Electronic Theses and Dissertations          Theses, Dissertations, and Major Papers

2011

# An Empirical and Simulation Study on Pressure Wave Propagation in Diesel Manifolds

Arturo Mendoza-Pinon
*University of Windsor*

Follow this and additional works at: https://scholar.uwindsor.ca/etd

AN EMPIRICAL AND SIMULATION STUDY ON PRESSURE WAVE
PROPAGATION IN DIESEL MANIFOLDS

By

Arturo Mendoza-Pinon

A Thesis
Submitted to the Faculty of Graduate Studies
through the Department of Mechanical, Automotive and Materials Engineering
in Partial Fulfillment of the Requirements for
the Degree of Masters of Applied Science at the
University of Windsor

Windsor, Ontario, Canada

2011

AN EMPIRICAL AND SIMULATION STUDY ON PRESSURE WAVE

PROPAGATION IN DIESEL MANIFOLDS

By

Arturo Mendoza-Pinon

APPROVED BY:

_____
Dr. Xiaohong (Iris) Xu, Outside Department Reader
Department of Civil and Environmental Engineering


_____
Dr. Graham T. Reader, Department Reader
Faculty of Engineering


_____
Dr. Jimi Tjong, Co-Adviser
Department of Mechanical, Automotive and Materials Engineering


_____
Dr. Ming Zheng, Co-Adviser
Department of Mechanical, Automotive and Materials Engineering


_____
Dr. Biao Zhou, Chair of Defense
Department of Mechanical, Automotive and Materials Engineering

20th September, 2011

# AUTHOR'S DECLARATION OF ORIGINALITY

I hereby certify that I am the sole author of this thesis and that no part of this thesis has been published or submitted for publication.

I certify that, to the best of my knowledge, my thesis does not infringe upon anyone's copyright nor violate any proprietary rights and that any ideas, techniques, quotations, or any other material from the work of other people included in my thesis, published or otherwise, are fully acknowledged in accordance with the standard referencing practices. Furthermore, to the extent that I have included copyrighted material that surpasses the bounds of fair dealing within the meaning of the Canada Copyright Act, I certify that I have obtained a written permission from the copyright owner(s) to include such material(s) in my thesis and have included copies of such copyright clearances to my appendix.

I declare that this is a true copy of my thesis, including any final revisions, as approved by my thesis committee and the Graduate Studies office, and that this thesis has not been submitted for a higher degree to any other University or Institution.

# ABSTRACT

Pressure wave oscillations occurring in both the intake and exhaust manifolds can potentially be applied to exhaust gas recirculation (EGR) and selective catalytic reduction (SCR), to increase their distribution efficiency and further reduce nitric oxide (NOx) emissions.

The work consists of an in depth study on pressure wave propagation in diesel exhaust manifolds for various operating conditions, such as: RPM, IMEP, EGR, Post-injection, backpressure, runner length, runner diameter, and position sweeps. The effect of pressure wave propagation in diesel manifolds, by varying such engine operating parameters, and geometric exhaust configurations, have been demonstrated empirically, and by simulation.

By understanding the characteristic behavior of the pressure waves, such as frequency, amplitude, and phasing, under different engine operating conditions, better EGR and SCR distribution strategies may be found. This may be done by implementing different manifold configurations and injection strategies, to the EGR and SCR systems, respectively.

# DEDICATION

This thesis is dedicated to my endearing parents; my beautiful mother Silvia Pinon Lopez and my incredible father Arturo Mendoza Caro, who have always been there for me unconditionally in every aspect of my life. It is because of them, that I have successfully completed this thesis, and who without, would be impossible.

# ACKNOWLEDGEMENTS

# TABLE OF CONTENTS

# LIST OF FIGURES

# LIST OF TABLES

# NOMECLATURE

| | |
|---|---|
| BDC | Bottom Dead Center |
| CAD | Computer Aided Design |
| CI | Compression Ignition |
| CO | Carbon Monoxide |
| $CO_2$ | Carbon Dioxide |
| DOC | Diesel Oxidation Catalyst |
| DPF | Diesel Particulate Filter |
| ECU | Electronic Control Unit |
| EGR | Exhaust Gas Recirculation |
| EVC | Exhaust Valve Closing |
| EVO | Exhaust Valve Opening |
| FSN | Filter Smoke Number |
| HTC | High Temperature Combustion |
| ICE | Internal Combustion Engine |
| IMEP | Indicated Mean Effective Pressure |
| IVC | Inlet Valve Closing |
| IVO | Inlet Valve Opening |
| LTC | Low Temperature Combustion |
| NO | Nitrogen Oxide |
| $NO_2$ | Nitrogen Dioxide |
| NOx | Nitric Oxides |
| Pinj | Injection Pressure |

| | |
|---|---|
| PM | Particulate Matter |
| ppm | Parts Per Million |
| psig | Pounds Per Square Inch Gauge |
| SCR | Selective Catalytic Reduction |
| SI | Spark Ignition |
| SOI | Start of Injection |
| TDC | Top Dead Center |
| THC | Total Hydrocarbons |
| TWC | Three Way Catalyst |

## CHAPTER I

## 1 INTRODUCTION

### 1.1 Motivation

Diesel engines posses an advantage of having higher thermal efficiencies, and being highly reliable and robust, than gasoline engines. The challenge lies in meeting the emission standards, as they continue to become more and more stringent. As a result, there is a need to focus on optimizing current in-cylinder, and after-treatment techniques, to meet the emission requirements.

The distribution of exhaust gas recirculation (EGR), an in-cylinder technique, used in reducing the amount of nitric oxides (NOx), varies among cylinders [8]. The injection strategies currently in place for selective catalytic reduction (SCR), an after-treatment system, which also reduces the amount of NOx, depend on the amount of exhaust flow. By manipulating pressure wave actions in diesel manifolds, the distribution of EGR among cylinders, and injection strategies associated with the SCR system, may potentially be optimized.

### 1.2 Objective and Approach

The objective of the work was to study pressure wave actions in diesel exhaust manifolds. These pressure wave actions in manifolds, are the cause of non-uniform charge distribution between cylinders, and are primarily used for intake tuning, to increase volumetric efficiency of natural aspirated engines [8]. The same pressure wave actions can potentially be used to increase the efficiency of EGR distribution among cylinders. The same concept can be taken and applied to the SCR system, to study different injection strategies.

The work primarily consists of studying pressure wave actions in the exhaust manifolds for two different research engines. Different engine parameters such as engine speed, load, backpressure, and post-injection are conducted, and their effect on pressure wave actions, analyzed. At the same time, simulation work for the same empirical conditions, plus the effect of runner length, runner diameter, and relative position, were conducted and analyzed.

The research engines used in this work to study pressure wave actions, have other primary research objectives, therefore there was a need to make a research platform, primarily to study pressure wave actions. During the course of this work, a portable dynamometer research platform, was designed and built to primarily serve this work. At the same time, in order to accurately measure intake and exhaust flow, an orifice meter was designed, built, and tested. This work is the first step in seeking different EGR distribution and SCR injection strategies.

**1.3 Thesis Organization**

This thesis is divided into six sections.

Section I, Introduction: This section covers the motivation, objective and approach, and thesis organization.

Section II, Background This section covers the basics of diesel engines, emissions, EGR, SCR system, and intake and exhaust manifolds.

Section III, Literature Review: In this section, an introduction to one-dimensional compressible flow is studied. Also, the method of characteristics is briefly explained and applied to a simple boundary flow problem. This helped in giving an understanding to the governing equations of compressible flow.

Section IV, Empirical and Simulation Set-up: In this section, the experimental and simulation set-ups are shown in detail. This section includes main engine platforms, pressure transducer system, data acquisition, simulation, portable dynamometer research platform, and orifice meter.

Section V, Results and Discussion: In this section, the analysis of different engine conditions and their effect on pressure wave action is shown. This section includes both empirical and simulated results which are then compared and validated.

Section VI, Conclusion and Future Work: In this section, the concluding remarks on pressure wave actions in the exhaust manifold are expressed, and the future work necessary to develop EGR distribution and SCR injection strategies, to further lower NOx.

# CHAPTER II

## 2 BACKGROUND

### 2.1 The Diesel Engine

Rudolf Diesel, a major contributor in the development of the current compression-ignition engine, understood that by increasing the compression ratio, one could achieve a higher thermal efficiency. In order to do so, Diesel proposed the idea of injecting fuel directly into the cylinder during the end of the compression stroke and throughout the expansion stroke. In this way the compression ratio could be dramatically increased, as opposed to spark ignition (SI) engines with their vulnerability to knock. As a result of Diesel's contribution, the diesel engine is highly efficient, robust, and reliable [1]. It is used in a variety of applications that require such characteristics which include marine, agriculture, and transportation, among others. Diesel engines also have the reputation of being loud and dirty due to its type of combustion, but in fact, possess an advantage of producing less engine-out emissions than SI engines [2,3]. Figure 2.1 compares both diesel and SI engines and their respective emissions. It clearly can be seen that for all emissions, with the exception of particulate matter (PM), diesel engines are cleaner. The advantage that SI engines have over diesel is the use of the three way catalytic converter which requires a near stoichiometric combustion, as opposed to diesel lean-combustion. In the many years since its invention, the diesel engine has technologically advanced to be one of the most efficient and clean engines available, but there is still a need in improving emission control strategies and devices, to continue approaching a zero-emissions standard.
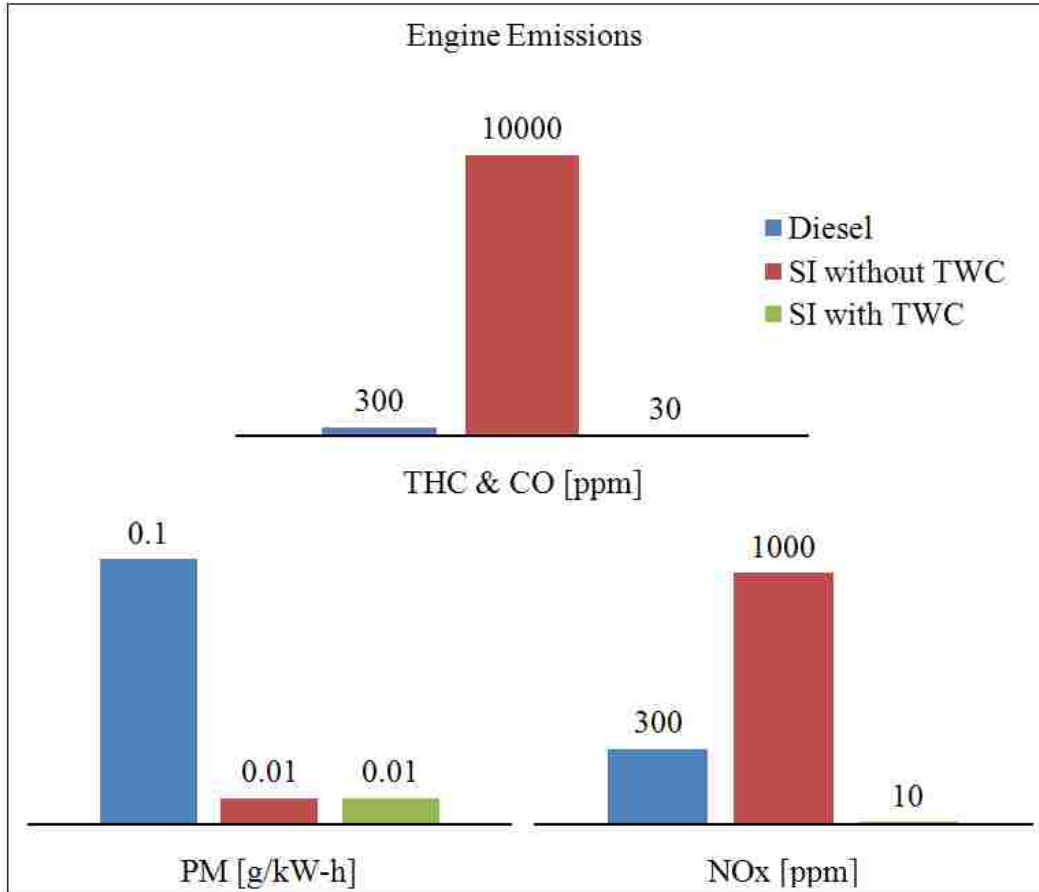
Figure 2.1: Diesel and Spark Ignition Engine Emissions (Adapted from [3])

Emission standards have become more and more stringent over the years, which regulate the amount of nitric oxides (NOx), total hydrocarbons (THC), carbon monoxide (CO), and particulate matter (PM). Figure 2.2 and 2.3 show the emission standards in North America for the past two decades, for heavy-duty diesel engines. There is a need to make internal combustion engines (ICE) cleaner, which can only happen by optimizing combustion and the after-treatment systems.
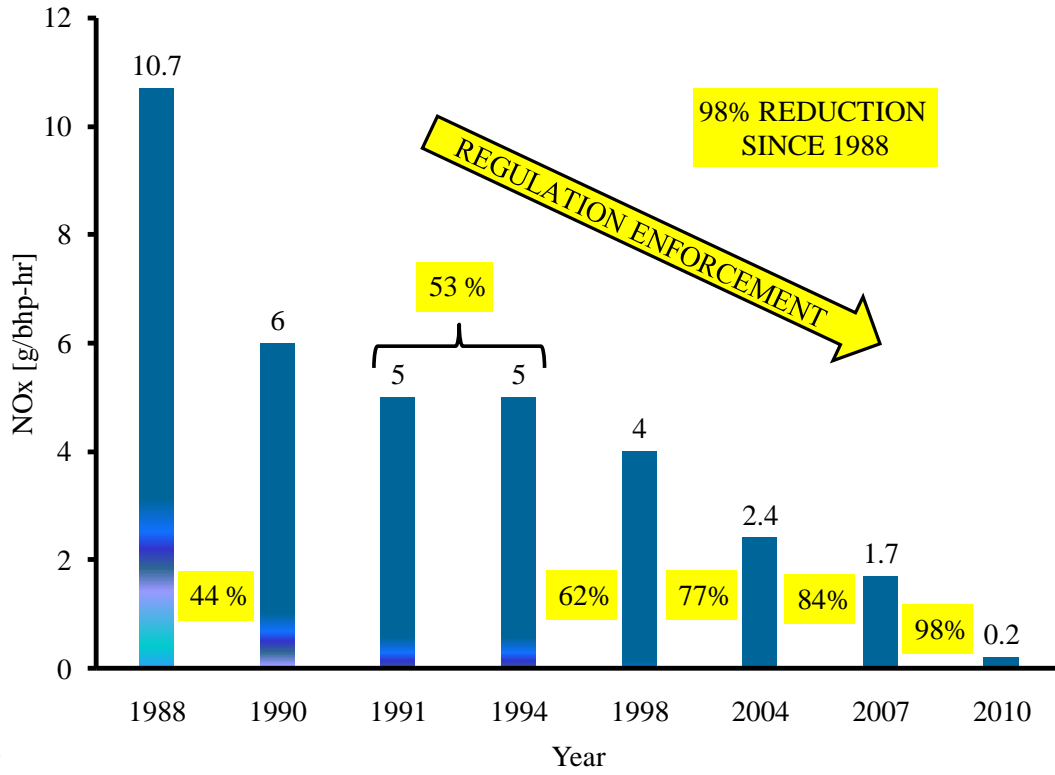
Figure 2.2: NOx Emission Standards [4]
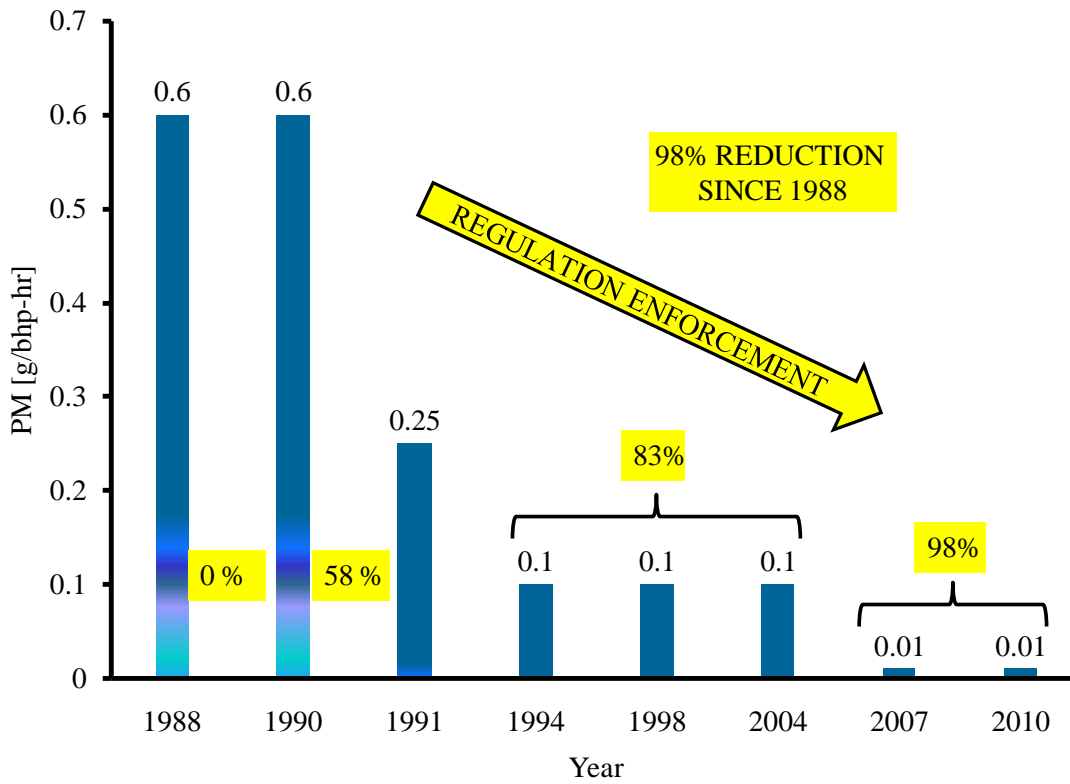


Figure 2.3: PM Emission Standards [4]

There are many different techniques used to lower emissions, both in-cylinder techniques and after-treatment devices. In-cylinder techniques such as the use of exhaust gas recirculation (EGR), effectively reduces NOx. On the after-treatment side, devices such as filters, traps, or injected chemicals along the exhaust system are used. A modern after-treatment system used to eliminate NOx, located on the upstream side of the exhaust system, is known as selective catalytic reduction (SCR). Both EGR and SCR strategies can be optimized in diesel engines to further lower NOx emissions, which are considered greenhouse gasses and smog causing compounds.

**2.2 Exhaust Gas Recirculation (EGR)**

As emission regulations become more stringent, there is a need to advance in emission control, and exhaust gas recirculation is just one of many emissions control strategies, to reduce NOx. Most of diesel exhaust consists of the compound NO, but once in the presence of oxygen it tends to oxidize and produce $NO_2$. The production of NOx depends on the amount of oxygen available and temperature. As cylinder temperatures reach above 2000 Kelvin, the rate at which NOx produces increases vastly. One must lower the combustion temperature or reduce the oxygen availability in the cylinder. EGR is effective in lowering both the combustion temperature and availability of oxygen. Figure 2.4 shows the typical implementation of EGR [5].
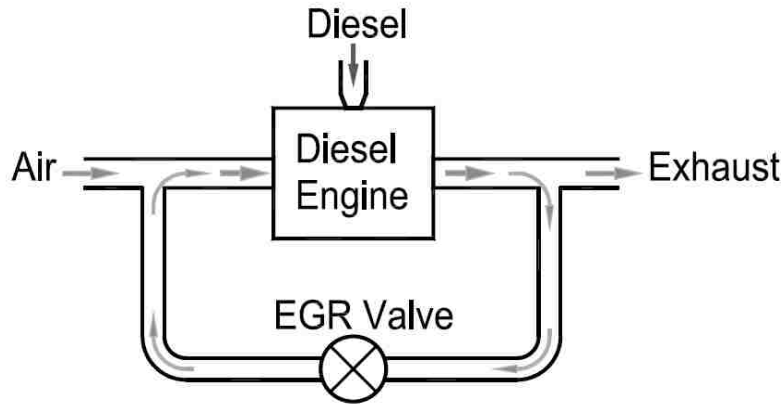
Figure 2.4: EGR Configuration (From [5])

Carbon dioxide ($CO_2$), an exhaust compound is used to calculate the amount of EGR. By knowing the concentration of $CO_2$ of both the intake and exhaust, one can calculate the amount of EGR introduced into the cylinder [5].

$$EGR \ ratio = \frac{\text{intake } CO_2 \ \text{concentration}}{\text{exhaust } CO_2 \ \text{concentration}}$$

As $CO_2$ enters the cylinder, it increases the heat capacity of the air charge, which in turn lowers down the specific heat capacity ratio, thus lowering the flame temperature. At the same time, EGR reduces the availability of oxygen since the fresh charge is being replaced by the exhaust gas from the previous cycle. By limiting the availability of oxygen, the fuel has more time to mix, therefore increasing ignition delay. As ignition delay increases, keeping fueling events constant, combustion occurs at a later stage of the expansion stroke. This causes a lower peak cylinder pressure, which yields a lower cylinder temperature, thus achieving lower NOx concentrations. Figure 2.5 shows the effect of EGR on ignition delay and peak cylinder pressure while figure 2.6 shows an EGR sweep at constant conditions and the effect on NOx production [5].
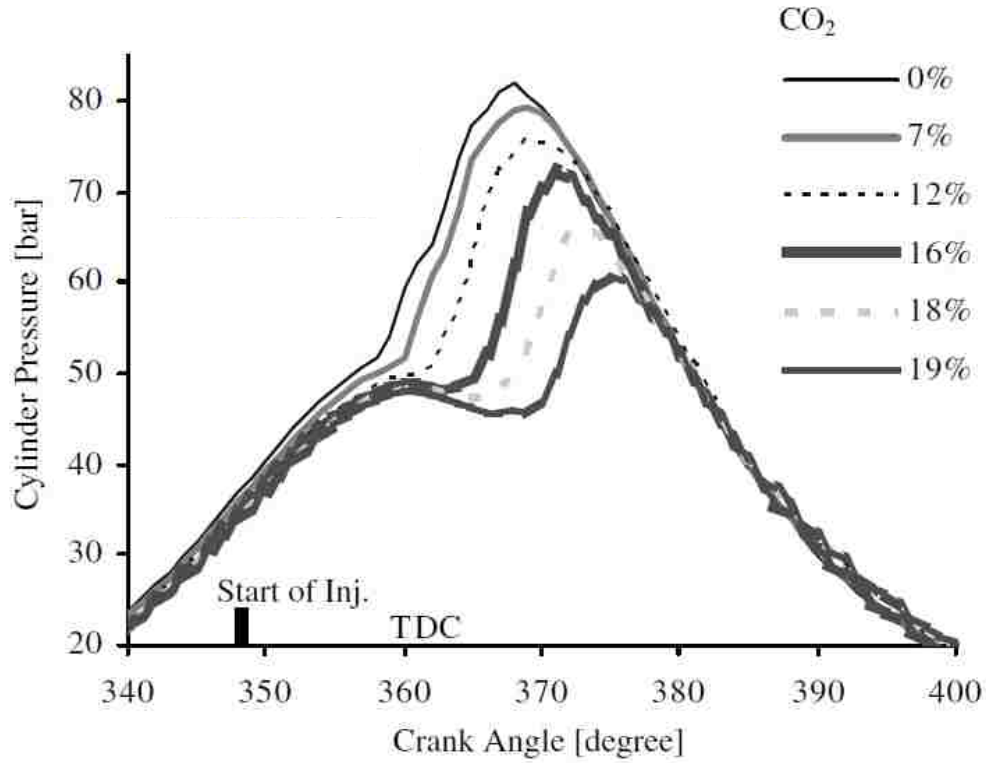
Figure 2.5: EGR Effect on Peak Pressure & Ignition Delay (Adapted from [5])
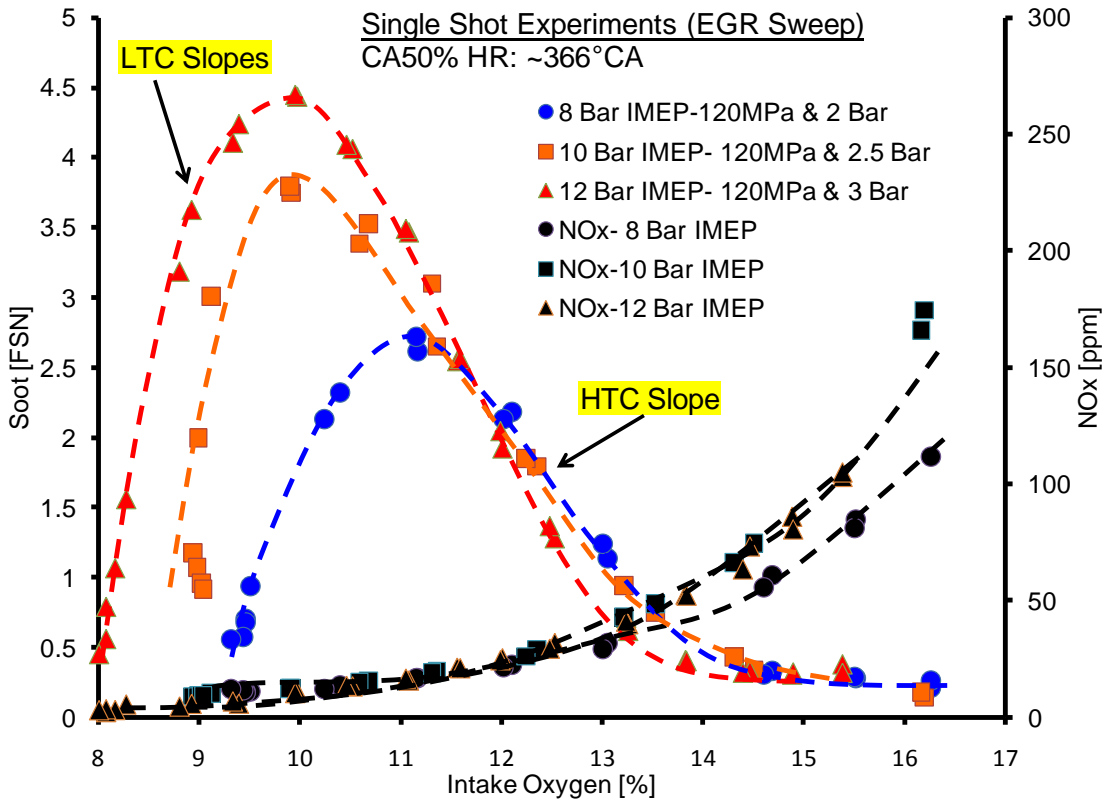


Figure 2.6: EGR Sweep

Figure 2.6 shows an EGR sweep at three different loads and the effect on soot and NOx emissions. It can be observed that NOx decrease with increasing EGR. At the same time the formation of soot increases, due to incomplete combustion. This decrease in NOx and increase in Soot is known as the classical NOx-Soot trade-off that occurs during typical diesel combustion or high temperature combustion (HTC). While simultaneously soot and NOx values are kept low, a mode of combustion known as low temperature combustion (LTC) has been achieved. This mode of combustion is the research for many, as it reaches ultra low NOx and Soot. There are many benefits as well as challenges with LTC, but since it is outside the scope of this thesis, no more will be covered.

In a multi-cylinder engine, where EGR is used, the exhaust gasses flow into the intake manifold, dispersing into each of the cylinders. The distribution of exhaust gas coming into the manifold is non-uniform throughout the cylinders, therefore varying combustion and emissions between them. In other words, one cylinder may be producing considerable more NOx than others, therefore contributing to an overall NOx increase. By individually tuning each runner on the intake manifold, the distribution can potentially reach a better degree of uniformity throughout the cylinders. The use of the pressure pulses or wave propagations caused by the valve train can help induce more exhaust into cylinders that are farther away from the EGR inlet.

## 2.3 Selective Catalytic Reduction (SCR)

SCR, as stated above, is an effective after-treatment device used on diesel powered vehicles to reduce NOx emissions by using a chemical agent known as urea. It is compound used primarily as fertilizer in the agriculture industry. Some is used in industrial applications as resins for plastics and also used for cattle feed [6].
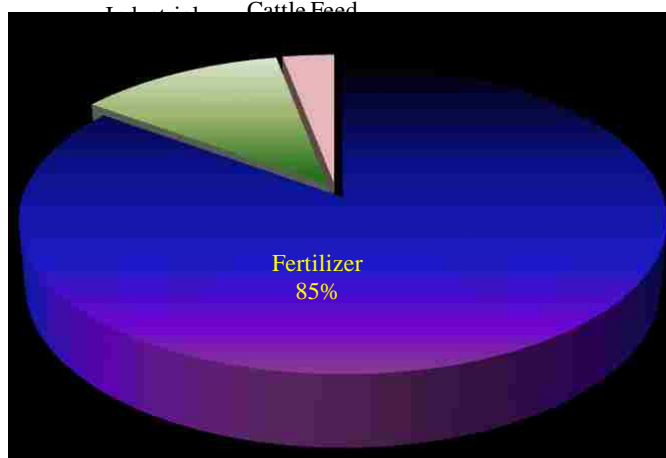
Figure 2.7: Urea Use [6]

A chemical agent or nitrogen containing compound such as urea, reduces certain nitric oxides in the presence of oxygen. It is termed 'selective' because it bonds with the oxygen attached to nitrogen instead of the molecular oxygen found abundantly in the exhaust. The following three chemical equations show how the SCR system works [6].

$$(NH_2)_2CO + H_2O \longrightarrow CO_2 + 2NH_3$$

$$4NO + 4NH_3 + O_2 \xrightarrow{CATALYST} 4N_2 + 6H_2O$$

$$6NO_2 + 8NH_3 \xrightarrow{CATALYST} 7N_2 + 12H_2O$$
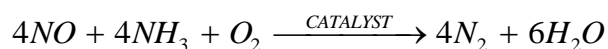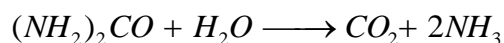
If urea $((NH_2)_2CO)$ is used as the reductant, it first needs to undergo hydrolysis in order to produce the ammonia needed for the system. This is done by mixing raw urea with water, as seen in the first equation. After the urea has undergone hydrolysis to produce the necessary ammonia, it is then injected into the exhaust stream, reducing both NO and $NO_2$, as seen in previous

11

equations. In order to lower the activation energy to speed up the reactions, an SCR catalyst is placed after the injected ammonia in the exhaust system. The complete system consists of four major parts [7]:

1) Urea Tank

2) SCR Doser

3) SCR Catalyst

4) Ammonia Catalyst

The urea tank contains the prepared ammonia solution; it is then injected by an SCR doser. The SCR catalyst as stated before speeds up the reduction reactions for the nitride oxides and the ammonia catalyst reduces the left over ammonia that does not get consumed. A typical SCR system layout is shown in figure 2.8. Before the SCR doser a diesel oxidation catalyst (DOC) and diesel particulate filter (DPF) are typically used.
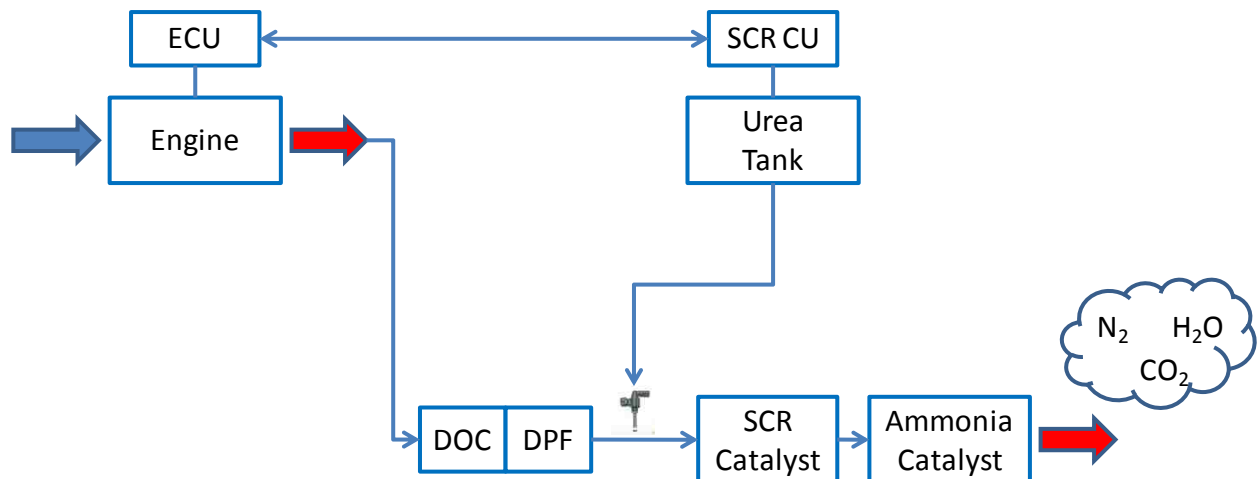


Figure 2.8: Urea Delivery Diagram (Adapted from [6])

The importance lies on the delivery method of the ammonia solution, which affects conversion efficiency. Currently the injection strategies on most systems are defined by an injection rate and amount, depending on the exhaust flow rate calculated by the engine's ECU. The use of the pressure oscillation in the exhaust manifold could be used, in order to optimize the delivery and increase distribution efficiency.

**2.4 Manifolds**

As both EGR and SCR distribution occur in both the intake and exhaust systems respectively, it is necessary to understand the flow characteristics in intake and exhaust manifolds. The design of intake and exhaust manifolds in reciprocating engines, have been studied into great detail to improve the gas exchange processes. On the intake manifold for naturally aspirated engines, the goal is to increase the manifold pressure which gives an increase in volumetric efficiency. This volumetric efficiency at a constant air/fuel ratio will increase the brake mean effective pressure, thus achieving higher torque. It is defined by the volume flow rate divided by the rate at which the volume changes caused by the piston [8].

$$\eta_v = \frac{2\dot{m}_a}{\rho_{a,i}V_d N}$$

The increase in volumetric efficiency is due to the pressure wave actions that occur in the intake system due to the valve events. These pressure wave actions occur in the individual runners for each cylinder. By tuning the runners, one can achieve a higher volumetric efficiency at a given engine speed. One of the most significant tunable factors in the intake system for naturally aspirated engines is the runner length, and its effect on volumetric efficiency can be seen in Figure 2.9 [9].
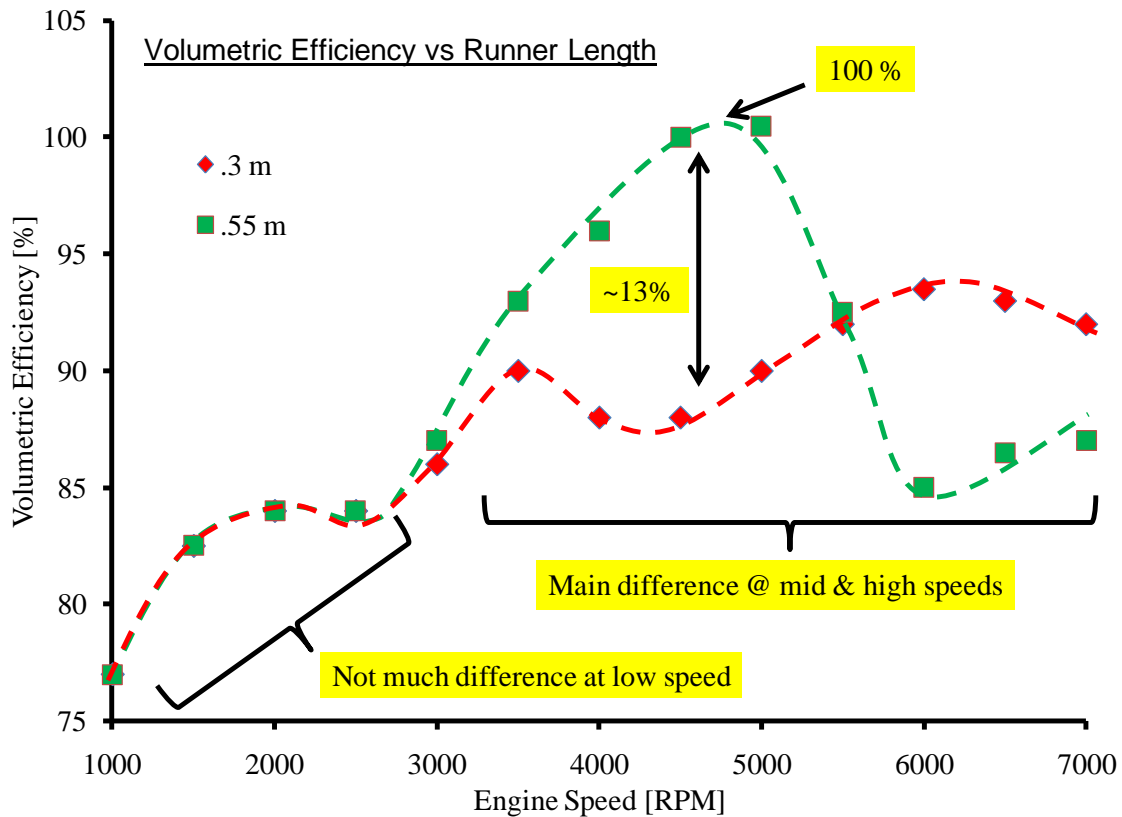
Figure 2.9: Volumetric Efficiency vs Runner Length (Adapted from [9])

In this particular engine two different runner lengths are tested and their effect on volumetric efficiency. Below 2500 rpm the volumetric efficiency stays relatively constants throughout the different runner lengths. Throughout the midrange, the shorter runner causes a higher volumetric efficiency due to the increased mass of air in the runners [9]. Longer runners are effective at middle to low engines speeds, but at higher speeds the effectiveness decreases rapidly. During higher engine speeds a shorter runner length is desirable to increase volumetric efficiency.

14

In order to overcome this issue, variable runner intake manifolds are required, where two air flow passages exist controlled by a valve. At lower engine speeds, the short runner closes, letting the air flow pass through the longer runner. The opposite occurs during higher engine speeds, where the shorter runner opens.

Air flow inside intake manifolds depend on the details of each branch for each cylinder, the way it connects to the plenum, and firing order [8]. Since no branch is identical in a multi-cylinder engine, the flow characteristics differ between each branch for each cylinder. This causes a greater volumetric efficiency in some cylinders than others. Variations of flow between cylinders have been measured to be up to 15% [8]. This causes a concern when EGR is employed to lower down NOx. By understanding flow characteristics inside manifolds, one can create a more uniform air charge between cylinders, and potentially further decreasing NOx emissions.

Most modern diesel engines do not lack in volumetric efficiency as they come equipped with turbochargers. Regardless of turbocharging in diesel engine the same pressure wave actions occur in their respective intake manifolds. Currently, diesel engine intake manifolds are not tuned since volumetric efficiency is not an issue, but the pressure wave actions can be used to distribute EGR more efficiently and uniformly throughout the cylinder to effectively lower NOx even further.

On the other hand, the exhaust manifold needs to be designed to create a lower pressure atmosphere, at the time of the exhaust valve opening in order to extract the exhaust gas quickly, therefore increasing the amount of fresh air charge into the cylinder. The same idea as the intake system can be applied to the modern turbocharged diesel engines to further lower NOx. Instead of creating a low pressure atmosphere at the time of the exhaust valve opening, the opposite can

be created in order to keep a portion of the exhaust gas inside the cylinder. This is known as internal EGR. In most engine laboratories, internal EGR is controlled by the amount of backpressure instead of by pressure wave action. The same pressure wave action used for internal EGR can be used to optimize the injection strategy in the SCR system. Therefore, it is necessary to have an in depth understanding of pressure wave action in both intake and exhaust systems, to be able to apply it to emissions control.

# CHAPTER III

## 3 LITERATURE REVIEW

### 3.1 One-Dimensional Compressible Flow Properties

Gas dynamics refers to fluid flow where significant changes in density and temperature occur. These changes typically occur at Mach number .5 and greater. They occur when the fluid, either a gas or a liquid, is subjected to a certain amount of pressure and as a result becomes compressed, thus changing the density of the fluid. In most cases, liquids are assumed non-compressible fluids for simplicity, but in fact are compressible to a certain degree. Gases on the other hand, have a higher degree of compressibility, thus significantly changing the density and temperature throughout the flow. Another way of showing the difference between compressible and in-compressible flow is the rate at which density changes. For example, consider a pipe where air is being pumped at certain flow rate and the pressure is suddenly increased to attain a higher flow rate. The air, on which the compression force is acting on, causes an increase in density and expands to the adjacent air molecules which are a lower density. The lower density air then becomes compressed and this pressure wave continues until it reaches the end of the pipe and then gets reflected back. The motion of these fluids which are subjected to various force fields, cause a change in the direction, speed, and thermodynamic state throughout the fluid flow. These changes are the subject of study of fluid dynamics [10,11,12,13,14].

### 3.1.1 One-Dimensional Flow

All fluid flows, external or internal are three-dimensional where pressure, temperature, velocity, and other flow properties vary in all directions. Flow is considered one-dimensional if the properties stated only change along the flow direction and remain constant within the cross-

section. In most cases analyzed such as pipe flow, the fluid properties majorly vary along the fluid flow direction making it one-dimensional but in reality have some variation within the cross-section as seen in figure 3.2. By analyzing flow in one dimension, the governing equations simplify greatly. Pipe flow can be treated in two dimensions to account for the property variations along the cross-section but it is required if accuracy is the objective. Certain correction factors are used in one-dimensional flow to account for these variations. In this thesis, one-dimensional unsteady flow is only considered as a high level of accuracy is not required [15].



Figure 3.1: Ideal Flow (Adapted from [15])    Figure 3.2: Actual Flow (Adapted from [15])

In calculating one-dimensional unsteady flow in any system including engines, boundary conditions are needed at both ends of the pipes. The development of such boundary conditions, are the work for many and require considerable amount of mathematical effort. There are three major differences between calculating flow between engine manifolds and other flow situations [8,9]:

1) Engine manifolds have a relatively smaller length/diameter ratio than other pipe network applications [8,9].

2) Engine manifolds reach a steady periodic flow during engine operation whereas other pipe cases consist of one sudden blowdown [8,9].

18

3) The ideal gas assumption is applied to engine manifold problems as opposed to other pipe problems [8,9].

It is important to understand the properties of gas flow in manifolds and the following sections cover such properties.

### 3.1.2 Compressibility

Fluids such as water are typically incompressible at low pressure conditions, but when subjected to pressures higher than 1000 bar, such fluids become compressible. During static conditions, if the fluid shows a change in volume then it is compressible. So, in other words, the degree of volume change dictates the compressibility of the fluid during static conditions. During dynamic conditions for the fluid to be incompressible, the volume flow rate remains constant while in compressible flow, the mass flow rate remains constant at any cross-section of the pipe [11,12,13,14].

$$\dot{Q} = AV = \text{Constant (incompressible flow)}$$

$$\dot{m} = \rho AV = \text{Constant (compressible flow)}$$

If a gas flows at a relative low speed, the change in density or volume from one cross-section to the other can be neglected, and therefore be treated as incompressible flow. The volume modulus of elasticity defines the compressibility of a fluid which depends on the change in static pressure and volume [11,12,13,14].

$$E = -\frac{\Delta p}{\Delta V / V_i}$$

This relationship can be further simplified by using the ideal gas equation, and seen that compressibility can be defined as the volume modulus of pressure [11,12,13,14].

$$E = p_i$$

### 3.1.3 Speed of Sound

Sound waves which are made up of small pressure oscillations or disturbances travel at a certain speed through a certain medium. The rate at which these waves travel is called the "speed of sound" and is denoted by the letter 'a'. Consider a piston moving in a cylinder where a certain gas is the medium inside the cylinder [11,12,13,14]. The piston moves horizontally with a certain velocity doing work on the adjacent gas, and leaving the gas with a higher pressure $p_1$ and density $\rho_1$ than the downstream gas, therefore [11,12,13,14].:

$$\Delta p = p_1 - p_i$$

$$\Delta \rho = \rho_1 - \rho_i$$

Choosing 'Ab' as the control volume, 'b' denoting the horizontal distance, and 'A' being the cross sectional area of the cylinder, the mass flow into volume 'Ab' is defined as [11,12,13,14]:

$$\dot{m} = \rho_1 A V$$

The above relationship must be equal to the mass flow rate through the control volume so [11,12,13,14]:

$$\frac{Ab(\rho_1 - \rho_i)}{t} = \rho_1 A V$$

But since $t = \dfrac{b}{a}$ then,

$$a(\rho_1 - \rho_i) = \rho_1 V$$

20

The acceleration caused by the piston and the mass in the control volume are defined by [11,12,13,14].:

$$\frac{V}{t} = V\frac{a}{b} \quad , \quad m = Ab\bar{\rho}$$

Where $\bar{\rho}$ is the average density:

$$\bar{\rho} = \frac{\rho_1 + \rho_i}{2}$$

Now let's consider the Newton's second law and apply to the control volume. The force acting on the control volume depends on the difference of pressure and the cross sectional area as shown [11,12,13,14].:

$$A(p_1 - p_i) = m(V\frac{a}{b})$$

$$A(p_1 - p_i) = (Ab\bar{\rho})(V\frac{a}{b})$$

$$\bar{\rho}Va = p_1 - p_i$$

Simplifying this even further, shows that the speed of sound 'a' depends on the difference ratio of pressure over density, also known as the Laplace equation [11,12,13,14]:

$$a^2 = \frac{dp}{d\rho}$$

For an ideal gas the Laplace equation becomes dependent on the ratio of specific heats and temperature [11,12,13,14]:

$$a^2 = \sqrt{\kappa RT}$$

### 3.1.4 Mach Number

There are different types of compressible flow that are categorized based on their Mach number, which is defined as the ratio of flow speed over the local speed of sound [11,12,13,14]:

$$M = \frac{V}{a} \text{ (Mach number)}$$

Compressible flow is categorized into the following [11,12,13,14]:

- Subsonic

- Supersonic

- Sonic

- Transonic

- Hypersonic

Subsonic flow refers to flow having a flow speed less than the local speed of sound. When flow speed is much less than the local speed of sound, it can be treated as incompressible flow, because the variations of density throughout the flow are minor, therefore negligible. Subsonic flow falls between a Mach number of $0 < M < 1$. Supersonic flow refers to flows speeds higher than the local speed of sound and has a Mach number value of $1 < M < \infty$, while Sonic flow refers to flow speeds equal to the local speed of sound [11,12,13,14].

Transonic flow refers to flow moving from subsonic to supersonic or vice versa. This phenomenon can be seen in both divergent and convergent ducts such as in engine manifolds. Since two types of flows are present in transonic flow, two mathematical techniques are needed to reach a solution when modeling [11,12,13,14].

Hypersonic flow typically refers to speeds of a Mach number greater than five. The Mach value at which the flow can be considered hypersonic, depends on the characteristics of the fluid and shape of the body the fluid interacts with [11,12,13,14].

**3.1.5 Choked Flow**

Choked flow, known as critical flow, refers to the gas velocity when the sonic boundary is reached. This sonic boundary is typically defined by a pressure ratio, of downstream over upstream of about 0.528 [16]. At this point maximum gas flow velocity for the given conditions has been reached. A commonly mistaken concept by many is that as choked flow is reached, the mass flow rate also freezes. If the upstream pressure for a given system at choked flow conditions is increased, the density increases. This increase in density changes the mass flow rate passing through a given orifice, but keeping the velocity through it the same. This concept applies to the valve events in IC engines during the intake and exhaust strokes.

**3.1.6 Waves**

In both intake and exhaust manifolds, two types of pressure waves occur:

1) Compression
2) Expansion

**3.1.6.1 Compression Waves**

A compression wave travels from a high pressure atmosphere to a lower, increasing the pressure and temperature throughout its propagation. Just before the exhaust valve opens, the pressure inside the exhaust manifold is below the in-cylinder. As the exhaust valve opens, the gasses are expelled from the cylinder at high pressure, creating a compression wave to travel to the end of the exhaust manifold. This compressions wave is used on intake manifold tuning to increase volumetric efficiency.

### 3.1.6.2 Expansion Waves

Expansion waves travel in the opposite direction than compression waves, decreasing pressure and temperature throughout its propagation. Taking the same example as above, at the same time the compression wave is created, an expansion wave as well in the opposite direction. These expansion waves are used in exhaust manifolds to draw the exhaust gasses out of the cylinder quicker and induce more fresh air charge into the cylinder.

### 3.1.6.3 Shock Waves

This type of propagation wave does exist in exhaust manifolds. It is characterized by an abrupt change in the flow characteristics. The temperature, pressure, and density greatly differ across the shock wave. A shock can develop from a compression wave as it increases in speed, and it is only matter of time and distance before it is formed. This type of propagation wave is not studied in this thesis, as it incorporate changes in entropy which is not considered [17].

### 3.2 Intake and Exhaust Flow

### 3.2.1 Flow Modeling Techniques

There are three approaches in modeling and understanding air flow in internal combustions engines [8,17]:

1)  Quasi-Steady Methods
2)  Filling and Emptying Methods
3)  Wave Action Methods

### 3.2.1.1 Quasi-Steady Model

It is the simplest model of all three since it considers all intake and exhaust systems as interconnected components. For each component it is required to empirically determine their steady-state characteristics or flow restriction. It is also simple since it allows for no mass accumulation, or in other words the manifolds are considered to have a negligible volume. This thermodynamic analysis allows for mass flow rates in and out of the cylinder but require empirical input. The equations used consist of simple first order non-linear ordinary differential equations. Such method works ideally where small pressure oscillations occur in the manifold systems as in short runner accompanied by big plenums [8,17].

### 3.2.1.2 Filling and Emptying Model

This method is more challenging than the previous one and can be compared to the gas dynamic models in difficulty, which are explained in the next section. This method takes both the intake and exhaust manifolds systems as finite volumes. The complete system can be divided up into separate connected control volumes which can store mass. As the quasi-steady model, the equations used form first order non-linear ordinary differential equations. This method requires less empirical input and since the systems are represented by one pressure and temperature, variations in charge distribution between cylinders or performance tuning is not possible. In other words, the method cannot account for unsteady gas dynamics which cause spatial variations [8,17].

### 3.2.1.3 Gas Dynamic Model

This technique involves the equations of compressible flow and allows different pressures along the intake and exhaust manifolds. The equations form a set of hyperbolic differential equations and means of solving these equations are needed. Since there is no analytic solution to these equations, graphical or numerical solutions are sought. These equations that describe compressible fluid flow are limited to one dimension, leaving two or three dimensional effects such as junctions and diffusers not possible. This technique provides a measure in predicting the performance of certain engines. It can be applied to the initial design stages of both intake and exhaust manifolds because it is able to show both the advantageous and disadvantageous resonances at all loads and speeds of engines. A few of the concerns in multi-cylinder engines is the bad distribution of charge between the cylinders or poor volumetric efficiency. This technique can be used to analyze these issue and as a design method for intake and exhaust manifolds [8,17].

### *Method of Characteristics*

This method is a technique to solve the hyperbolic partial differential equations associated with gas dynamic models. It takes the hyperbolic partial differential equations and transforms them by either graphical or numerical methods into ordinary differential equations. It primarily studies the pressure wave oscillations in unsteady flow which travel at the local speed of sound. The graphical method was the dominate method to solve such gas dynamic problems up until the 1950s. It requires extensive time to solve even for simple problems with simple boundary conditions. The drawback with this method is that it not capable of calculating discontinuities such as shock waves which are seen in exhausts systems of high speed engines. In other words,

this method serves only for first order accuracy. Even though, the method has been around for quite some time, it has the benefit of giving understanding or feel, to the person by using this technique in the graphical way [8,17]. This method has been applied to a simple homentropic non-steady flow problem shown in a later section [8,17].

**3.2.2 One-Dimensional Unsteady Compressible Flow Governing Equations**

The following equations govern one-dimension unsteady homentropic compressible flow for constant area ducts. There are three main equations which describes this type of flow [9,17]:

1) Continuity

2) Momentum

3) Energy

**3.2.2.1 Continuity Equation**

This equation states the mass flow rate change within the control volume is equal to net change in mass flow rate through the system [9,17]. This relationship is expressed as follows:

$$\frac{\partial(\rho u)}{\partial x} = \frac{\partial \rho}{\partial t}$$

$$\frac{1}{\rho}\frac{\partial \rho}{\partial t} + \frac{u}{\rho}\frac{\partial \rho}{\partial x} + \frac{\partial u}{\partial x} = 0$$

### 3.2.2.2 Momentum Equation

It states that the sum of both pressure and shear forces acting on the control surface, equal the sum of the total rate of change of momentum and efflux of momentum for the control volume [9,17].

$$-\frac{\partial \rho}{\partial x} = \rho \frac{Du}{Dt}$$

Where,

$$\frac{Du}{Dt} = \frac{\partial u}{\partial t} + u \frac{\partial u}{\partial x}$$

So the momentum equation can be represented as:

$$-\frac{\partial p}{\partial x} = \rho \frac{\partial u}{\partial t} + \rho u \frac{\partial u}{\partial x} = 0$$

$$\rho \frac{\partial u}{\partial t} + \rho u \frac{\partial u}{\partial x} + \frac{\partial p}{\partial x} = 0 \ , \ divide \, by \, \rho$$

$$\frac{1}{\rho} \frac{\partial p}{\partial x} + \frac{\partial u}{\partial t} + u \frac{\partial u}{\partial x} = 0$$

### 3.2.2.3 Energy Equation

The energy equation can be derived from the first law of thermodynamics which states the entropy change of a particle that passes through the given control surface. The general form is shown first below. As stated above the flow in this case is considered homentropic which

28

involves no change in entropy, therefore the first equation reduces to the second. The second equation, further reduces to third equation, since the gas is assumed ideal for simplicity [9,17].

$$\left(\frac{\partial p}{\partial t}+u\frac{\partial p}{\partial x}\right)-a^2\left(\frac{\partial \rho}{\partial t}+\frac{\partial \rho}{\partial x}\right)-(k-1)\rho(q+uG)=0$$

$$\frac{dp}{d\rho}=a^2=\left(\frac{\partial p}{\partial \rho}\right)_s$$

$$a^2=\frac{kp}{\rho}$$

**3.2.2.4 Hyperbolic Partial Differential Equations**

The three previous conservation equations govern one-dimension unsteady homentropic compressible flow for constant area ducts. These equations can be further combined, yielding two equations which are in terms of local speed of sound and particle velocity. The two equations shown below, form quasi-linear hyperbolic partial differential equations. These two equations are the ones solves by the method of characteristics [17].

$$\frac{2}{(\kappa-1)}a\frac{\partial a}{\partial x}+\frac{\partial u}{\partial t}+u\frac{\partial u}{\partial x}=0 \; (Momentum)$$

$$\frac{2}{(\kappa-1)}\frac{\partial a}{\partial t}+\frac{2}{(\kappa-1)}u\frac{\partial a}{\partial x}+a\frac{\partial u}{\partial x}=0 \; (Continuity)$$

### 3.2.3 Example: Sudden Valve Opening

The following is a recreation of a problem in Benson et.al book [17]. The purpose was to understand the characteristic calculation and analyze the results. The problem in Figure 3.3 consists of a very large receiver connected to a pipe with a certain diameter. The receiver is kept at a constant pressure and temperature by the inlet located on the left. At the end of the pipe, a valve exists and is suddenly opened to ambient conditions. A graphical calculation was conducted, but instead of using an AO drawing board, CATIA, a computer aided design (CAD) software was used. The pressure and velocity results are plotted for location A and B shown in figure 3.4 and 3.5.
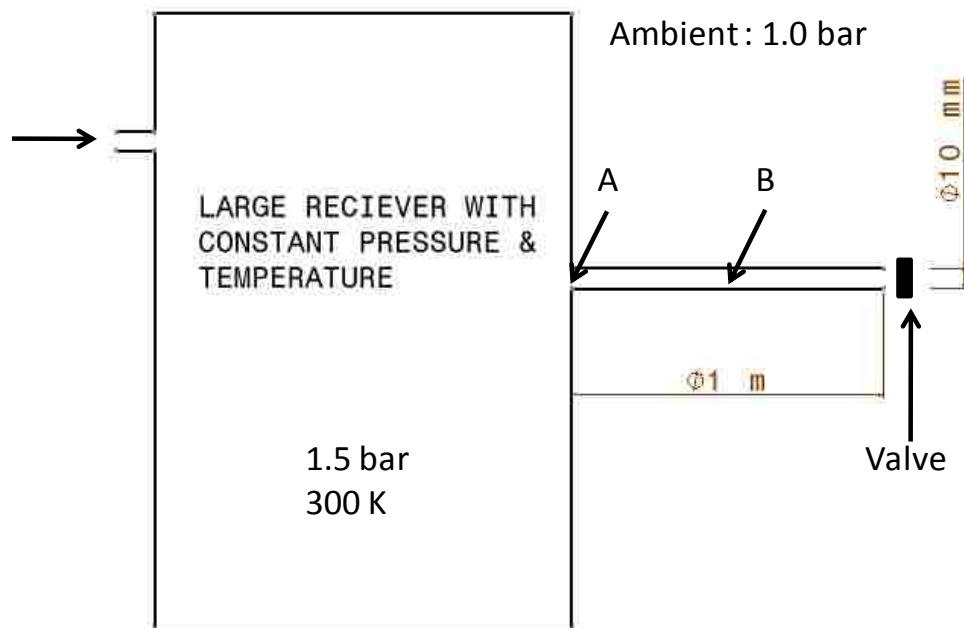


Figure 3.3: Sudden Discharge Problem (Adapted from [17])
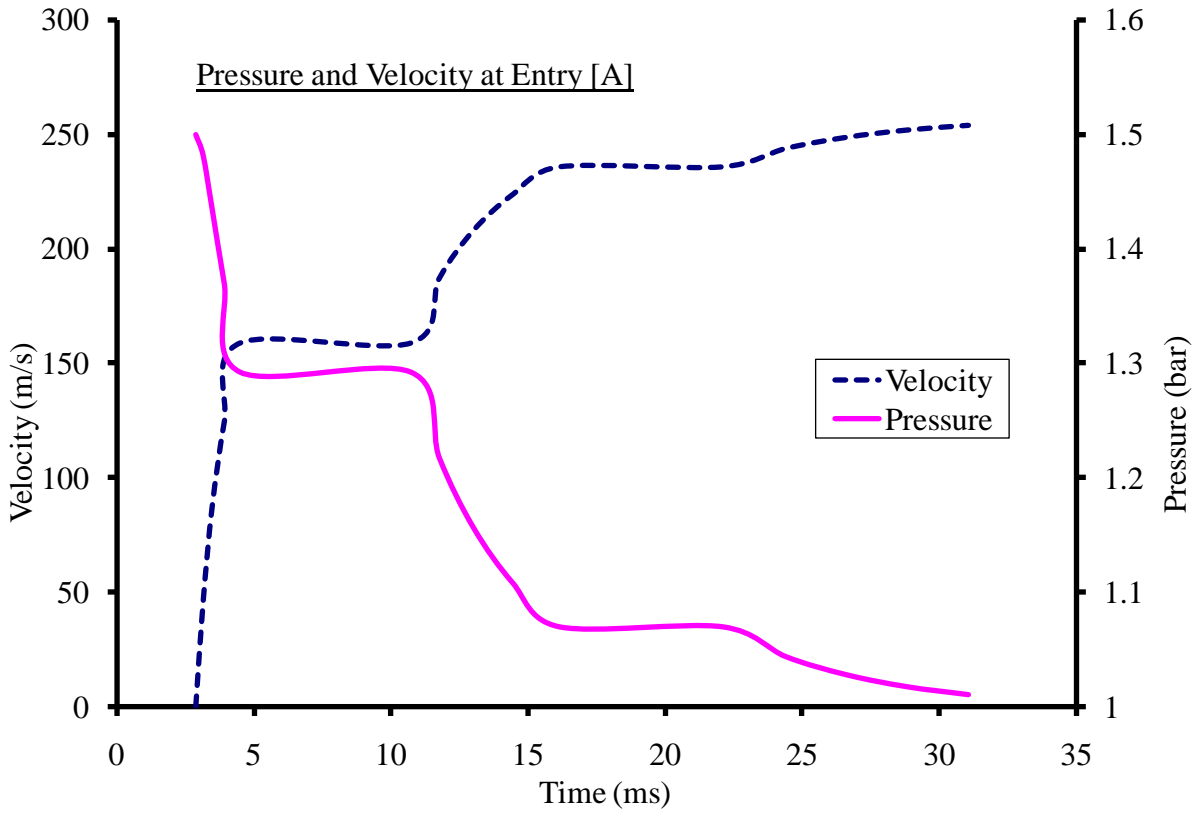
Figure 3.4: Pressure & Velocity at Entry [17]
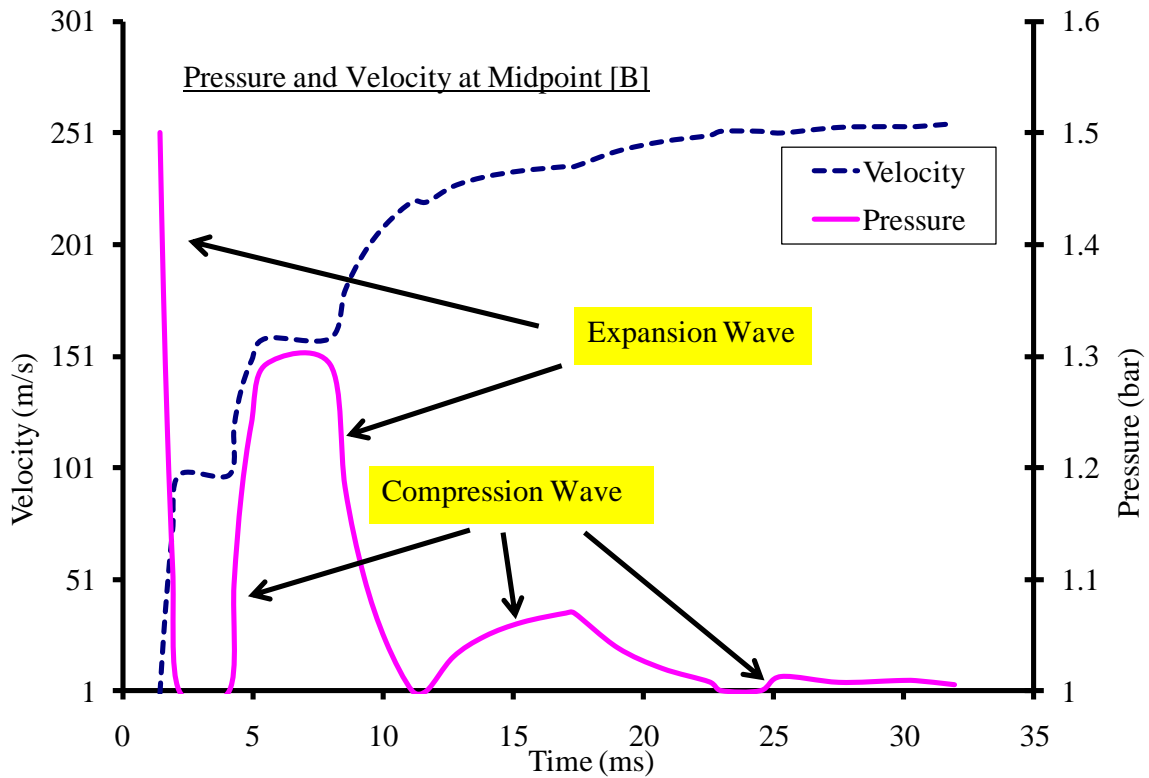


Figure 3.5: Pressure & Velocity at Midpoint [17]
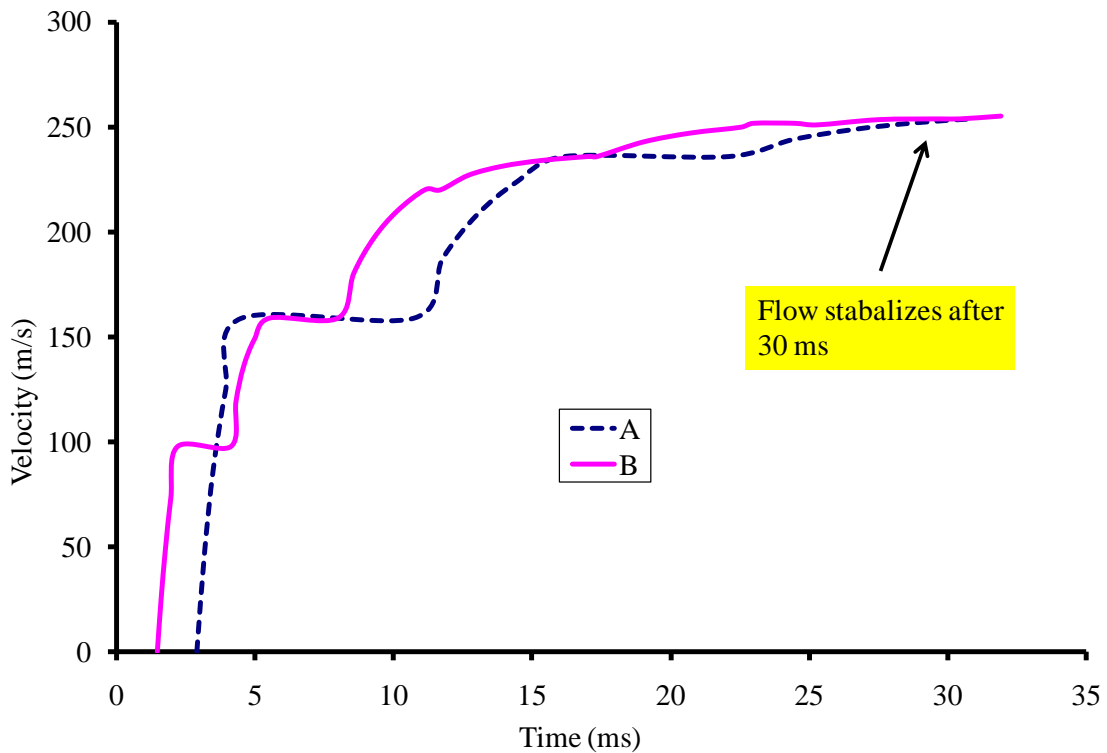
Figure 3.6: Velocity Profile [17]

In figure 3.4 and 3.5 the pressure traces along with the flow velocity are shown with respect to time. As the valve is suddenly opened, an expansion wave propagates toward the left and reaches the midpoint and entry points at 2 ms and 3 ms, respectively. At the midpoint the expansion wave causes the pressure to drop to ambient conditions. The same is not true for the entry point as a constant pressure is kept in the reservoir. Nonetheless, the first expansion wave does cause a pressure drop at the entry point but not as drastic as the midpoint. Once the expansion wave reaches the entry point, it returns as a compression wave, keeping the pressure almost constant at the entry point but raising it at the midpoint. The compression wave arrives at the midpoint, recognized by the sudden increase in pressure at about 4 milliseconds. This pressure oscillation continues until about 30 milliseconds and the flow stabilizes throughout the pipe as shown in figure 3.6.

This calculation gave an understanding of pressure waves in ducts as seen in intake manifolds for IC engines. This calculation required intensive amount of time to complete but it gives a feel as the pressure wave propagates along the pipe. This simple boundary flow problem was calculated using the method of characteristics, and the rest of the simulation work conducted in this thesis consists of using the simulation software Ricardo.

**CHAPTER IV**

**4   EMPIRICAL AND SIMULATION SET-UP**

**4.1 Ford Puma**

The Ford puma engine is a four-cylinder two liter diesel production engine. It is a donation from Ford Motor Company for research purposes only. The majority of the research conducted in this thesis, comes from this platform, therefore the simulation conducted, shown in the following sections, use the platform's specifications. Research is conducted on cylinder number one, which is isolated from the rest of the cylinders. The engine is referred to as a box engine, since both the bore and stroke are equal. It has the highest compression ratio out of both engines used. Table 4.1 shows the main engine specifications for the Ford Puma engine.

| FORD PUMA SPECIFICATIONS | |
|---|---|
| Cylinders | 4 |
| Type | 4-Stroke |
| Displacement | 1.998 Liters |
| Bore | 86 mm |
| Stroke | 86 mm |
| Compression Ratio | 18.2:1 |
| Injection System | Delphi Common Rail (1600 bar) |

Table 4.1: Ford Puma Specifications

*Layout*

As seen in Figure 4.1, cylinder one is isolated from the rest of the cylinders. The supplied air comes from a pressurized tank and is controlled by a valve. The air then passes through an air flow meter and is dumped into the surge tank. The surge tank ensures proper reading at the flow meter, since it cancels any pressure fluctuations caused by the engine. The exhaust system also contains a surge tank for the same purposes. In order to control the amount of gas recirculation, a backpressure valve, as well as an EGR valve is used. The backpressure valve controls the amount of pressure in the exhaust system; while the EGR valve controls the amount of exhaust gas recirculation entering the intake system.
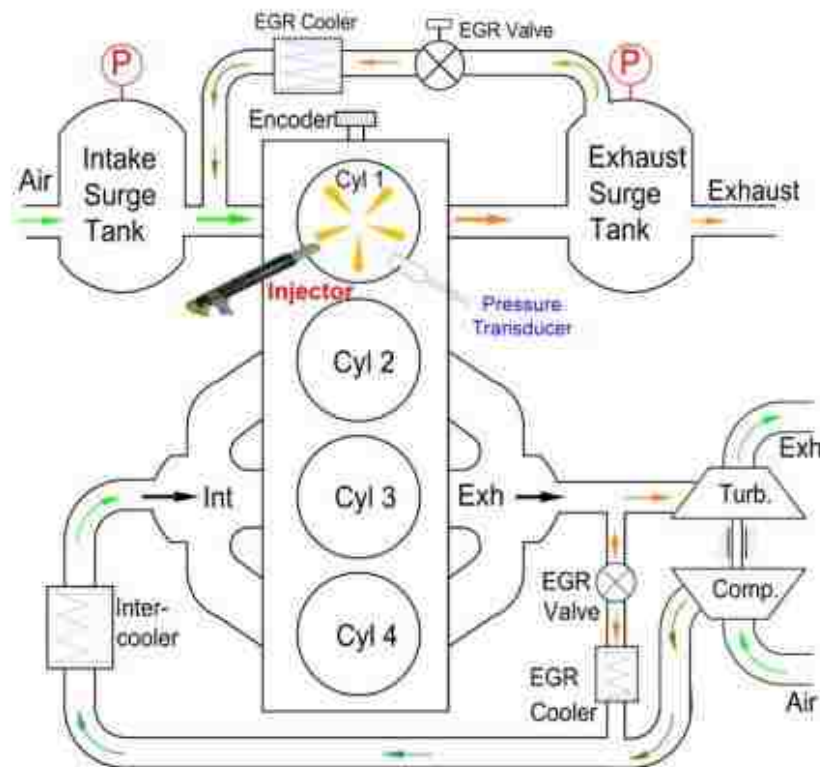


**Figure 4.1: Ford Puma Schematic**

Cylinders two through four use a separate intake system but eventually connect to the same exhaust system. While in operating conditions the three cylinders that are isolated from cylinder one, receive the same amount of fuel necessary to help balance, and eliminate any unwanted engine vibrations due to variance in combustion from cylinder one.

The exhaust system contains numerous pipe diameters and lengths, leading up to the surge tank. At the cylinder head, a flange connected to a one inch pipe inner diameter is used. The pipe makes a $45^o$ angle directly from the flange. The pipe has a length of about 350 mm, and it is the one used for the pressure wave measurement as shown in Figure 4.2. The pressure port measures a distance of about 140 mm to the exhaust valves. Figure 4.3a and 4.3b show the actual pressure transducer installed on the one inch exhaust pipe.
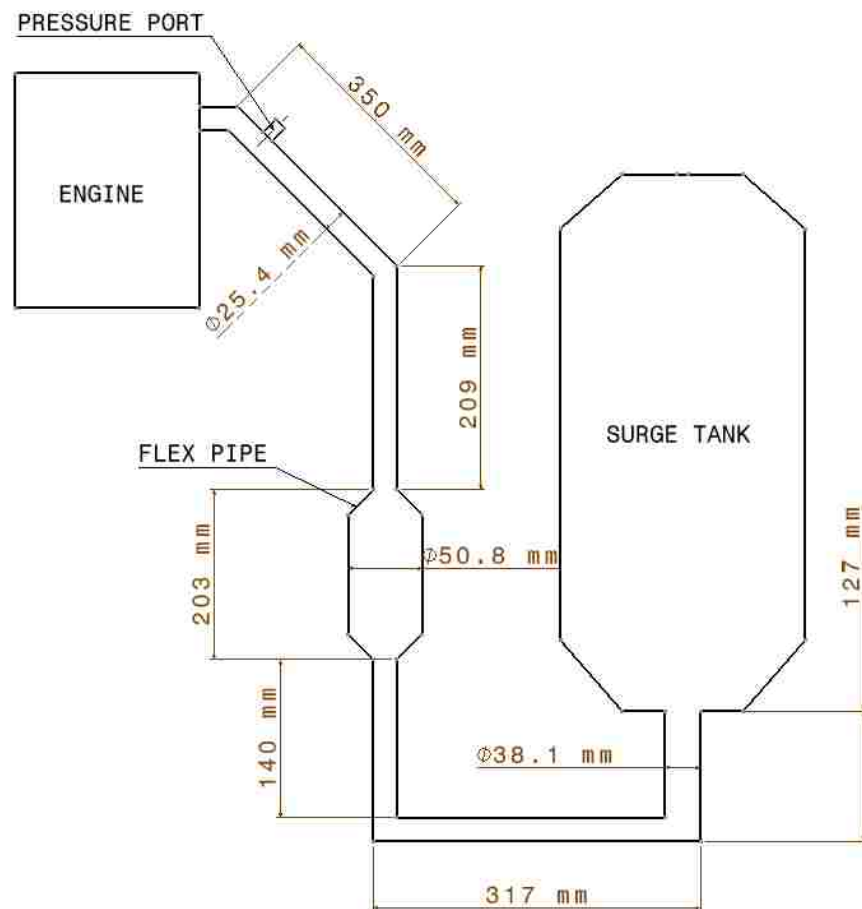


Figure 4.2: Ford Puma Exhaust System Schematic
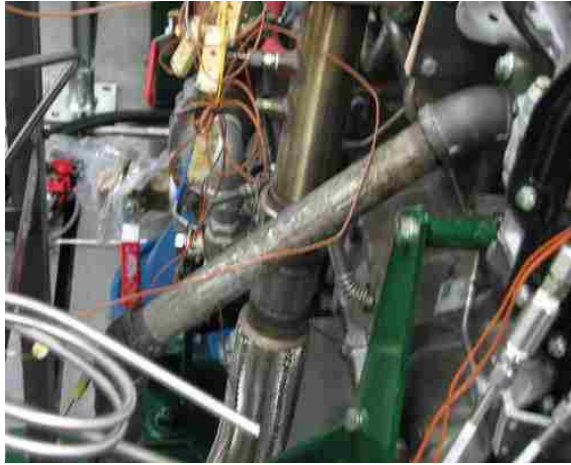
Figure 4.3a: Unmodified Puma Exhaust Pipe    Figure 4.3b: Modified Puma Exhaust Pipe
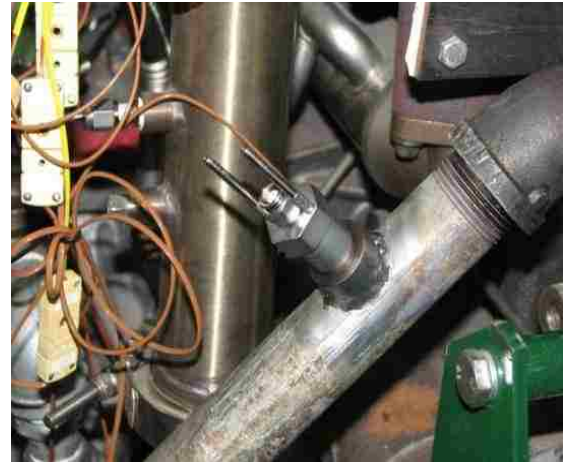
**4.2 Single Cylinder I-TEC**

The single cylinder research engine, donated by Navistar, differs vastly from the Ford Puma specifications. This engine has a greater displacement per cylinder, and a considerable lower compression ratio, but both use a common rail for the injection systems. Table 4.2 shows the single cylinder research engine specifications.

| SINGLE CYLINDER I-TEC SPECIFICATIONS | |
|---|---|
| Cylinders | 1 |
| Type | 4-Stroke |
| Displacement | .78 Liters |
| Bore | 96 mm |
| Stroke | 107.8 mm |
| Compression Ratio | 14.3:1 |
| Injection System | Common Rail |

Table 4.2: I-TEC Specifications

*Layout*

In the same way as the Ford Puma engine, the air supplied comes from a compressed air tank and controlled by a valve. The air then passes through the flow meter and is dumped into the intake surge tank. The intake system on the single cylinder can be switched so that the air supplied comes from ambient conditions within the dyno cell. On the exhaust side, exhaust gas recirculation (EGR) is controlled the same way as the Ford Puma engine by using an EGR and backpressure valve. Figure 4.4 shows a detailed layout of the single cylinder research engine.
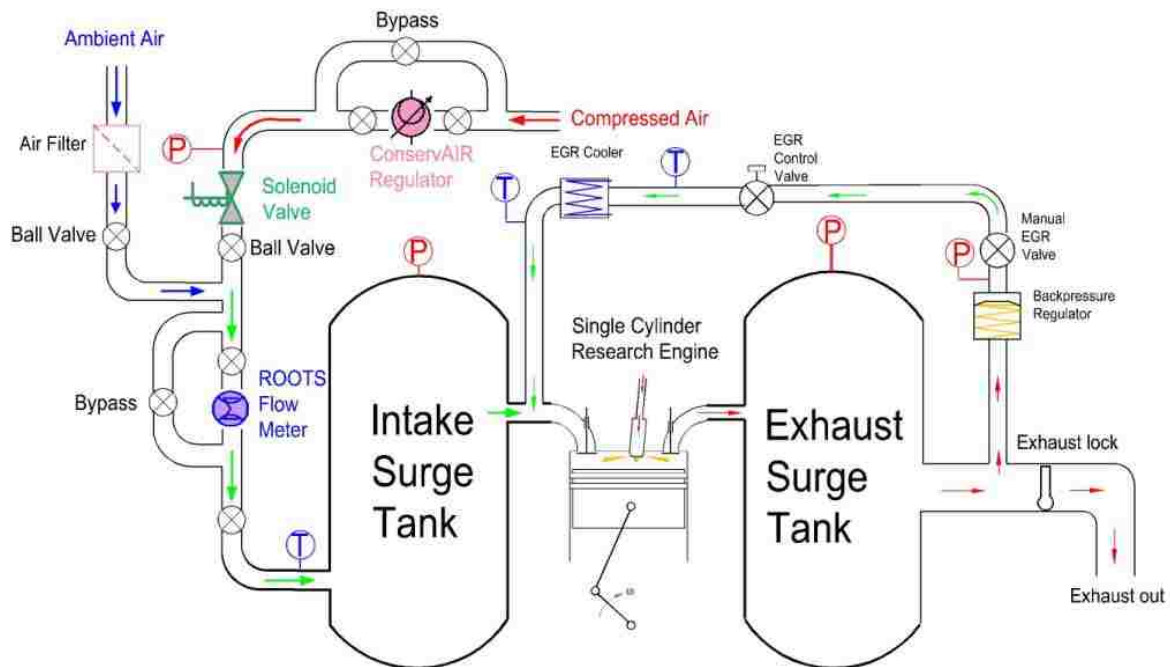


Figure 4.4: ITEC Schematic

In similar fashion the exhaust system consists of circular pipes leading up to the surge tank. The pipe directly connected to the cylinder head at the exhaust ports has a diameter of 1.5 in and a length of 15 in. It is the one used for the pressure port for the transducer. Adjacent to the pressure port, a K-type thermocouple is installed to accurately measure exhaust temperature. Figure 4.5

shows the engine on the left, and the exhaust system on the right. More specifically it shows the pipe that was modified to adapt it with the pressure transducer. Figure 4.5 shows the new modified exhaust pipe with both the thermocouple and pressure port. The pressure port is located at about 153 mm from the exhaust valves.
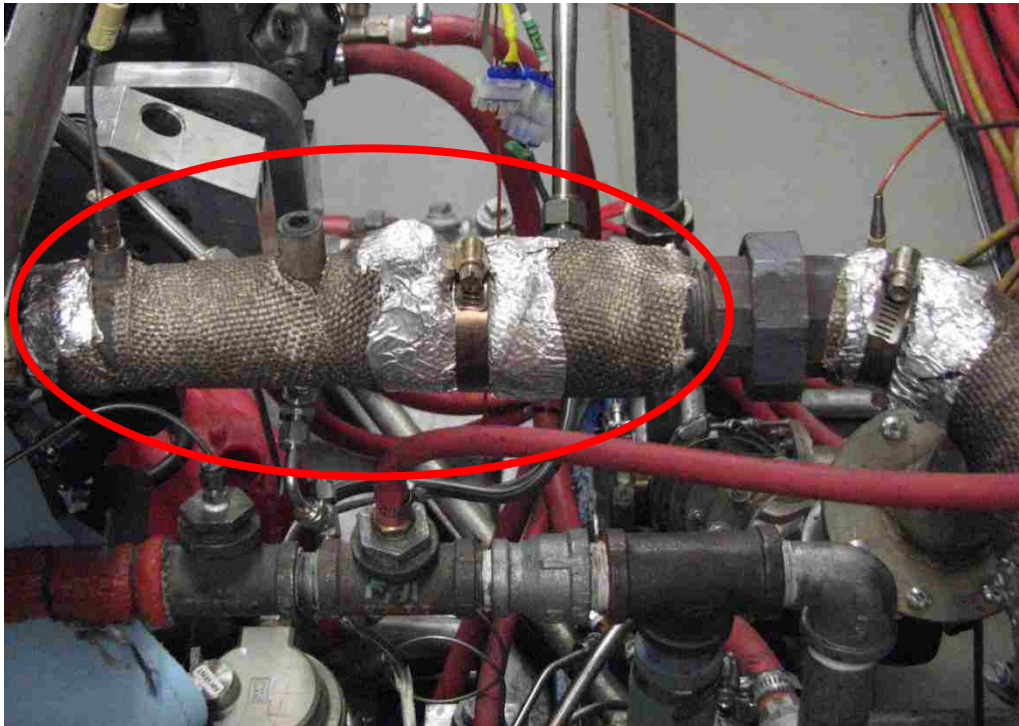


Figure 4.5: Unmodified I-TEC Exhaust Pipe



Figure 4.6: Modified I-TEC Exhaust Pipe

## 4.3 Pressure Transducer System

The pressure transducer used is a Kistler 4075 A10, shown in Figure 4.7. It has a pressure range of zero to ten bar. The output voltage is zero to ten volts after the amplifier, which equates to a one to one ratio. The sensor requires a cooling adapter when used on exhaust systems, due to the high temperatures. Though, the transducer is not limited for exhaust system use. The pressure range for the pressure transducer is more than the desired, and will affect the resolution of the measurement. Typical exhaust pressure seen in exhaust systems for diesel engines under moderate load does not exceed 2 bar absolute. More specific pressure transducer specifications are shown in Table 4.3.



Figure 4.7: Kistler 4075A10 Pressure Transducer (From [18])

| KISTLER 4075A10 SPECIFICATION | |
|---|---|
| Connection | M12x1 |
| Compensated Operating Temp | $20...120^o\,C$ |
| Min/Max Temperature | $0/140^o\,C$ |
| Measuring Range | 0… 10 bar |
| Overload | 25 bar |
| Sensitivity at lcal | 50 mV/bar |
| Natural Frequency | > 120 kHz |
| Linearity | < 0.3 % |
| Tightening Torque | 12… 20 N-m |
| Weight | 28 g |

Table 4.3: Kistler 4075A10 Specifications (Adapted from [18])

As stated above, the sensor requires the Kistler water cooled adapter 7075 shown in Figure 4.8. The adapter is a male M14 x 1.25, which is a rare thread pattern to acquire. A bung needs to be made, tapped, and welded onto the exhaust pipe with the correct female thread. When mounting the adapter onto the exhaust pipe, the end of the adapter facing into the pipe, needs to be positioned flush with the inner diameter of the pipe as shown in Figure 4.9.
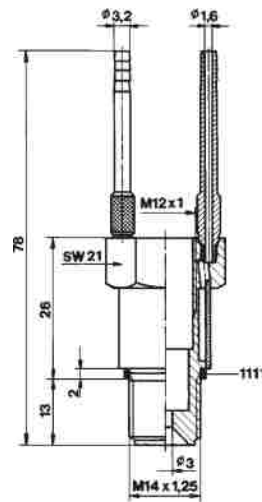


Figure 4.8: Kistler 7075 Drawing (Taken from [19])



Figure 4.9: Kistler Pressure Transducer Assembly (Taken from [19])

Specific tapping geometry exists for proper fitment and sealing [19]. A tightening torque range of 10 to 15 N-m is required for proper installation of the water cooled adapter. The two water ports on both sides of the adapter shown in Figure 4.9 only require hand tightening. A small o-ring ensures sealing, and over tightening can cause the o-ring to tear and be prone to leakage.

In order to read the analog signal from the pressure transducer, an amplifier is required. The amplifier used is a Kistler 4618A0 shown in figure 4.10. An input voltage range of 18 to 30 VDC is required to operate the amplifier and pressure transducer.



Figure 4.10: Kistler Amplifier 4618A0

### 4.3.1 Water Cooling Loop

A water cooling system was made in order to keep the transducer cool during operation. It is designed to be a portable system since two engine platforms were used. The tank, pump, pressure gauge, and water lines, are all within the portable unit to simplify relocation to each dyno cell. Figure 4.11 shows the portable water cooling system.



Figure 4.11: Water Cooling System

The whole structure, including the water tank consists of aluminum in order to remove heat and to reduce weight. The water supply temperature to the water cooled adapter cannot exceed $50^o C$ according to Kistler. Therefore, the water tank has a 3 gallon capacity which ensured an operating time of an hour before the water temperature supplied reaches $50^o C$. This calculation is based on the required flow rate specified by Kistler of 0.5 L/min and an initial water temperature of $25^o C$. During engine operation, a bath of ice chilled water was used to ensure a safe operating temperature for the pressure transducer. At the same time, water temperature inside the tank was constantly monitored by a T-type thermocouple positioned near the supply port of the tank. Figure 4.12 shows the water cooling circuit of the system.
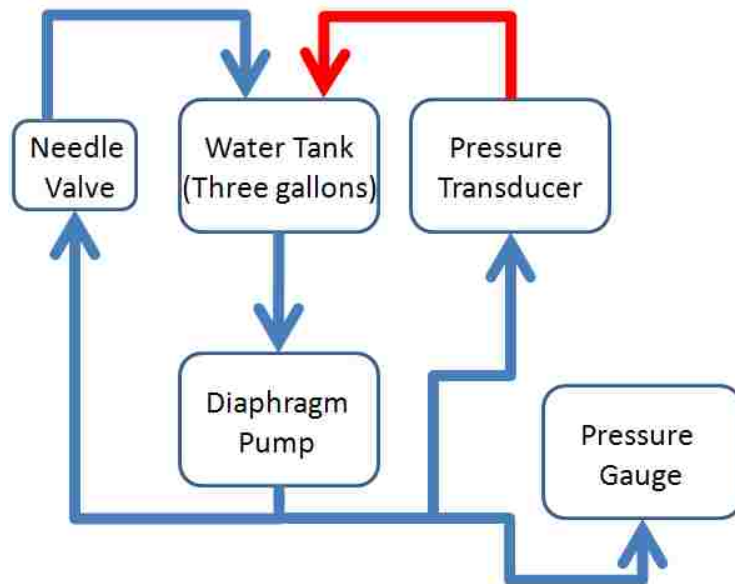


Figure 4.12: Water Cooling Loop

All the water lines consist of Teflon tubing with two different diameters. The water cooled adapter requires 1/8 in tubing, while the rest of the lines are ¼ in tubing. The water flows from the water tank into the diaphragm pump, passing through a needle valve to control the water supply. The pump then supplies the pressure transducer, pressure gauge, and the return line. The return line contains another needle valve, controlling the pressure in the system to give the

desired flow rate. In this case, a graduate cylinder was used in order to determine the required pressure to reach the desired flow rate of .5l/min. In order to minimize the pressure drop in the cooling loop, only a short section of the required 1/8 in tubing for the cooling adapter was used, and connected to the main ¼ in tubing by Swagelok adapters. The return line from the adapter connects to the tank through the same port as the bypass.

The water pump used is a KNF 1100 series diaphragm pump, shown in Figure 4.13. It requires a 12 VDC power supply, with a limiting flow rate of 1.3 l/min, and maximum pressure head of 85 psig. The pump supplies more than the required flow rate but the pressure is necessary since the small 0.125 in Teflon tubing used at the water cooled adapter, could induce a greater pressure drop than expected.



Figure 4.13: KNF 1100 Diaphragm Pump

**4.3.2 Power Supply**

In order to power both the pressure transducer, and the water pump, a common power supply box was built that is capable of supplying four different voltages:

1) 24 V

2) 5.5 V

3) 12 V

4) 3.3 V

Inside the main power supply box, two individual power supplies exist. The first one has been taken from a computer with power rating of 400 watts. The second power supply, only supplies 24 volts, with a power rating of 450 watts, which is used for the pressure transducer. Each of the four voltages supplied from these two boxes, have individual on/off switches with a light indicator, and two sets of banana connectors. The main power for the box is received from the wall at 120 VAC, and it is controlled by a main switch on the back of the box. The main switch is also equipped with LED indicator. In order to ensure proper cooling, two fans were installed. The first fan draws air in, while the second draws it out of the box. The figures below show the system in detail.



Figure 4.14: Power Supply Front View



Figure 4.15: Power Supply Back View



Figure 4.16: Power Supply Inside View

**4.4 Simulation**

Ricardo Wave is the simulation software used to study pressure wave action, in engine manifolds. It is a gas dynamic simulation tool applied to engine research and development. It is a convenient tool used to study the effect of different operating modes, without the expense and required time associated with empirical work. The following sections will cover the complete Ricardo model shown in Figure 4.17.
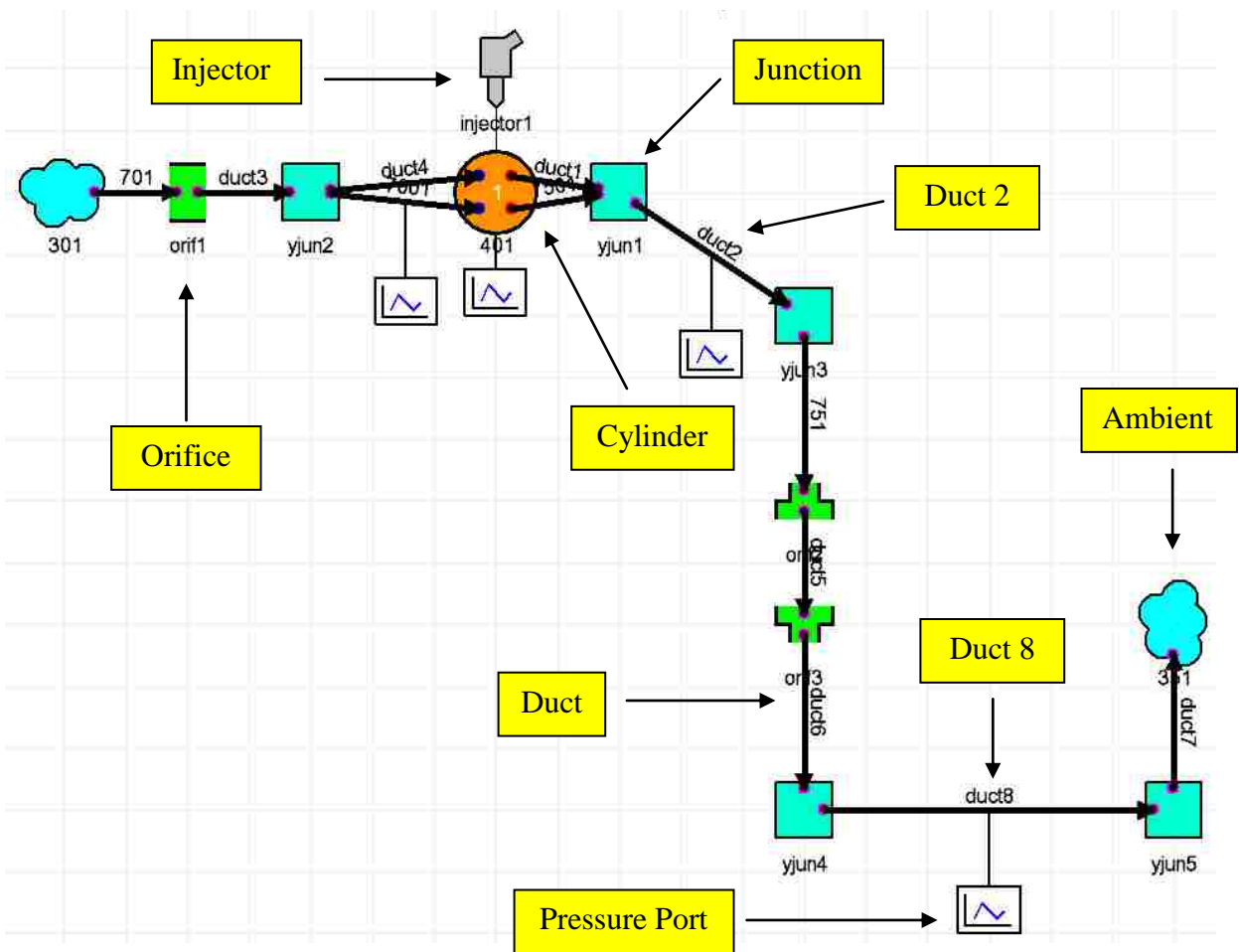


Figure 4.17: Ford Puma Ricardo Simulation Model [20]

### 4.4.1 Engine Model

Since most of the research tests were conducted on the Ford Puma engine, the simulation work was set-up using the Ford Engine specifications. Since research is conducted on cylinder number one, a single cylinder simulation model is used. The geometric specifications of the Ford Puma engine used in the simulation model are given in Table 4.4.

| SIMULATION ENGINE SPECIFICATIONS | |
|---|---|
| Cylinders | 4 |
| Type | 4-Stroke |
| Displacement | 1.998 Liters |
| Bore | 86 mm |
| Stroke | 86 mm |
| Compression Ratio | 18.2:1 |
| Valves per Cylinder | 4 |
| Injection System | Delphi Common Rail (1600 bar) |
| Exhaust Valve Diameter | 28 mm |
| Intake Valve Diameter | 33.4 mm |
| Intake Valve Lift | 12.5 mm |
| Exhaust valve Lift | 8.64 mm |
| Intake Valve Opening | $690^o$ |
| Intake Valve Closing | $250^o$ |
| Exhaust Valve Opening | $498^o$ |
| Exhaust Valve Closing | $68^o$ |

Table 4.4: Simulation Engine Specifications

There are certain specifications that were not available; such as valve geometry, timing, and lift. In order to account for these in the simulation model, specifications on similar displacement diesel engines were used, with the exception of exhaust valve timing. The timing on the exhaust valves was attained by the empirical results. Figure 4.18 shows the geometry specification window of the simulation model.
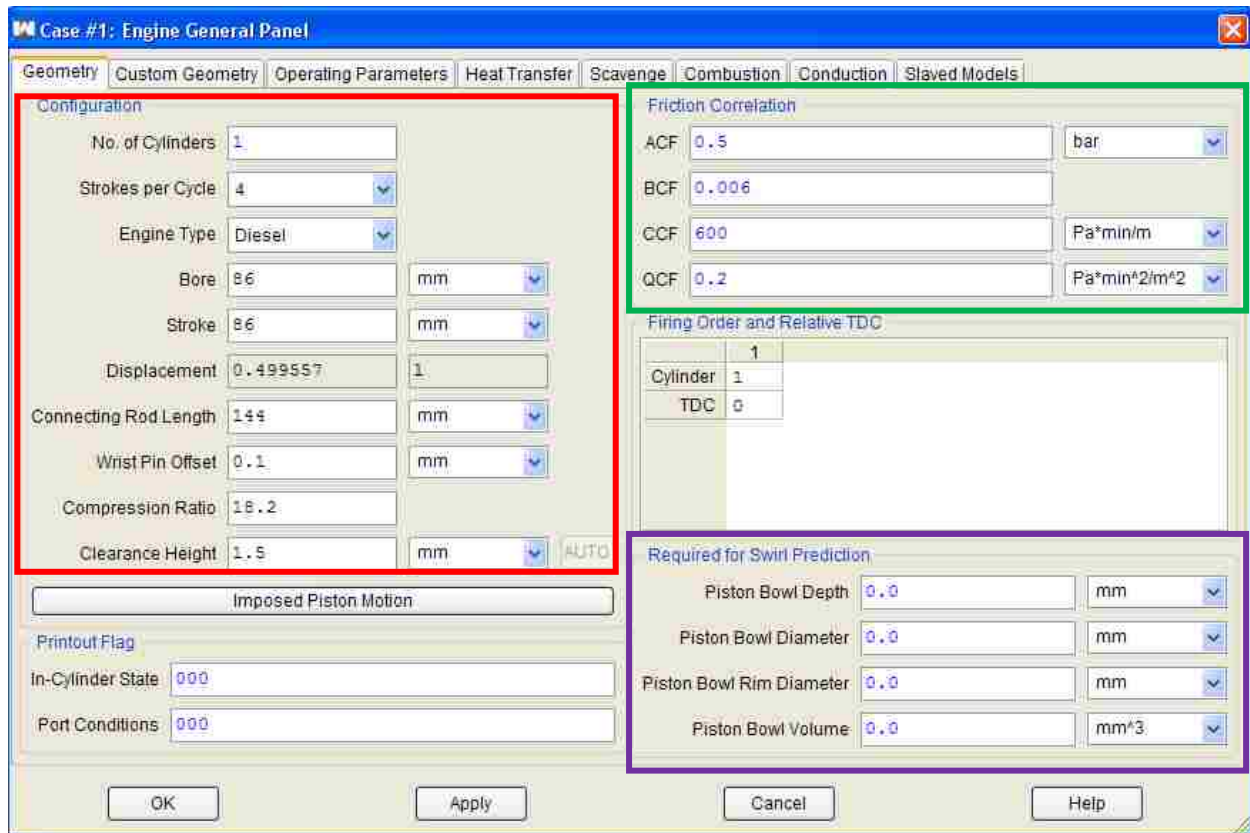
Figure 4.18: Ricardo Geometry Specification Window [20]

The basic geometric engine parameters are enclosed by the red box, on the top left. The information enclosed by the green box, includes the friction parameters. Since all of these parameters are not known for the Ford Puma engine, the default values are used. Below the friction correlation parameters, the firing order is set zero degrees top dead center (TDC). The purple box below the firing order shows the swirl parameters. Again, no information is available for Ford Puma engine therefore, no swirl ratio is used. The swirl ratio affects the combustion model, but in this case the model used in the simulation requires no swirl ratio input, as it depends on the empirical data. The combustion model is explained in the next section.

### 3.4.2 Combustion Model

There are various combustions models that are available for use in Ricardo. In order to accurately model the Ford Puma engine at each operating condition, empirical data from the engine is uploaded into the simulation model. More specifically, a heat release curve at each operating mode is implemented into the simulation. A heat release curve is necessary for all operating engine conditions that are simulated. The heat release curve is then used to calculate an in-cylinder pressure trace. When each heat release curve for the different engine conditions are implemented into the simulation model, Ricardo normalizes the curve, and a certain degree of calibration is required to match the empirical in-cylinder pressure data. There are certain scaling parameters that need to be adjusted, including start of ignition and fueling. Figure 4.19 shows a heat release curve for a certain engine operating mode and Figure 4.20 shows the simulation combustion profile window.
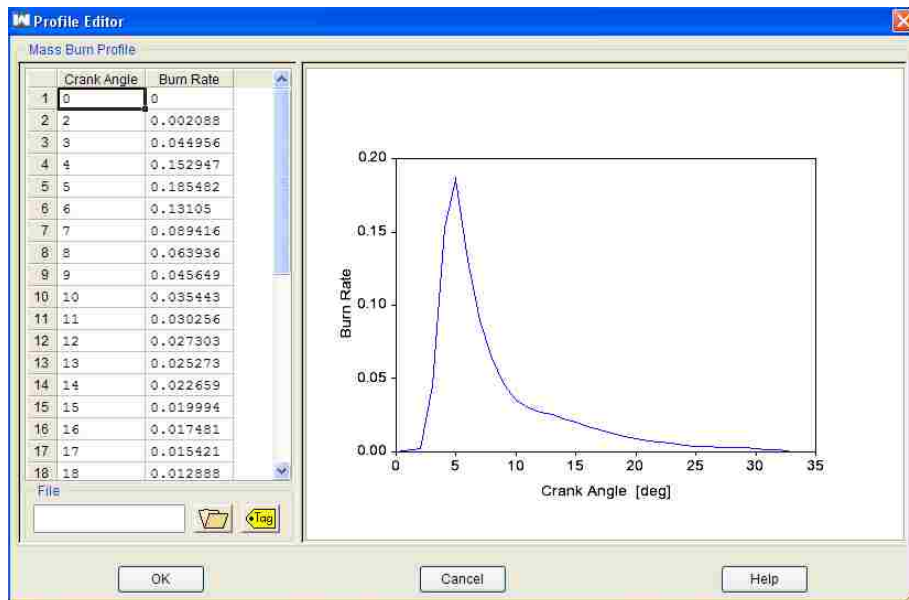


Figure 4.19: Ricardo Heat Release Input Window [20]
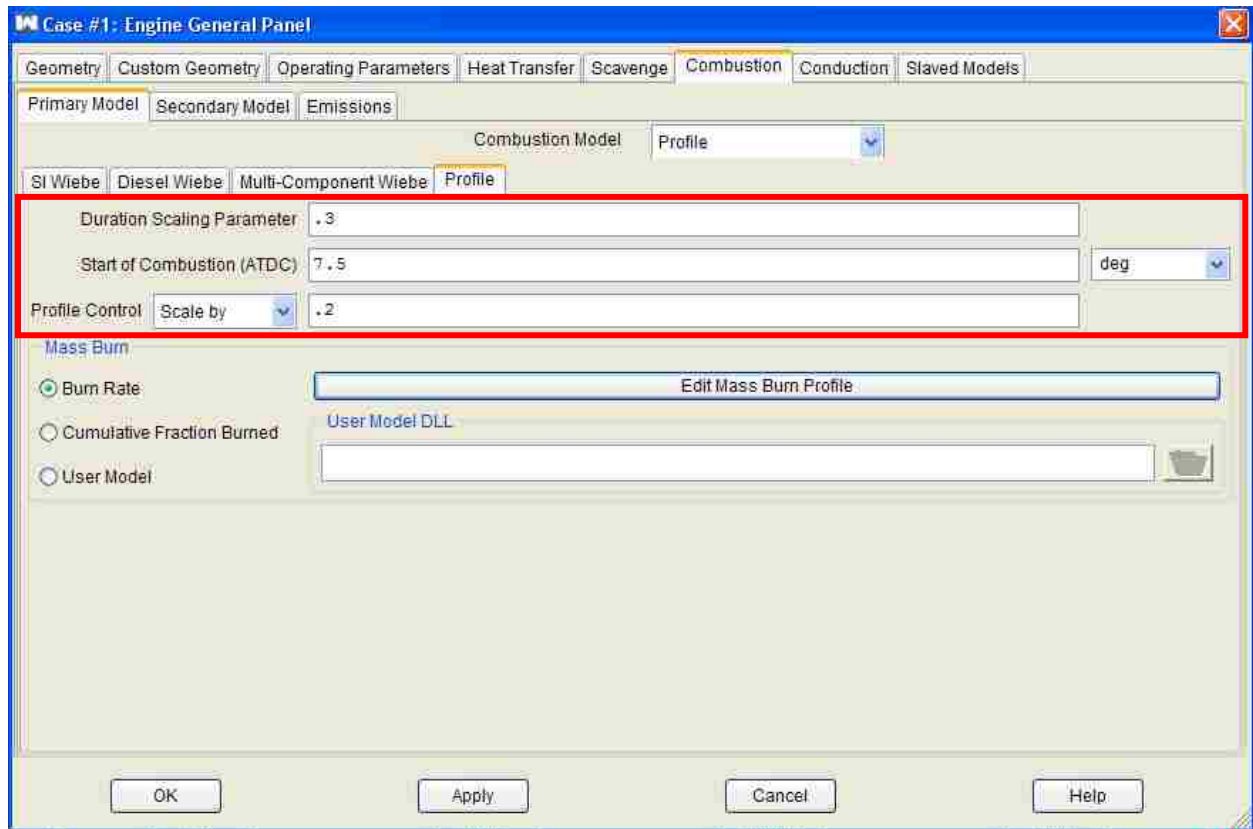
Figure 4.20: Ricardo Combustion Profile Window [20]

The combustion model used is referred to as "Profile". The information enclosed by the red box contains three main parameters: duration scaling parameter, start of combustion, and profile control. The duration scaling parameter adjusts the combustion duration, so it will either widen or thin the combustion profile. The start of combustion is acquired by the empirical data and the profile control parameter adjusts the vertical scaling of the entire profile. These parameters, and adjustment of the fueling, need to be adjusted in order to match the empirical in-cylinder pressure trace, to accurately model the operating conditions. The in-cylinder pressure needs to be fine tuned to the match the empirical data, as pressure wave actions depends on the pressure present in the cylinder, at the time of the exhaust valve opening (EVO).

50

### 4.4.3 Injector Model

The injector specified in the model, uses an amount of fuel per shot in milligrams. A required injection profile and injection pressure is needed, and can be adjusted depending on the operating conditions. Figure 4.21 and 4.22, show the injection profile, and one of the pressure profiles used respectively.
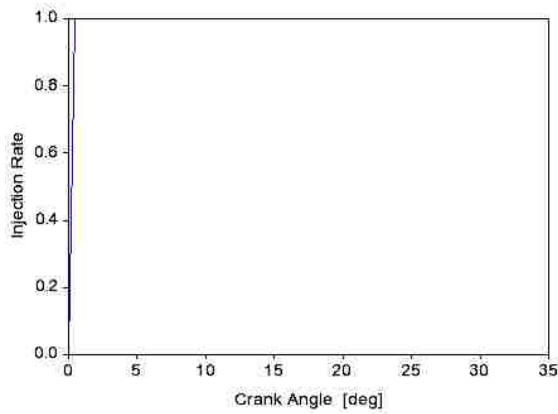


Figure 4.21: Injection Rate [20]                    Figure 4.22: Injection Pressure [20]
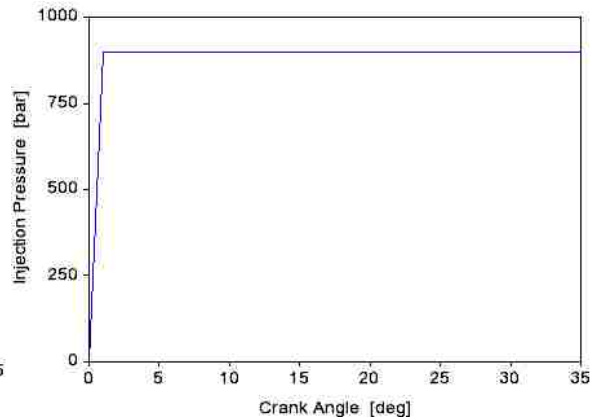
The injection rate profile shown is normalized, meaning that the injection rate attains its full value, within a degree of start of injection (SOI). The injection pressure profile is defined in bar, and also reaches a value of 900 bar, within a degree for this given case.
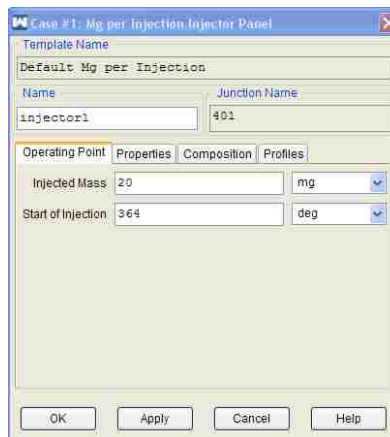


Figure 4.23: Ricardo Injector Model Window [20]

Figure 4.23, shows the injector panel window where both injected mass and start of injection, can be defined. Both parameters are acquired, from the empirical data for each operating point, and implemented into the model. Once injector parameters are implemented into the simulation the scaling parameters for the combustion model can be fined tuned. There are other parameters within the injector model that can be modified, such as temperature and liquid fraction among others, but can be accounted for by the scaling parameters in the combustion model in order to match the in-cylinder pressure trace.

**4.4.4 Intake System Model**
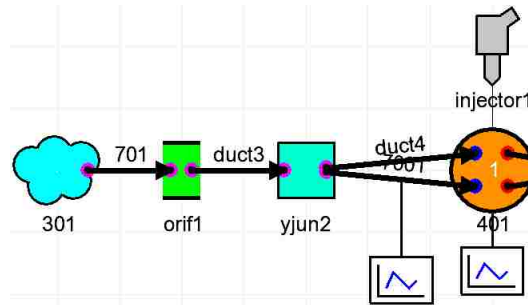


Figure 4.24: Simulation Intake System [20]

The intake system shown in figure 4.24, consists of numerous ducts and junctions which represent the empirical geometric layout. Icon 301 represents ambient conditions and is primarily used to control the amount of boost. Parameters such as air composition, temperature, pressure, and discharge coefficients, can be modified depending on the operating conditions. Icon "orif1," represents an orifice which is used to change duct diameters. Icon "yjun2" represents a complex junction used to connect various ducts together at specified angles as shown in Figure 4.25. The arrows represent the ducts and parameters, such as length, heat transfer, friction, and diameter that are adjusted in order to simulate actual conditions. Table 4.5 shows the lengths and

52

diameters used in the model, which correspond to the actual dimension of the Ford Puma engine. Heat transfer and friction coefficients are not known for the actual set-up, therefore default parameters were used initially, and then used in the fine tuning, after comparing both the empirical and simulation results.
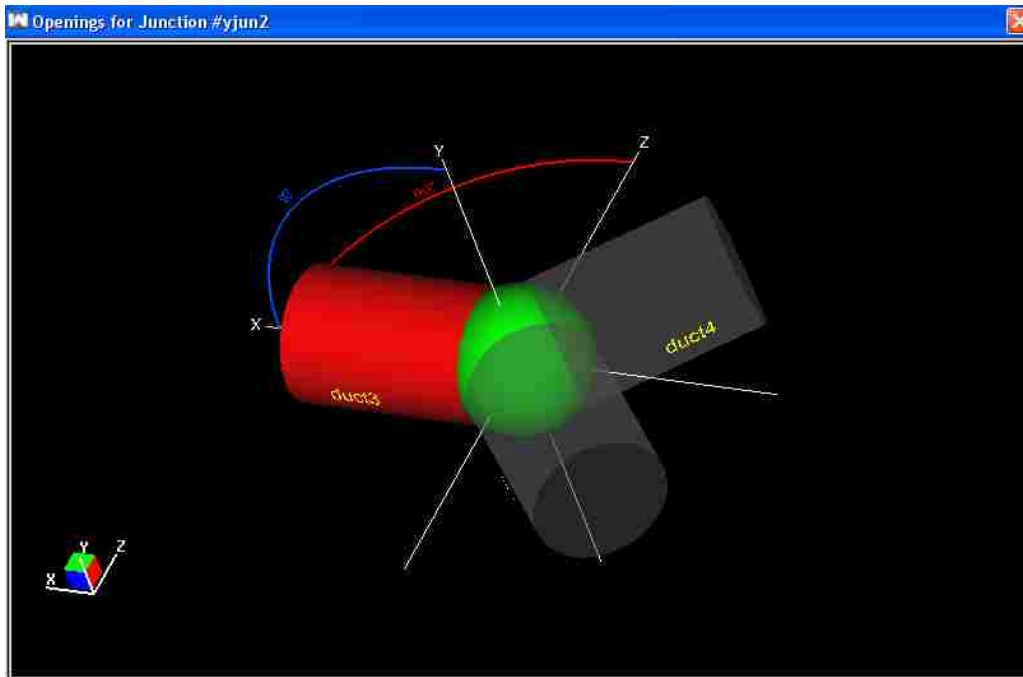


Figure 4.25: Complex Junction [20]

| INTAKE DUCT LENGTH | | |
|---|---|---|
| Duct | Length (mm) | Diameter (mm) |
| 701 | 1000 mm | 36 |
| Duct 3 | 100 mm | 36 |
| Duct 4 | 50 mm | 48 |
| 7001 | 50 mm | 48 |

Table 4.5: Intake Duct Lengths

**4.4.5 Exhaust System Model**
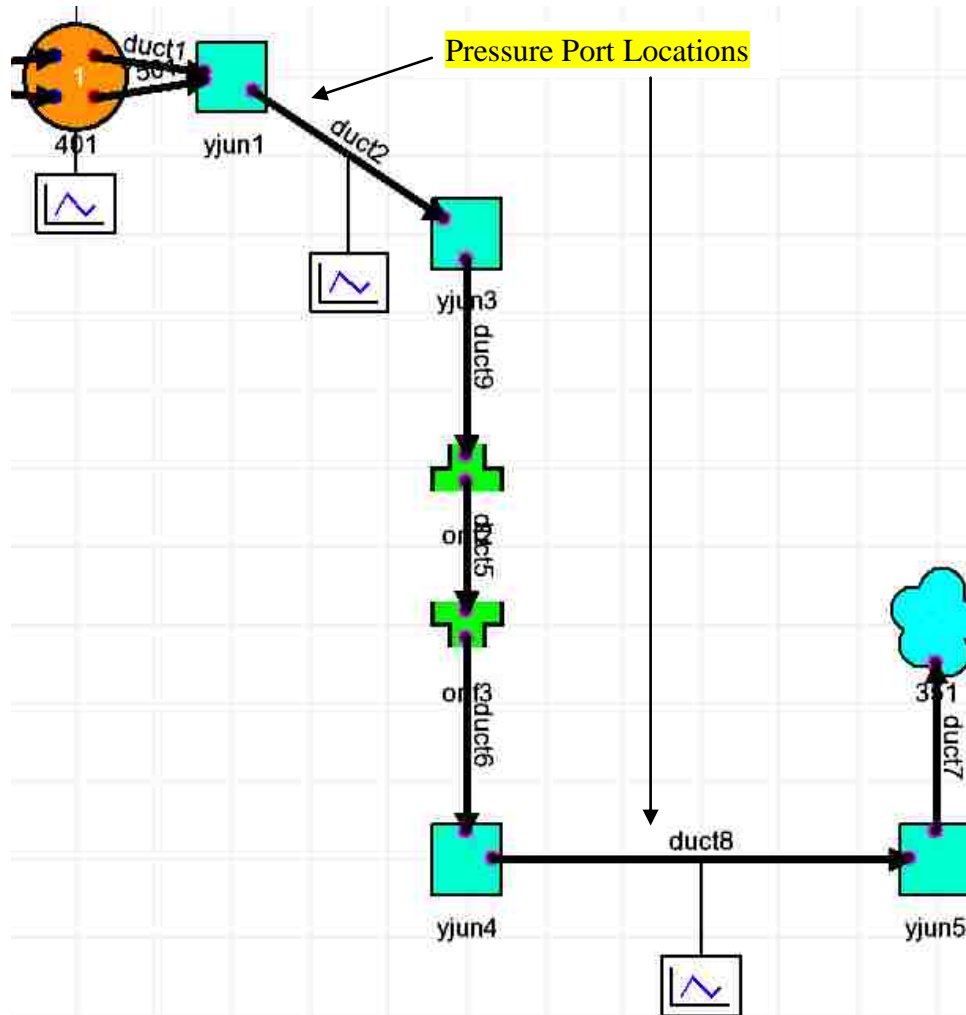


Figure 4.26: Simulation Exhaust System [20]

In the same way as the simulated intake system, complex junctions and orifices connect the complex exhaust piping, in the same manner as the empirical set up. The ducts to note are duct 1 and 501, which are the ones coming off directly from the exhaust valves. These ducts as well as the intake ducts connected to the valves, represent the port length inside the cylinder head. The actual cylinder head port configuration is not the same as the circular configuration used, and will add error to the simulation. Table 4.6 shows the appropriate length and diameters used for each duct in the exhaust system.

| EXHAUST DUCT LENGTHS | | |
|---|---|---|
| Duct | Length (mm) | Diameter (mm) |
| Duct 1 | 30 | 30 |
| Duct 2 | 400 | 25.4 |
| Duct 5 | 203.2 | 50.8 |
| Duct 6 | 139 | 25.4 |
| Duct 7 | 127 | 38.1 |
| Duct 8 | 319 | 25.4 |
| Duct 9 | 209 | 25.4 |
| 7501 | 30 | 30 |

Table 4.6: Exhaust Duct Lengths

## 4.5 Portable Dynamometer Research Platform

A dynamometer research platform was needed in order to study pressure wave actions in depth, due to the limiting use of the current research engines. A dynamometer research platform needed to be designed and built, to serve solely for research in gas exchange processes for internal combustion engines. Due to limitation in space, the dynamometer platform needed to be portable and on wheels, but when in use had to be fastened down. There was also limitation on main components used for the set-up, such as the AC motor and torque transducer. The system needed to be pulley-belt driven to make alignment simple. This type of system also gives the versatility of swapping different engines to use. The following sections will cover the design, building, and preliminary testing of this dynamometer research platform. Figure 4.27 shows the 3-D drawing of the completed system.

## 4.5.1 Components



| Dynamometer Component List | | | |
|---|---|---|---|
| 1 | Kart | 7 | Pulley |
| 2 | AC Motor | 8 | Bed Plate |
| 3 | Torque Sensor | 9 | Safety Guard |
| 4 | Pillow Block Bearings | 10 | Bearing Block |
| 5 | Couplers | 11 | Rec. Beam Supports |
| 6 | Shaft | 12 | Cross Plate Supports |
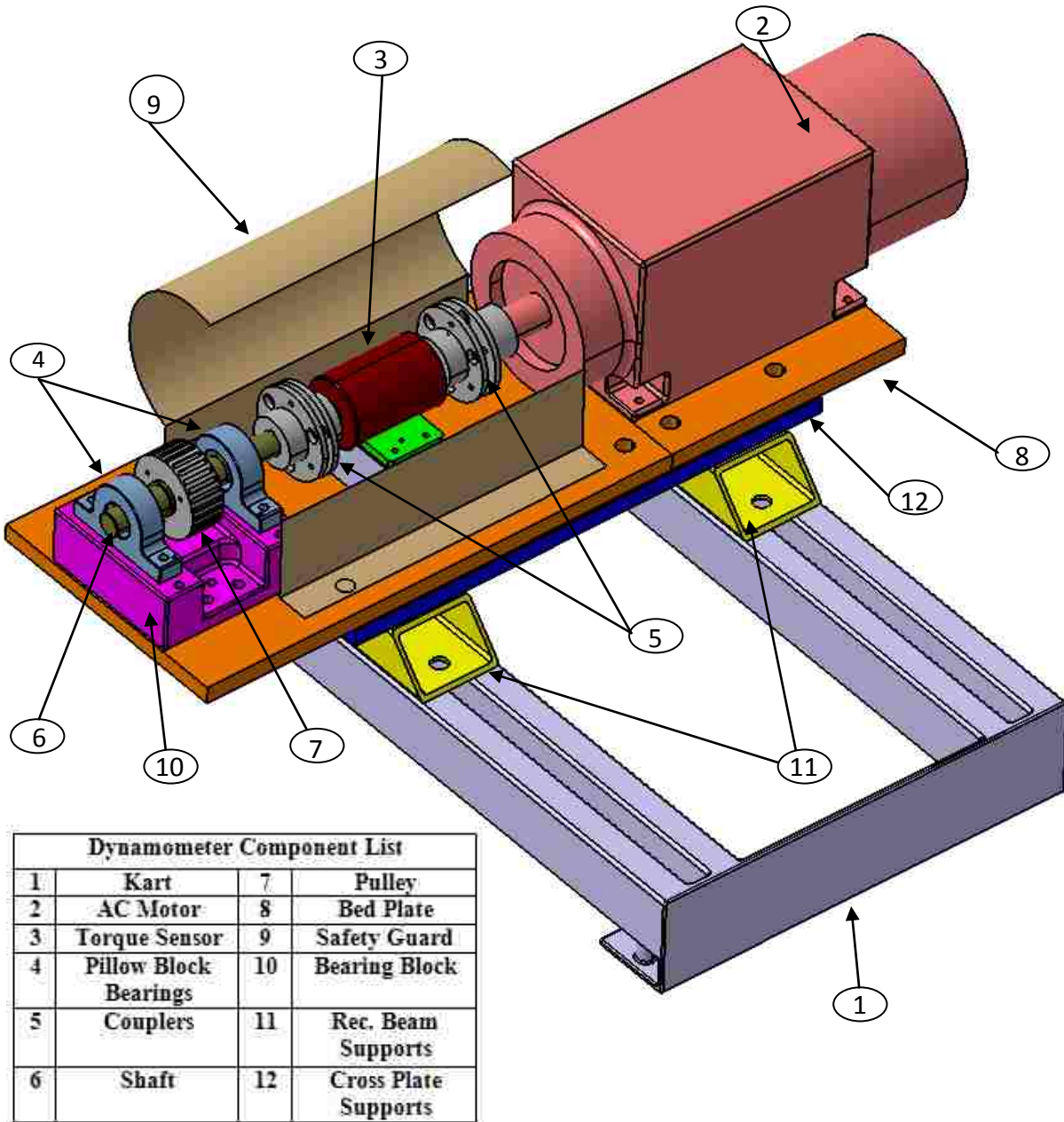
Figure 4.27: Dynamometer Research Platform [21]

### 4.5.2 AC Motor

The AC motor used, shown in Figure 4.28, is capable of handling up to 60 N-m of torque, with a speed limitation of 3600 rpm. It uses a UNICO vector controlling unit for its operation.



Figure 4.28: AC Motor

### 4.5.3 Torque Transducer& Amplifier

In order to monitor and control torque output, the torque sensor used is a Honeywell 1104. It is in-line rotary ring sensor design, used in a variety of motor testing applications shown in Figure 4.29.

Figure 4.29: Lebow 1104 Torque Transducer

This specific model has a capacity of handling up to 1000 lb-in of torque, consisting of about 53% more torque capacity than the AC motor. The performance characteristics are shown in Table 4.7.

| PERFORMANCE CHARACTERISTICS | |
|---|---|
| Characteristics | Measure |
| Torque Range | 100-1000 lb-in |
| Non-Linearity | $\pm 0.1$ % of rated output |
| Hysteresis | $\pm 0.1$ % of rated output |
| Repeatability | $\pm 0.05$ % of rated output |
| Output at Rated Capacity | $\pm 2$ mV/V (nominal) |

Table 4.7: Torque Transducer Specifications [22]

The torque sensor requires an amplifier since the output from the sensor is in mV. The sensor recommended by 'Daytronic' and approved by Ford engineers, consists of a DIN type amplifier, with an output scale of either zero to five volts, or zero to ten volts. The full specifications are shown in Table 4.8.

| AMPLIFIER SPECIFICATIONS | |
|---|---|
| Power Requirements | 11-28 Vdc : 2 watts Max |
| Transducer Types | Conventional 4-Arm strain gauge bridges, 120 Ω to 10 kΩ; zero range is 100% of the stated full scale; a screw terminal is provided for use-supplied shunt calibration resistor. |
| Input Ranges | 0.5 to 5mV/V or 1 to 10 mV/V via internal switch settings. |
| Dimensions | 114.5 mm D x 22.5 mm W x 99.0 mm H |
| Housing | DIN mount housing; non-removable screw terminals |
| Operating Relative Humidity | 5% to 95%, non-condensing |
| Operating Temperature Range | $-10^o C$ to $70^o C$ |

Table 4.8: Daytronic Amplifier Specifications [23]



Figure 4.30: Daytronic Amplifier

### 4.5.4 Design

The design and full details on the portable dynamometer research platform are shown in the appendix.

**4.6 Orifice Flow Meter**

The orifice meter is a precision instrument used to study flow rates based on differential pressure across an orifice. As an unknown fluid flows along a straight smooth pipe, and passes through an orifice plate, a certain static pressure drop occurs. This static pressure drop corresponds to a certain flow rate for the working fluid. The same device can be used to calibrate pressure sensors, based on a known flow rates. The orifice meter is used to study intake flow, and verify the accuracy of modern mass flow sensors in IC engines, which in turn affect engine performance. The design is based on the ISO 5167-2:2003 design guidelines. The orifice meter was designed, built, and tested jointly with Marko Jeftic. The following sections cover the design, final product, and calibration.

Three types of orifice meter designs are outlined in the guidelines. They differ by the location where the pressure ports are located, to record the static pressure drop.

1) D and D/2 pressure tapings
2) Flange tapings
3) Corner tapings

The D and D/2 pressure tapings was chosen, since it involves less complicated pressure taping geometry, but both will achieve the same level of accuracy. The following section covers the relationships used to design and calculate the working parameters for D and D/2 pressure type orifice design.

## 4.6.1 Theory

The relationship relating pressure drop to mass flow rate is given by the following [24]:

$$q_V = \frac{q_m}{\rho}$$

Where $q_m$ and $\rho$ are mass flow rate and density respectively.

The mass flow rate is defined as [24]:

$$q_m = \frac{C}{\sqrt{1-\beta^4}} \, \varepsilon \frac{\pi}{4} d^2 \sqrt{2\Delta p \rho_1}$$

$C$ : Discharge Coefficient

$\beta$ : Diameter ratio

$d$ : Orifice diameter

$\Delta p$ : Pressure difference

$\rho$ : Density

$\varepsilon$ : Expansibility factor

### 4.6.1.1 Diameter Ratio

The diameter ratio is defined as the diameter of the orifice, divided by the inner diameter of the pipe. Limits exist for this ratio, and the chosen minimum and maximum diameter ratios will depend on the amount of flow rate desired [24].

$$\beta = \frac{d}{D}$$

A minimum of 50 mm and a maximum of 1000 mm is the limitation for the inner diameter of the pipe.

### 4.6.1.2 Discharge Coefficient

It is defined as the ratio of the mass flow rate at the discharge of the orifice over the mass flow rate of a nozzle that expands the same working fluid from the same initial to final conditions. The discharge coefficient can be calculated by the following relationship [24]:

$$\begin{aligned} C = &.5961 + .0261\beta^2 - .216\beta^8 + .000521\left(\frac{10^6 \beta}{\mathrm{Re}_D}\right)^{.7} + (.0188 + .0063A)\beta^{3.5}\left(\frac{10^6}{\mathrm{Re}_D}\right)^{.3} \\ &+ \left(.043 + .080e^{-10L_1} - .123e^{-7L_1}\right)(1 - .11A)\frac{\beta^4}{1 - \beta^4} - .031\left(M_2' - .8M_2'^{1.1}\right)\beta^{1.3} \\ &+ .011(.75 - \beta)\left(2.8 - \frac{D}{25.4}\right) \end{aligned}$$

Where,

$$L_1 = \frac{l_1}{D} = 1$$

$$L_2' = \frac{l_2'}{D} = 0.47$$

$$M_2' = \frac{2L_2'}{1 - \beta}$$

$$A = \left(\frac{19000\beta}{\mathrm{Re}_D}\right)^{.8}$$

### 4.6.1.3 Expansibility Factor

It is defined by the following relationship [24]:

$$\varepsilon = 1 - \left(.351 + .256\beta^4 + .93\beta^8\right)\left[1 - \left(\frac{p_2}{p_1}\right)^{1/k}\right]$$

Experimental results in determining the expansibility factor exist for air, steam, and natural gas but equation above can be used to determine the expansibility factor for other gases. The only limitation is that the pressure ratio has to be less or equal to 0.75. The ISO 5167-2:2003 design guidelines shows a table for the expansibility factor based on specific heat ratio, pressure ratio, and diameter ratio.

### 4.6.1.4 Limitations

For "D and D/2" tapings the following limitations need to be enforced [24]:

- $d \geq 12.5\,mm$

- $50 \geq D \geq 1000\,mm$

- $0.1 \leq \beta \leq 0.75$

- $\mathrm{Re}_D \geq 5000\ for\ 0.1 \leq \beta \leq 0.56$

- $\mathrm{Re}_D \geq 16000\beta^2\ for\ \beta > 0.56$

### 4.6.1.5 Design

The design and full details on orifice flow meter are shown in the appendix.

## CHAPTER V

## 5   RESULTS AND DISCUSSION

### 5.1 Simulation Results

The following simulation results study pressure wave actions in the exhaust manifold, at various engine operating conditions. Some operating conditions will be the same as those of the empirical results; however they will not be compared until a later section. Different variables shown in Table 5.1 have been simulated to see the effects on pressure wave actions.

| PARAMETERS OF STUDY | |
|---|---|
| 1 | RPM |
| 2 | Load |
| 3 | Backpressure |
| 4 | Runner Length |
| 5 | Runner Diameter |
| 6 | Position |

Table 5.1: Parameters of Study

### 5.1.1 RPM Sweep

The effects of different engine speeds are simulated to see the effect on the pressure wave in the exhaust manifold. Three different engine speeds are simulated while injection pressure, boost, IMEP, and backpressure are all kept the same. The start of injection (SOI) changes as engine speed changes in order to accommodate combustion and keep the same load level. The simulation operating parameters are shown in table 5.2.

| SIMULATION PARAMETERS | |
|---|---|
| | 1200 RPM |
| Engine Speed | 1500 RPM |
| | 1800 RPM |
| Injection Pressure | 900 bar |
| Boost | 1.5 bar |
| SOI | 364 to 357 |
| IMEP | ~1.6 bar |
| Backpressure | 1 bar |

Table 5.2: RPM Sweep Simulation Parameters
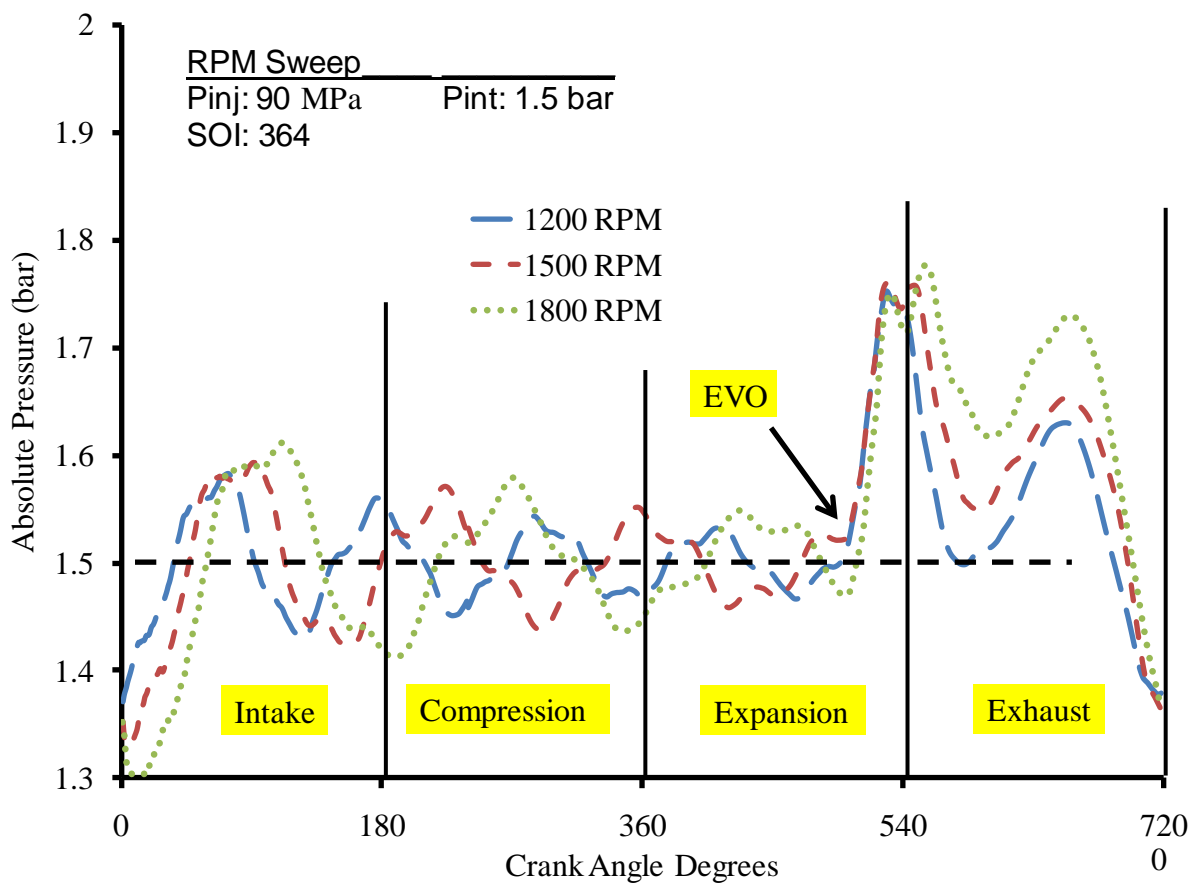


Figure 5.1: Simulated RPM Sweep

Figure 5.1 shows the pressure wave for the three engine speeds. It is easy to identify the exhaust

valve opening in all three curves by the sudden increase in pressure during the expansion stroke.

All three curves isolate among the horizontal black dotted line, which represents the exhaust

backpressure of 1.5 bar absolute. As speed is increased the exhaust gasses are expelled through the exhaust valve at a higher speed due to pressure increase, causing a frequency and phase shift. There is a $47.4^o$ forward shift between each engine speed, and therefore a total shift of $\sim 94.8^o$ exists when speed is increased from 1200 rpm to 1800 rpm, during the compressions stroke.

Due to the increase in speed, the exhaust gasses are forced out at a higher pressure, and as a result the amplitude does increase slightly throughout the cycle. This effect can greatly be observed in the second pressure peak present during the exhaust stroke for 1800 rpm, which has the highest amplitude. Frequency and phase change is the major impact on the pressure wave action as engine speed increases. The pressure wave arrives at different pressure points at the time of EVO.

## 5.1.2 IMEP Sweep

Two different load conditions are simulated at the same engine speed to study the effect of pressure wave action in the exhaust manifold. Parameters such as engine speed, injection pressure, boost, backpressure, and start of injection are kept constant. The simulation parameters are shown in table 5.3.

| SIMULATION PARAMETERS | |
|---|---|
| Engine Speed | 1200 RPM |
| Injection Pressure | 900 bar |
| Boost | 1.5 bar |
| SOI | 362 |
| IMEP | 1.6 bar |
| | 5 bar |
| Backpressure | 1.5 bar |

Figure 5.3: IMEP Sweep Simulation Parameters

Figure 5.2 and 5.3 shows the simulated cylinder pressure traces for both load levels. Figure 5.2 being the lowest load level of 1.6 bar, achieves a peak cylinder pressure of about 70 bar, while at 5 bar IMEP the peak pressure is over 80 bar. This increase in cylinder pressure affects the expansion stroke, by achieving a higher pressure throughout. It is easily noted that as the exhaust valves opens at $498°$, the cylinder pressure for 5 bar IMEP has a higher value, thus affecting the amplitude of the pressure wave in the exhaust manifold. Figure 5.4 shows the pressure wave action for both load levels at the same engine speed.
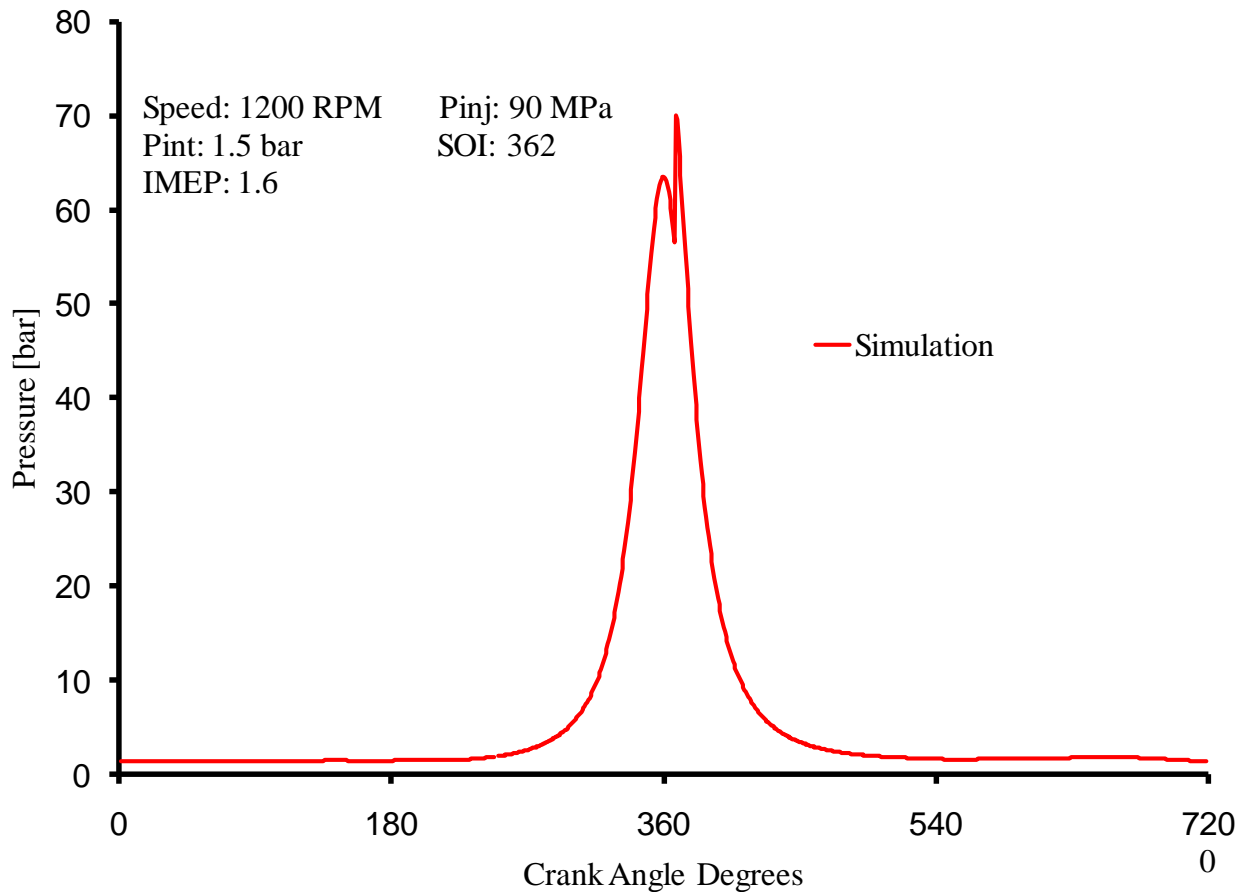


Figure 5.2: Simulated Cylinder Pressure Trace (1.6 bar IMEP)

67
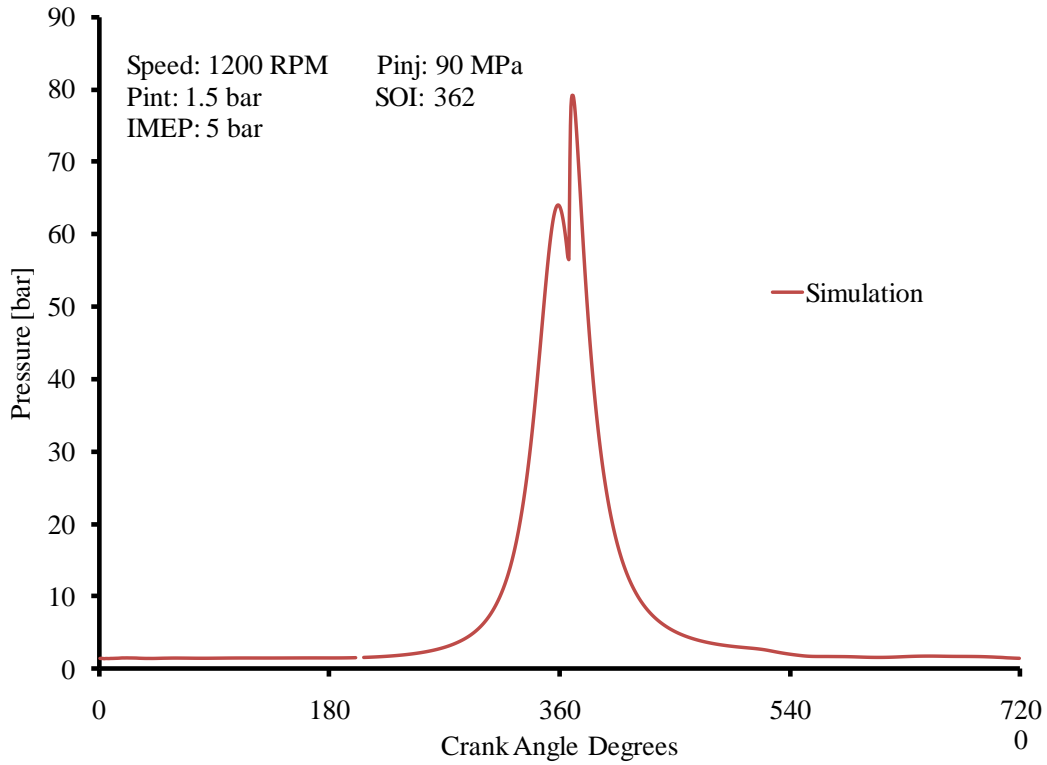
Figure 5.3: Simulated Cylinder Pressure Trace (5 bar IMEP)



Figure 5.4: Simulated IMEP Sweep

68
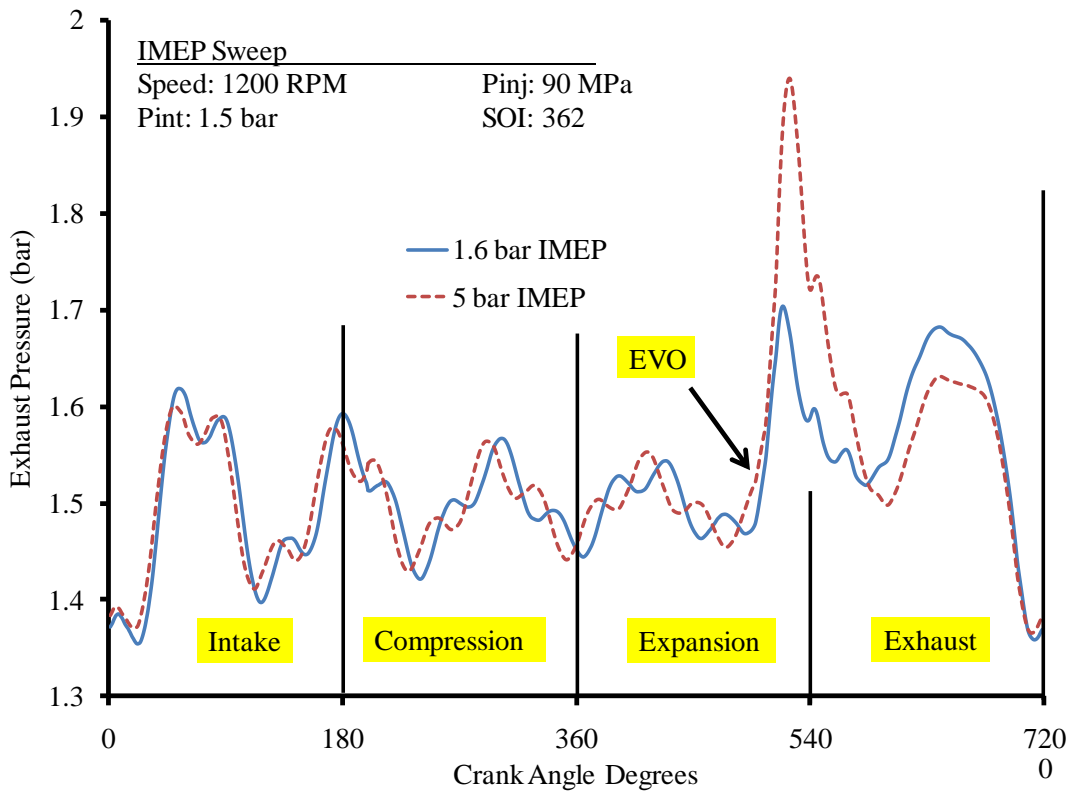
It can clearly be seen that as a higher load level is attained, the greater the pressure amplitude is, as soon as the exhaust valve opens. The interesting factor lies in the second pressure peak, after the exhaust valve opens. At low load, the second pressure peak has greater amplitude than at a higher load. For the rest of the oscillations, in the intake and compression strokes, the amplitudes remain fairly the same. There is a slight frequency change between the curves and can be noted by the pressure values at the time of time of the EVO.

### 5.1.3 Backpressure Sweep

Backpressure is used as one method to control internal exhaust gas recirculation (EGR) and exhaust noise. Backpressure effects engine performance due to poor combustion and volumetric efficiency. As backpressure is increases, a larger amount of residual gasses are kept in the cylinder, meaning less fresh air charge, hence affecting combustion. The following results show the simulated effect of two different backpressures on pressure wave action in the exhaust manifold. The engine speed, injection pressure, boost, SOI, and IMEP are kept constant as backpressure changes. The simulation parameters are shown in table 5.4.

| SIMULATION PARAMETERS | |
| --- | --- |
| Engine Speed | 1200 RPM |
| Injection Pressure | 900 bar |
| Boost | 1.5 bar |
| SOI | 364 |
| IMEP | ~1.6 bar |
| Backpressure | 1.5 bar |
| | 1.75 bar |

Table 5.4: Backpressure Sweep Simulation Parameters
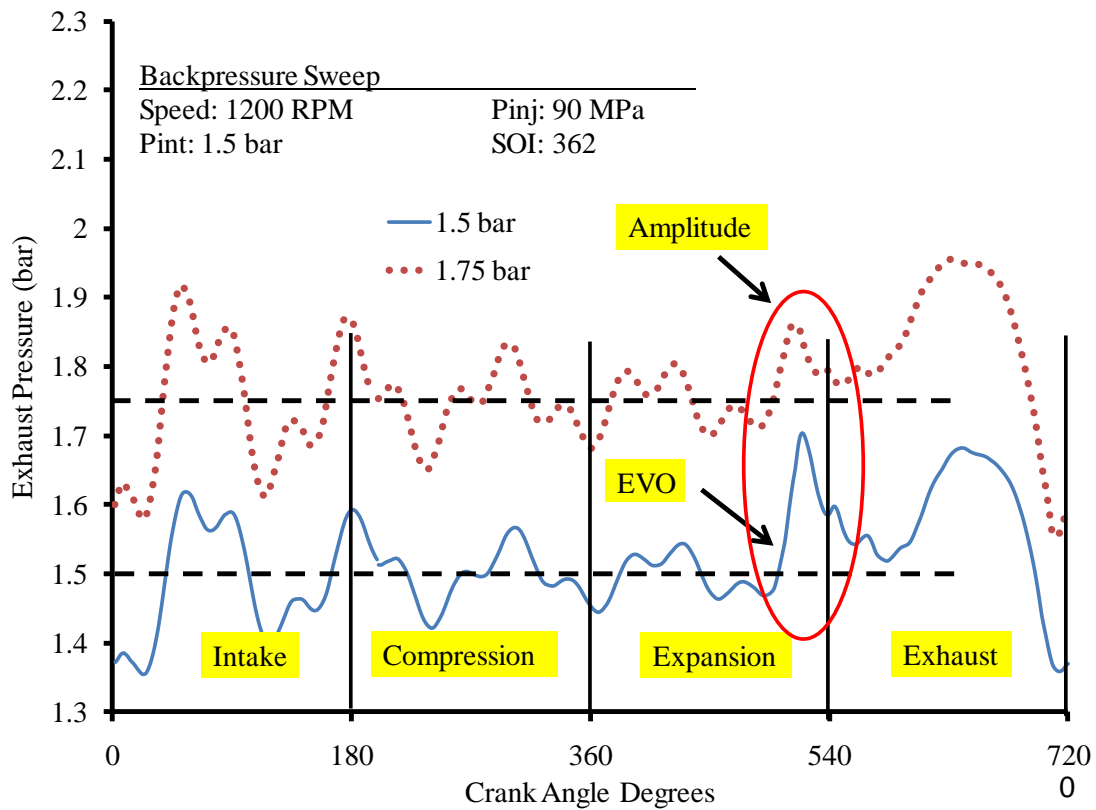


Figure 5.5: Simulated Backpressure Sweep

Figure 5.5 shows the pressure curves for both backpressure levels. As the backpressure is increased, the complete curve shifts upward, in correspondence to the backpressure level. It can be seen that both curves isolate among the stated backpressure levels. As the higher backpressure levels are reached, the amplitude on the first pressure peak, as the exhaust valve opens, reduces in magnitude. As the backpressure increases, it achieves a closer pressure to the one inside the

cylinder, therefore giving a smaller amplitude peak. The frequency and phasing of both curves remains unchanged, but there does seem to be an overall difference in the amplitude for all peaks, between the curves. When backpressure is increased the amount of fresh charge reduces and some exhaust gas gets trapped inside the cylinder. As a result, combustion suffers and the cylinder pressure trace changes. In the simulation, fueling parameters needed to be adjusted in order to keep the cylinder pressure trace the same for both cases.

### 5.1.4 Runner Length Effect

Runner length greatly affects engine performance on natural aspirated engines. The effect is highly noted on the intake side rather than the exhaust. The exhaust system is usually longer and contains more obstacles that dampen the pressure wave oscillations such as catalytic converters and mufflers. Nevertheless, oscillations occur at branch points such as bends or area changes, and these are the points of interest. The following simulation results show the effect of runner length, as it is increased and decreased from the original length of the pipe, while keeping engine speed, boost, IMEP, backpressure, SOI, and injection pressure constant. The simulation parameters are shown in Table 5.5.

| SIMULATION PARAMETERS | |
|---|---|
| Engine Speed | 1200 RPM |
| Injection Pressure | 900 bar |
| Boost | 1.5 bar |
| SOI | 364 |
| IMEP | ~1.6 bar |
| Backpressure | 1.5 bar |
| Runner Length | .5 x length |
| | 1 x length |
| | 1.5 x length |

Table 5.5: Length Sweep Simulation Parameters
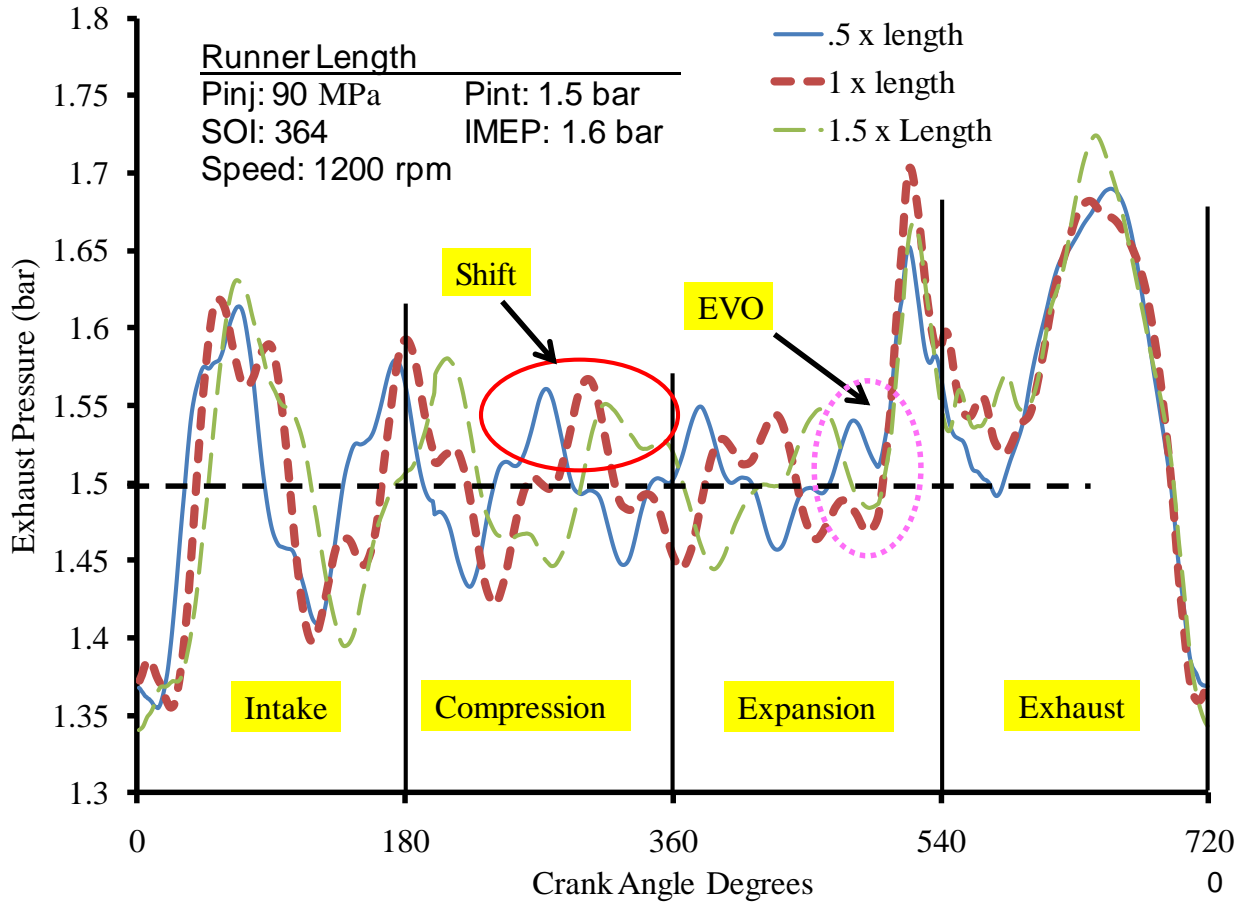
Figure 5.6: Simulated Length Sweep

Figure 5.6 shows the pressure wave curves as the length is shorten by 0.5 and lengthen by 1.5 times than the original length of the runner. As the runner length changes the amount of time for the pressure wave to travel back and forth also changes, therefore a frequency change of the pressure wave occurs. As this frequency change occurs with different runner lengths, the wave arrives at the exhaust port at different pressures. As the runner goes from the shortest to the longest, the pressure at the exhaust valve opening decreases. This low pressure valley of the pressure wave is favorable in the exhaust system because it will help draw the exhaust gasses out of the cylinder and pull more fresh charge into the cylinder. As a lower pressure arrives at the time of the EVO, due to the increase in length, the first peak after the valve opens is higher in

magnitude than the other curves. The opposite happens as the runner length is shortened, as a high pressure peak arrives at the time of the EVO.

**5.1.5 Runner Diameter Effect**

The diameter of the exhaust pipe was changed to see the effect of the pressure wave propagation. Only the pipe, where the pressure data was gathered from was changed, while the rest of the exhaust components remained the same. Three different exhaust pipe diameters were simulated under constant engine speed, injection pressure, boost, SOI, IMEP, and backpressure. The simulation parameters are shown in table 5.6.

| SIMULATION PARAMETERS | |
|---|---|
| Engine Speed | 1200 RPM |
| Injection Pressure | 900 bar |
| Boost | 1.5 bar |
| SOI | 364 |
| IMEP | ~1.6 bar |
| Backpressure | 1.5 bar |
| Pipe Diameter | 1 x length |
| | 1.25 x length |
| | 1.5 x length |

Table 5.6: Diameter Sweep Simulation Parameters
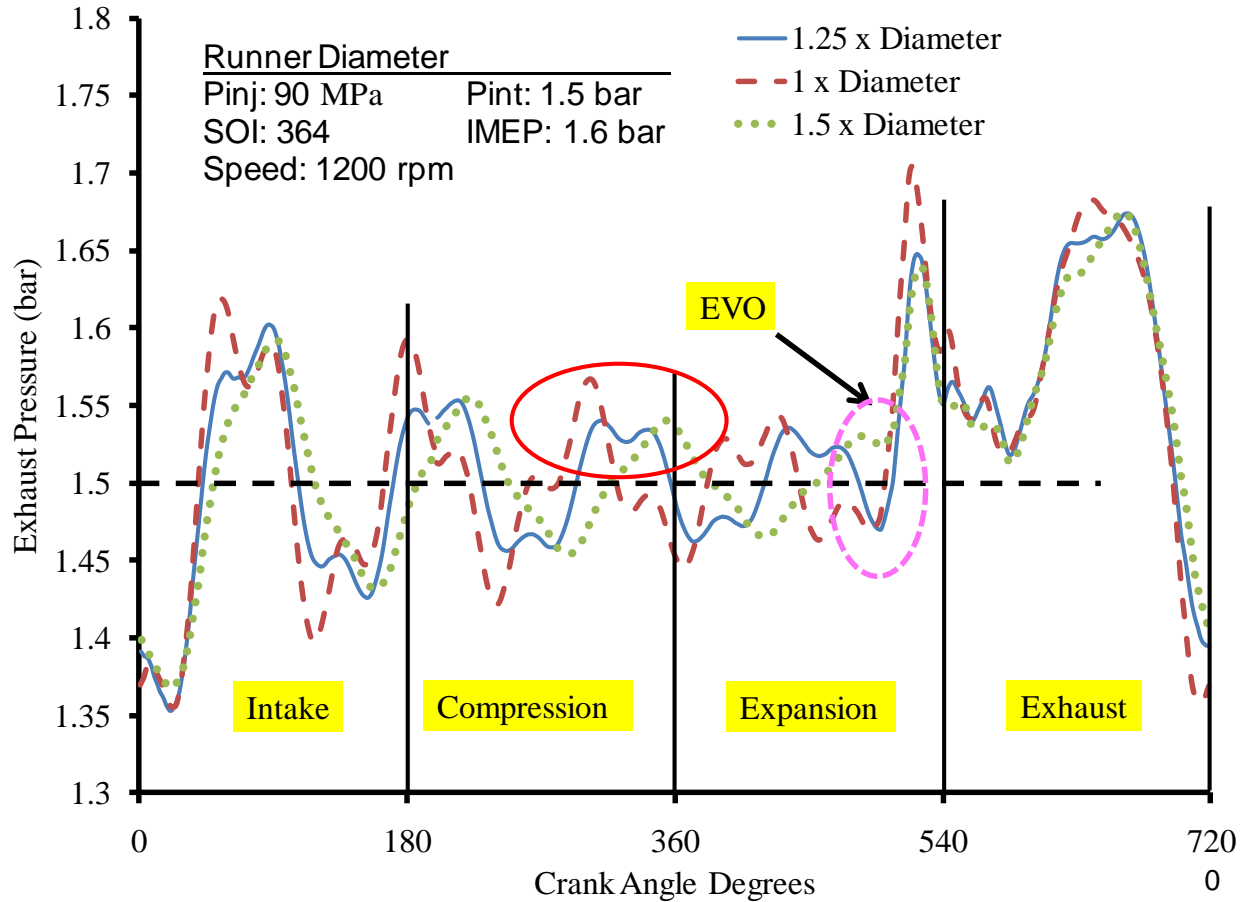
Figure 5.7: Simulated Diameter Sweep

Figure 5.7 shows the pressure wave curves for the three different exhaust pipe diameters. A similar trend is seen as the runner length effect. There is frequency difference with the change in diameter, and causes different pressure values to arrive at the time of the EVO. The smallest diameter would benefit the engine the most, as the wave arrives with a low pressure valley at the time of the exhaust valve opening, helping with the gas exchange process. The same is not true as the diameter increases.

**5.1.6 Position Effect**

Since SCR distribution occurs downstream of the exhaust system, it is necessary to study the pressure wave effects at locations farther down the exhaust system. In the simulation,

components such as catalysts, mufflers, or filters are not implemented into the model. These components will significantly affect the pressure wave action by dampening the wave to higher degree, but nonetheless the simulation will give an idea of the trends that are seen downstream of the exhaust system. The pressure measurement is taken at the middle of duct 8 shown in Figure 4.26. The simulation consists of comparing the pressure wave action at duct 8 with duct 2 for one engine operating mode. The simulation parameters are shown in Table 5.7.

| SIMULATION PARAMETERS | |
|---|---|
| Engine Speed | 1200 RPM |
| Injection Pressure | 900 bar |
| Boost | 1.5 bar |
| SOI | 364 |
| IMEP | ~1.6 bar |
| Backpressure | 1.5 bar |

Table 5.7: Location Simulation Parameters
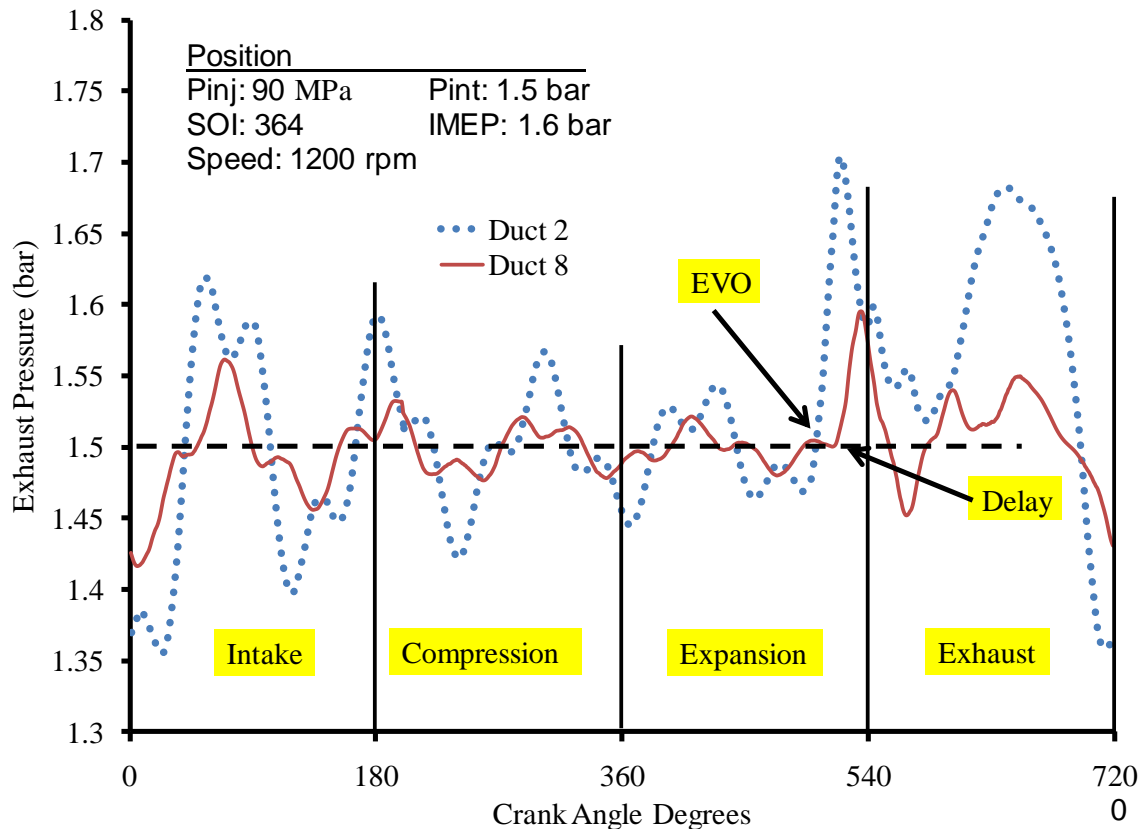


Figure 5.8: Position Simulation

75

Figure 5.8 shows the pressure wave effect at two different locations in the exhaust system. Duct 2, located next to the exhaust port, receives the first pressure pulse after EVO, and $13^o$ later, duct 8 receives it, but with a much weaker amplitude. The distance from the two pressure locations is just over one meter. In vehicle exhaust systems, especially in those of diesel engine trucks, the exhaust systems are much longer than a meter, therefore the magnitude of the pressure wave would be much weaker but there would still be some pressure oscillation.

## 5.2 Empirical Results

Most of the following research results were conducted on the Ford Puma research engine, with the exception of test five which was conducted on the single cylinder research engine. The results show pressure wave actions in the exhaust manifold, as stated before. The effect of engine speed, load, exhaust gas recirculation, backpressure, and post injection are shown. Table 5.8 shows the test matrix.

| TEST | TYPE | IMEP (bar) | RPM | | |
|------|------|------------|------|------|------|
| 1 | RPM Sweep | 5 | 1200 | 1500 | 1800 |
| 2 | IMEP Sweep | 2-7 | 1200 | 1500 | 1800 |
| 3 | EGR Sweep | 3 | 1800 | | |
| 4 | Back Pressure Effect | 3 | 1800 | | |
| 5 | Post-Injection | 5 | 1200 | | |

Table 5.8: Empirical Test Matrix

## 5.2.1 RPM Sweep (Test #1)

The effects of different engine speeds are tested to see the effect on the pressure wave in the exhaust manifold. Three different engine speeds are attained while keeping injection pressure, boost, IMEP, and backpressure constant. The start of injection (SOI) changes as engine speed

changes in order to accommodate combustion and keep the same load level. The testing

parameters are shown in Table 5.9.

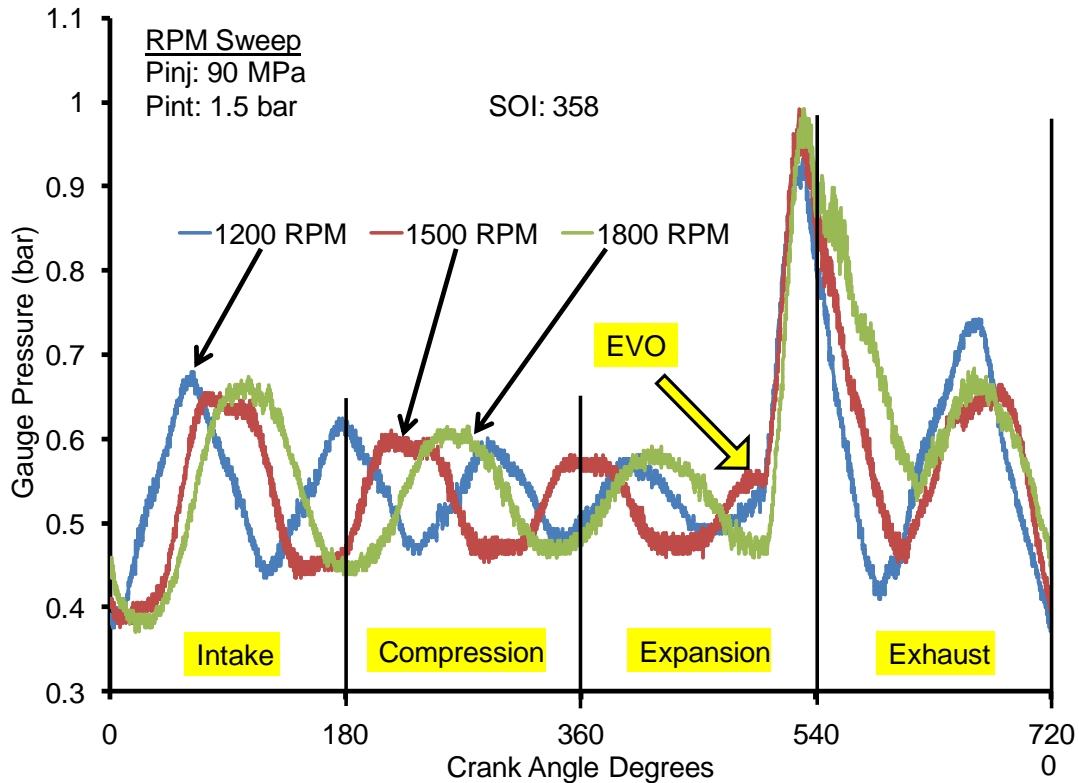| TEST #1 PARAMETERS | |
|---|---|
| Engine Speed | 1200 RPM |
| | 1500 RPM |
| | 1800 RPM |
| Injection Pressure | 900 bar |
| Boost | 1.5 bar |
| SOI | 364 to 357 |
| IMEP | ~1.6 bar |
| Backpressure | 1 bar |

Table 5.9: Empirical Test #1 Parameters



Figure 5.9: Empirical RPM Sweep

During testing the backpressure, boost, start of ignition (SOI), and ignition duration were kept

constant. The first aspect to note is the exhaust valve opening, which can clearly seen by each

rpm curve by the sudden increase in pressure in Figure 5.9. The exhaust valve opening occurs at

around 500 degrees. The first peak pressure seems to vary little as engine speed increases. The increase in peak pressure from 1200 rpm to 1800 rpm is only 1.2 psi. The interesting event occurs in the second pressure peak, in which the lower engine speed of 1200 rpm attains a higher peak pressure than the higher engine speeds and is seen throughout the rest of the oscillations. Also, notice the phase difference as engine speed increases due to the speed at which the exhaust gasses are pushed out of the cylinder. During the compression stroke, the shift change between each engine speed curve is about $44^o$, and a total shift change of about $88^o$ as engine speed increase from 1200 rpm to 1800 rpm. Due to this frequency and phase shift as engine speed increases, the wave arrives at different pressure points when the exhaust valve opens for the next cycle. At 1200 rpm the wave arrives at the exhaust valve with increasing pressure, also known as a compression wave. At 1500 rpm the wave arrives at the peak of the compression wave, which would aid in internal exhaust gas recirculation (EGR) but would affect engine performance. At an engine speed of 1800 rpm, the bottom peak of the expansion wave arrives at the exhaust port, helping draw the exhaust out of the cylinder faster, and introducing more fresh charge. A low pressure point when the exhaust valve opens is desirable for performance, and a high pressure point is desirable from an emission point of view.

**5.2.2 IMEP Sweep (Test #2)**

Six different load conditions are tested to study the effect of pressure wave action in the exhaust manifold, at three different engine speeds while keeping injection pressure, boost, backpressure, and start of injection constant. As a greater fuel amount is injected the load level changes. For each set of load tests, the engine speed is kept the same. Therefore, the start of injection does not change during the load sweep. The testing parameters for the first load sweep are shown in Table 5.10.

**5.2.2.1 Test #2a (1200 RPM)**

| TEST #2A PARAMETERS | |
|---|---|
| Engine Speed | 1200 RPM |
| Injection Pressure | 800 bar |
| Boost | 1.5 bar |
| SOI | 364 |
| IMEP | 1.6 bar |
| | 2.64 bar |
| | 4.05 bar |
| | 5 bar |
| | 6.03 bar |
| | 6.85 bar |
| Backpressure | 1.5 bar |

Table 5.10: Empirical Test #2a Parameters
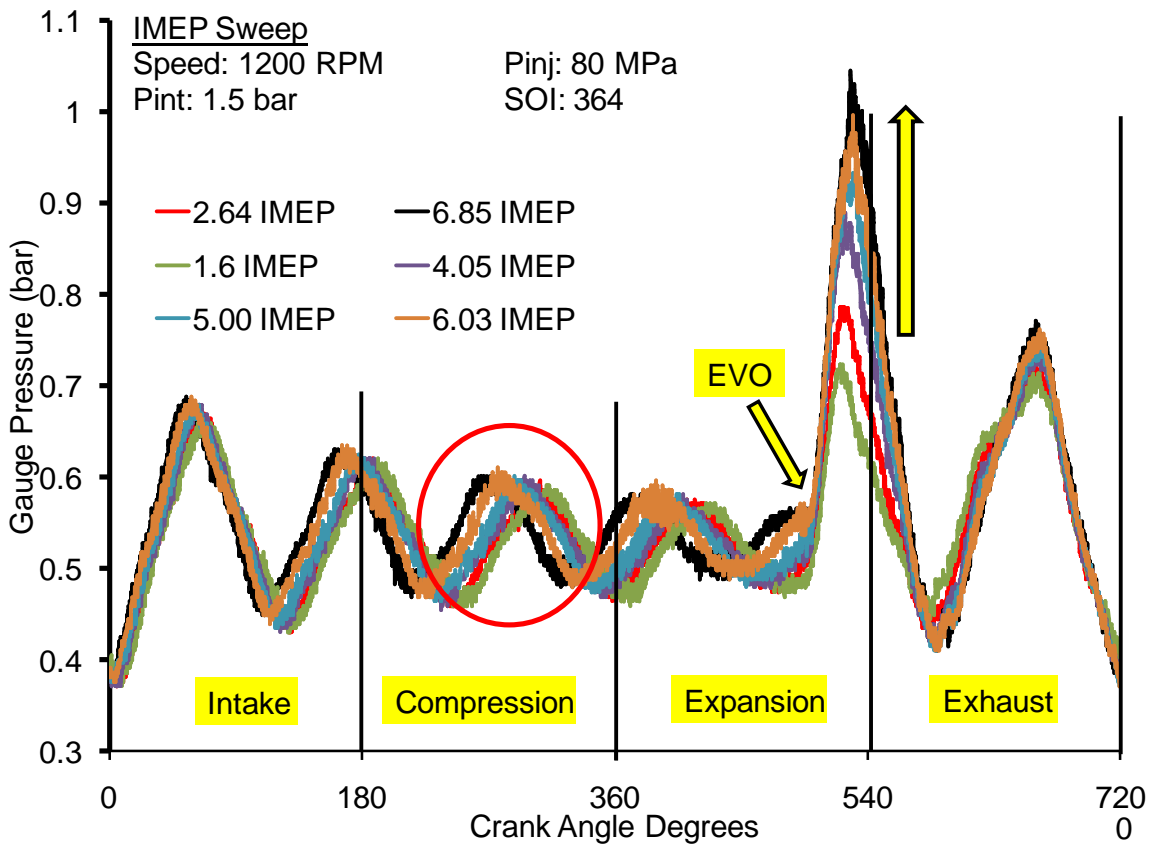


Figure 5.10: Empirical IMEP Sweep (1200 RPM)
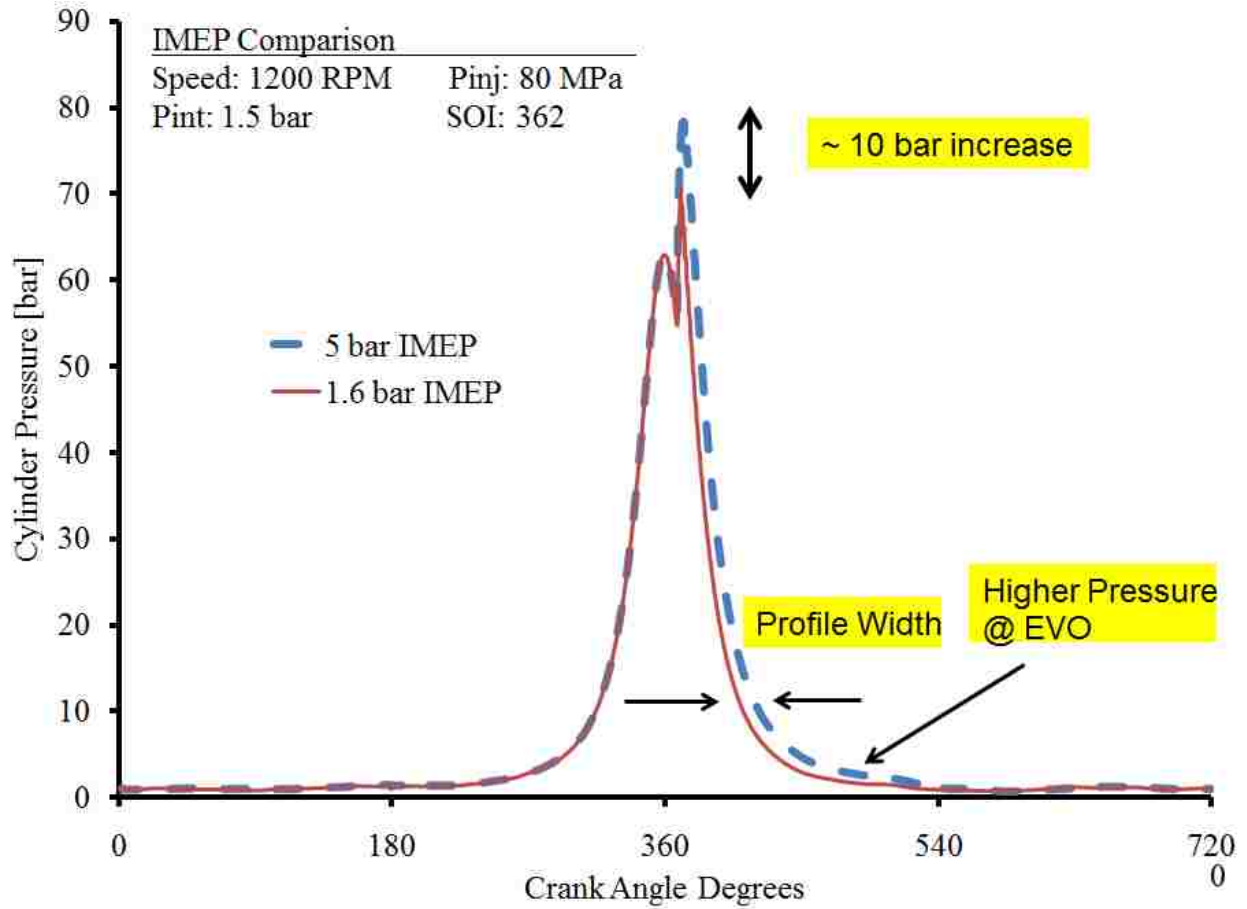
Figure 5.11: Empirical Cylinder Pressure Trace Comparison

### 5.2.2.2 Test #2b (1500 RPM)

| TEST #2B PARAMETERS | |
|---|---|
| Engine Speed | 1500 RPM |
| Injection Pressure | 900 bar |
| Boost | 1.5 bar |
| SOI | 360 |
| IMEP | 1.7 bar |
| | 2.87 bar |
| | 4 bar |
| | 5 bar |
| | 6 bar |
| | 7 bar |
| Backpressure | 1.5 bar |

Table 5.11: Empirical Test #2b Parameters
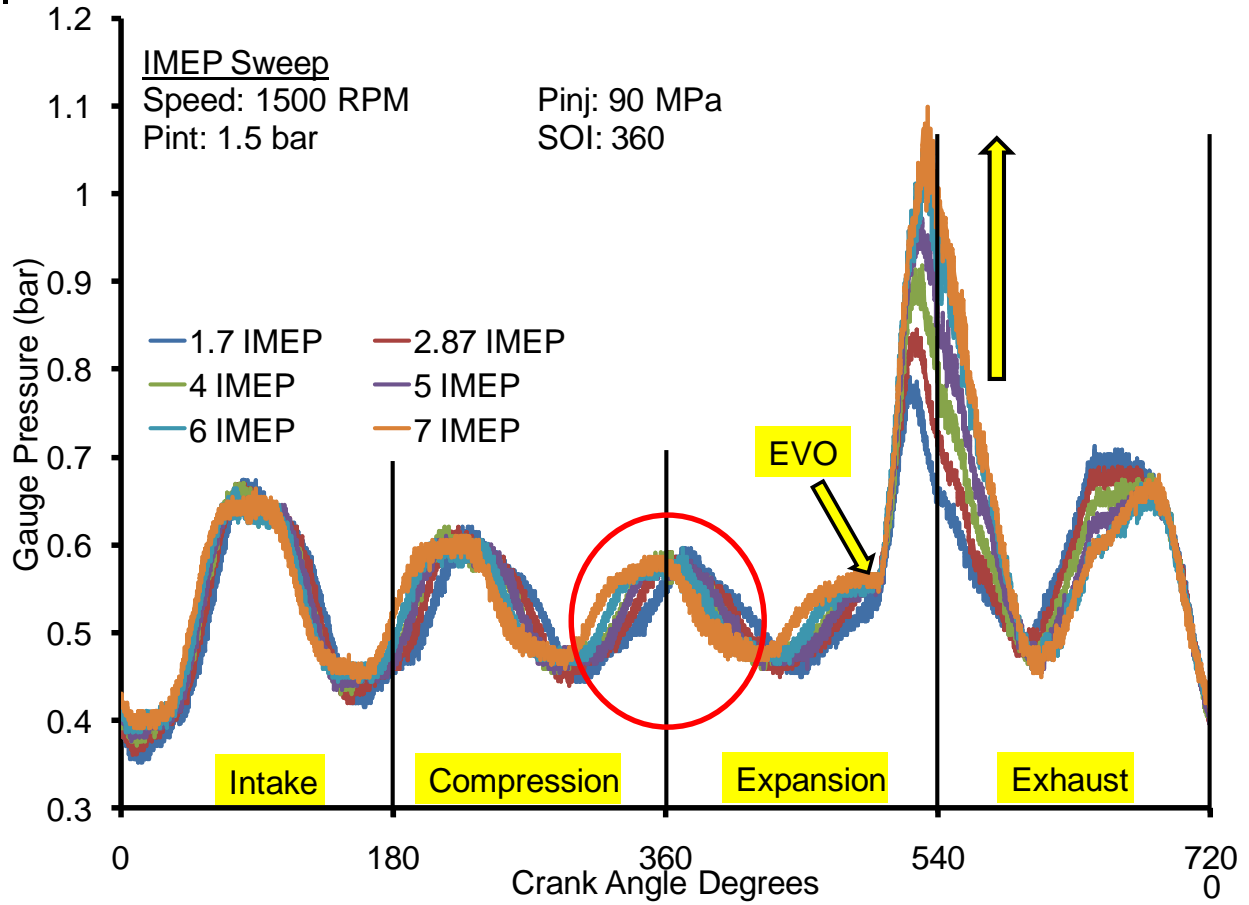
Figure 5.12: Empirical IMEP Sweep (1500 RPM)

### 5.2.2.3 Test #2c (1800 RPM)

| TEST #2C PARAMETERS | |
|---|---|
| Engine Speed | 1200 RPM |
| Injection Pressure | 900 bar |
| Boost | 1.5 bar |
| SOI | 357 |
| IMEP | 1.6 bar |
| | 3.06 bar |
| | 3.97 bar |
| | 5 bar |
| | 6 bar |
| | 7 bar |
| Backpressure | 1.5 bar |

Table 5.12: Empirical Test #2c Parameters
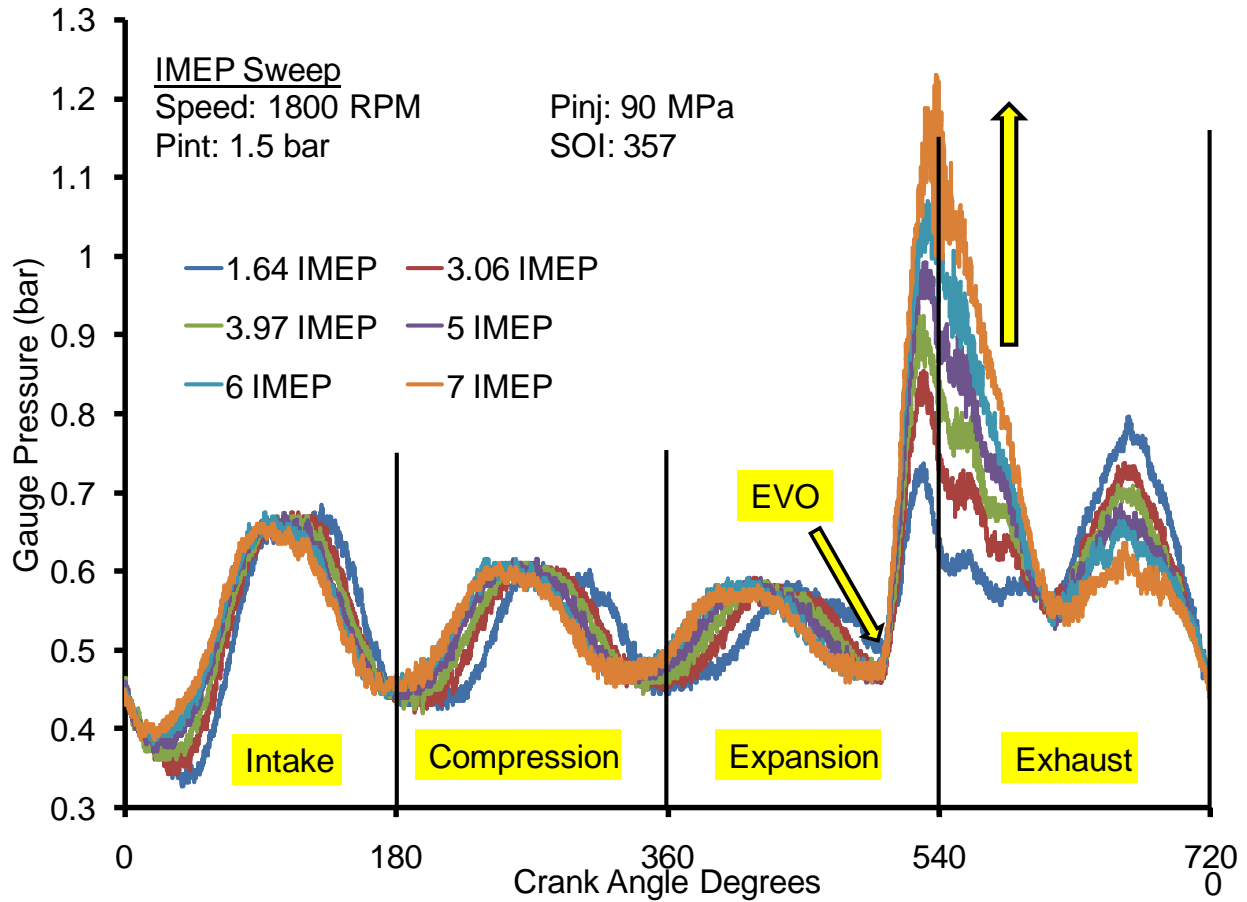
Figure 5.13: Empirical IMEP Sweep (1800 RPM)

In all three sets of tests, at different engine speeds, the exhaust valve opening event can clearly be observed by the sudden increase in pressure, which occurs around 500 degrees. In every case the amplitude of the first pressure peak after the exhaust valve opens, increases as load is increased. As the IMEP levels increases, the amount of fuel injected increases, raising cylinder pressures and temperatures, seen in figures 5.11. The compression profile in figure 5.11, remains the same as the load level increases, but the combustion profile changes considerably. An increase of 10 bar, in peak cylinder pressure is seen, as load level increases from 1.6 bar to 5 bar IMEP. Due to the change in the combustion profile, the expansion profile changes accordingly with relative higher cylinder pressures. At the moment of the exhaust valve opening, the cylinder

pressure is at a higher state, therefore yields a higher peak pressure in the exhaust manifold. Also a frequency change occurs, but it is not as apparent as the previous rpm sweep test. In figure 5.10, at an IMEP of 1.64 bar, the secondary pressure peak is higher than the first pressure peak. The same trend is observed in figures 5.12 and 5.13, where the lower engine speeds and load levels causes a higher secondary pressure peak, than at higher speeds and loads.

### 5.2.3 EGR Sweep (Test #3)

An EGR sweep was conducted since it is a commonly used technique to effectively reduce NOx emissions, but at the expense of combustion efficiency. As explained in the introduction, EGR effectively reduces NOx, by reducing the flame temperature and availability of oxygen. At higher EGR levels or lower oxygen concentrations a mode of combustion known as low temperature combustion (LTC) can be reached. Since this mode of combustion is the primary research for many, it is important to understand its full effects on pressure wave propagation. Five different levels of EGR are implemented, to see the effects on pressure wave action in the exhaust manifold. This change in specific heat capacity ratio affects wave propagation speed. The test consisted of a constant engine speed, injection pressure, boost, start of injection, and backpressure. As EGR was introduced into the cylinder, by manipulating both the EGR and backpressure valve, the IMEP levels do not drop significantly. The testing parameters are shown in Table 5.13.

| TEST #3 PARAMETERS | |
|---|---|
| Engine Speed | 1800 RPM |
| Injection Pressure | 900 bar |
| Boost | 1.5 bar |
| SOI | 358 |
| IMEP | 3 bar |
| Backpressure | 1.5 bar |
| EGR % | 0 |
| | 23 |
| | 45.5 |
| | 66 |
| | 72.1 |

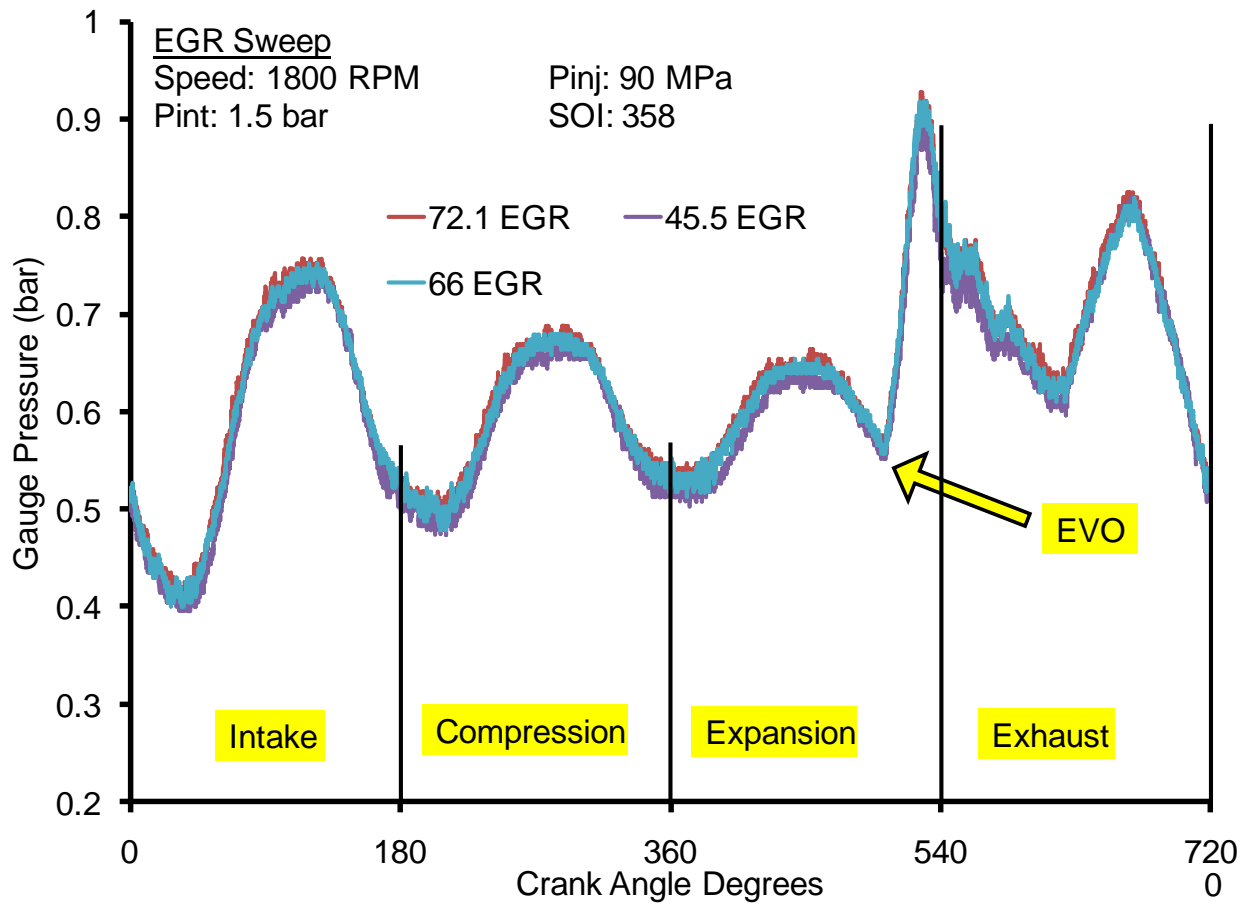Table 5.13: Empirical Test #3 Parameters



Figure 5.14: Empirical EGR Sweep

Figure 5.14 shows three curves which are imposed on each other are at different levels of EGR. There seems to be no clear difference in pressure magnitude nor phase shift as the EGR levels increase, concluding that the specific heat ratio has little to no impact on the wave propagation characteristics.

**5.2.4 Back Pressure Effect (Test #4)**

As stated above, one of the techniques in controlling the amount of EGR is to manipulate the amount of backpressure. Two different backpressures are tested, and the effects seen on pressure wave actions in the exhaust manifold. As the amount of backpressure is increased, the EGR valve is kept closed to keep combustion constant. In this test, while increasing the amount of backpressure pressure, engine speed, injection pressure, SOI, boost, and IMEP are all kept constant. The testing parameters are shown in Table 5.14.

| TEST #4 PARAMETERS | |
|---|---|
| Engine Speed | 1800 RPM |
| Injection Pressure | 900 bar |
| Boost | 1.5 bar |
| SOI | 358 |
| IMEP | 3 bar |
| Backpressure | 1.5 bar |
| | 1.7 bar |

Table 5.14: Empirical Test #4 Parameters
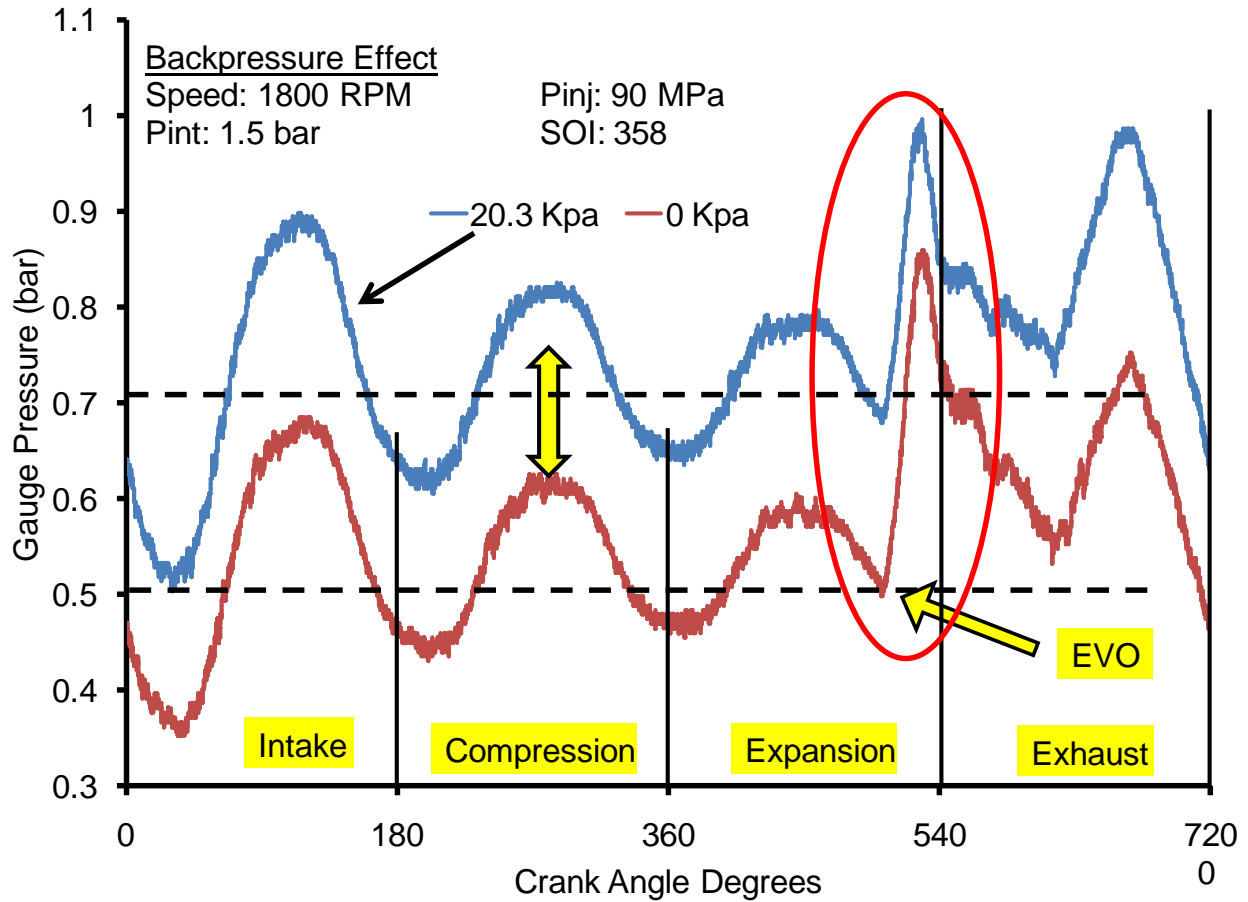
Figure 5.15: Empirical Backpressure Sweep

Figure 5.15 shows the pressure wave effect on two different backpressures. As the backpressure is increased the pressure profile increases accordingly to the given backpressure value. Both pressure curves oscillate among the static backpressure condition shown by the black dotted line. The frequency and phasing of both curves remain the same except for their amplitudes. As backpressure increases, the pressure difference between the exhaust manifold and the cylinder decrease, therefore the first pressure peak as the exhaust valve opens, shortens in amplitude. The rest of the amplitudes in the intake, compression, and part of the exhaust stroke have similar magnitudes.

## 5.2.5 Post-Injection Effect (Test #5)

Post-injection involves a secondary fuel injection, during the expansion stroke to raise cylinder temperature. It is a technique used for regeneration of diesel particulate filter (DPF), to burn off the particulate matter (PM) trapped in the DPF. The test consists of a constant main injection, and varying the post injection timing. Seven post-injection timings are implemented, and the effects on pressure wave actions in the exhaust manifolds observed. The test is conducted with constant engine speed, injection pressure, boost, main injection timing, initial IMEP, and backpressure. The testing parameters are shown in Table 5.15.

| TEST #5 PARAMETERS | |
|---|---|
| Engine Speed | 1200 RPM |
| Injection Pressure | 1200 bar |
| Boost | 1.25 bar |
| SOI | 360 |
| IMEP | 5 bar |
| Backpressure | 1.3 bar |
| Post-Injection Timing | 380 |
| | 385 |
| | 390 |
| | 400 |
| | 410 |
| | 415 |
| | 420 |

Table 5.15: Empirical Test #5 Parameters

| POST-INJECTION LEGEND | |
|---|---|
| | Injection Timing (Degrees) |
| | 0 |
| | 0 |
| | 390 |
| | 380 |
| | 400 |
| | 410 |
| | 415 |
| | 420 |

Table 5.16: Empirical Test #5 Legend
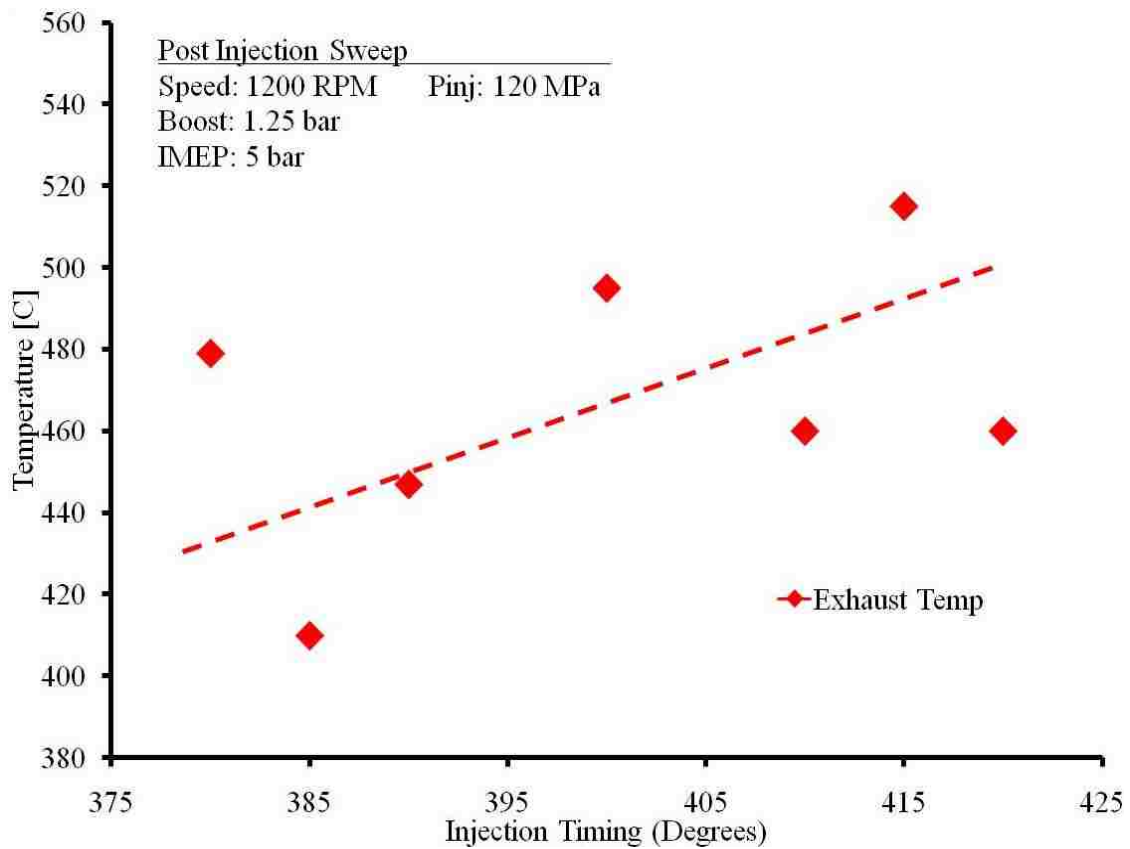


Figure 5.16: Empirical Post-Injection Exhaust Temperature
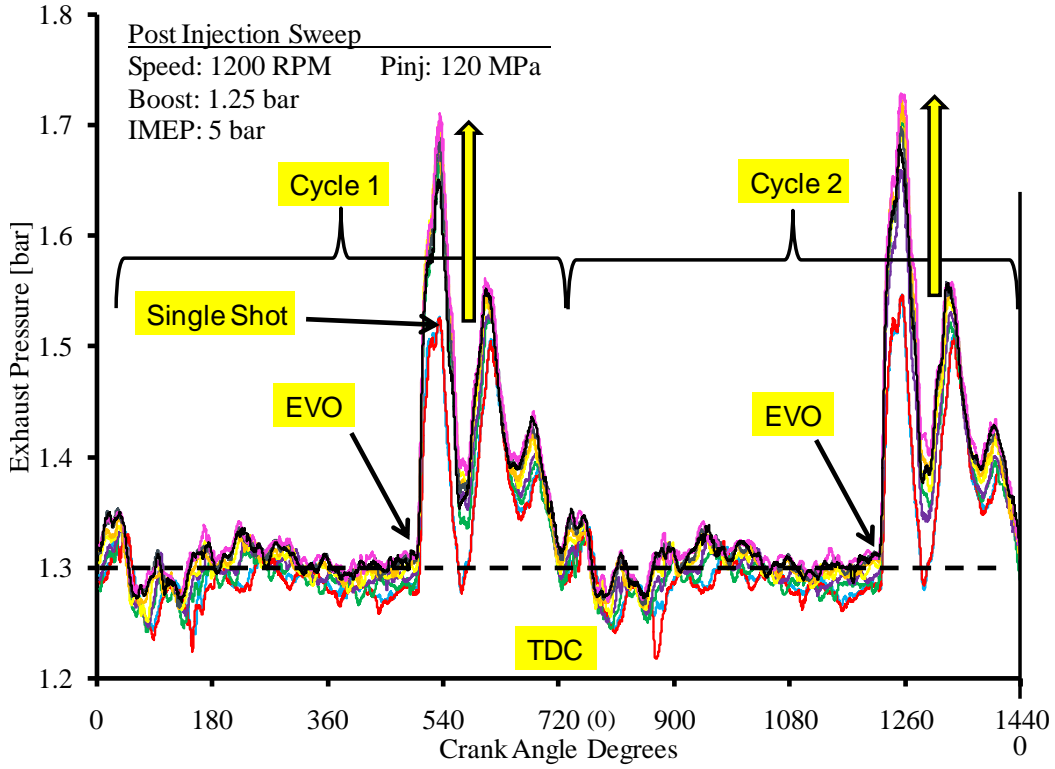
Figure 5.17: Empirical Post-Injection Sweep (2 Cycles)
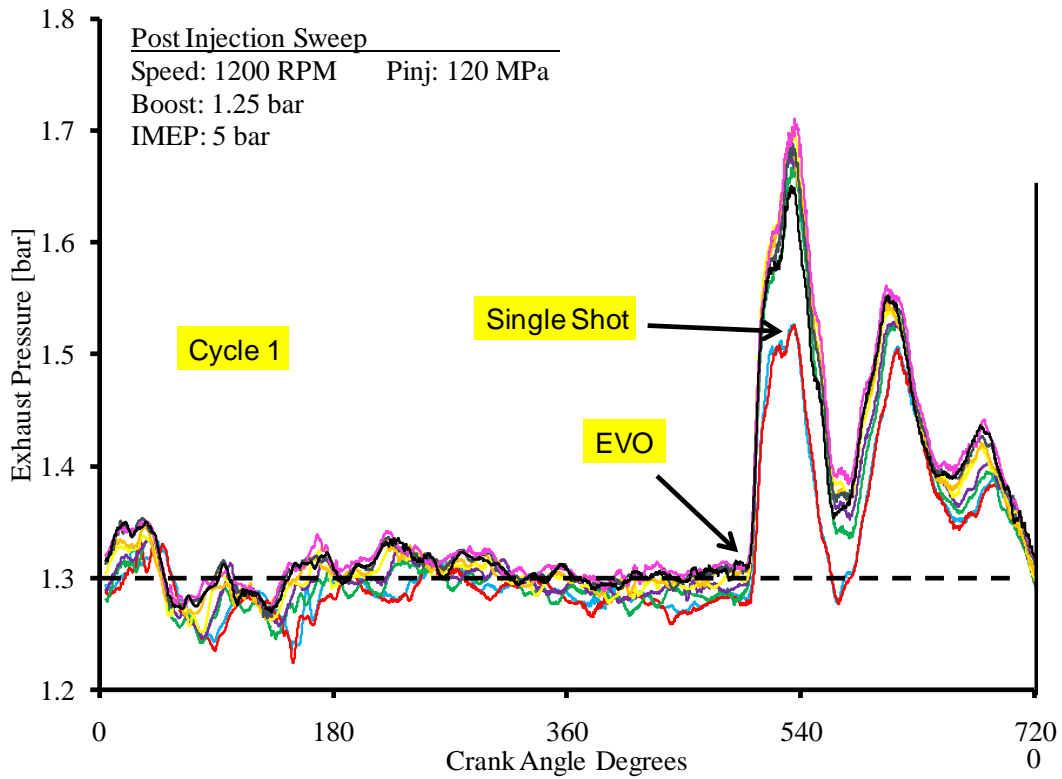


Figure 5.18: Empirical Post-Injection Sweep (1$^{st}$ Cycle)

89
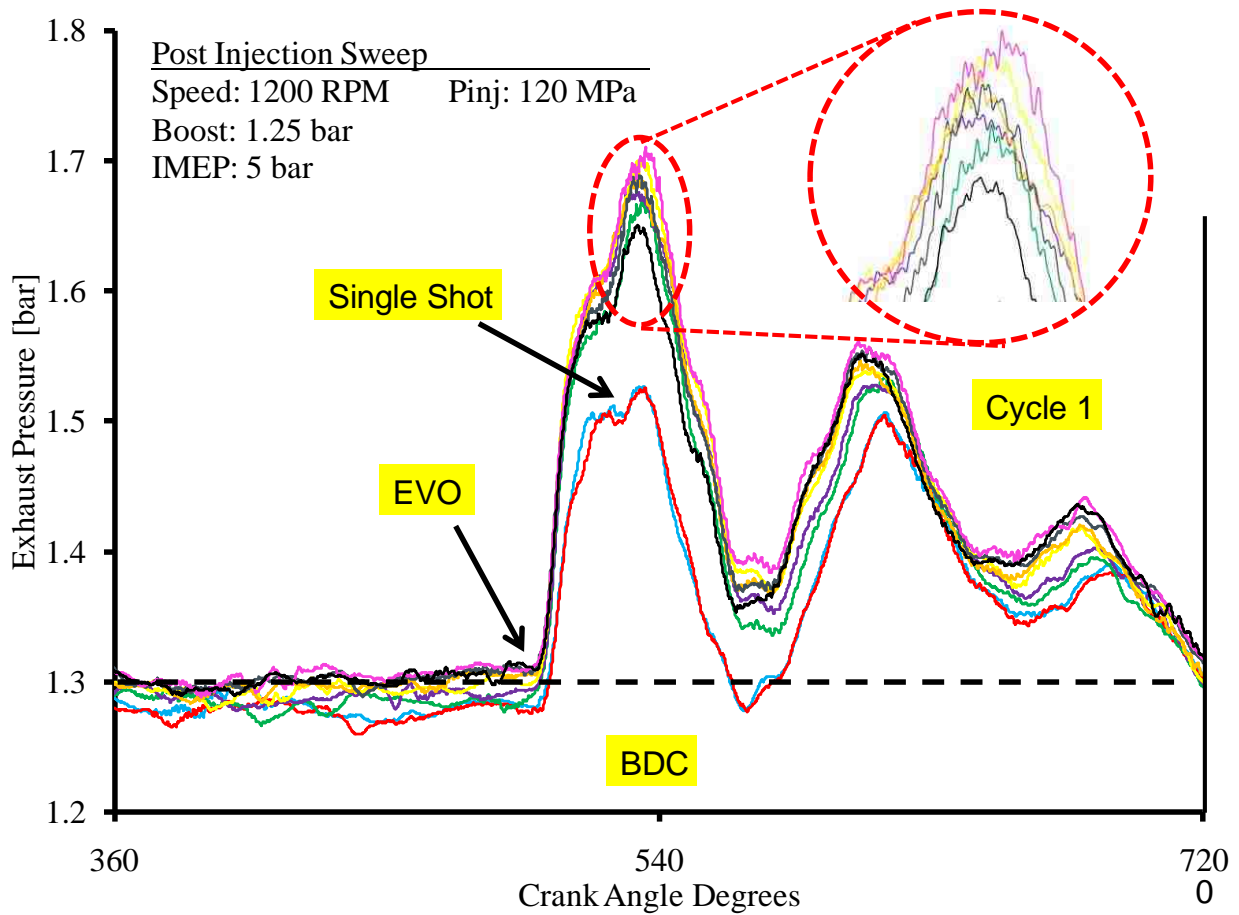
Figure 5.19: Empirical Post-Injection Sweep Amplitude (1$^{st}$ Cycle)

Figure 5.16 shows the exhaust temperature next to the pressure transducer, as the post injection is retarded. As the post injection time is retarded the overall average exhaust temperature increases. The temperature data was recorded after a few hundred cycles ran to reach steady state conditions. Figure 5.17 shows two cycles of the pressure wave curves for the post-injection sweep. Two curves indicated by the single injection tab in Figure 5.17, represent the base curve before a second injection was implemented. As the post-injections were implemented, a higher exhaust pressure occurred, due to the pressure increase inside the cylinder. The two cycles are shown, in order to see the pressure wave oscillations throughout the next cycle. As the pressure

waves travel back and forth in the exhaust system, after the exhaust valve opening, the amplitudes dampen due to friction and heat transfer losses. In figure 5.18, the first cycle is isolated to show the frequency change as the post-injection is retarded. A frequency change is not certain since there is still some noise associated with the data even after filtering. Figure 5.19 shows the amplitudes as soon as the EVO, for the post-injection curves. The trend seems to be, that as a higher exhaust temperature is reached, which may not necessarily correspond to a later post-injection, the higher the amplitude. Again, it is a trend that can be observed, but more tests need to be conducted to validate the previous trends.

## 5.3 Comparison

In this section both the empirical and simulation results are compared to validate the simulation model.

### 5.3.1 Cylinder Pressure Trace

During the empirical test, various load levels were conducted at different engine speeds, however, in the simulation model, only two load levels were simulated. As stated before, the empirical heat release data for each load level had to be implemented into the model, and a certain degree of calibration had to be conducted, for the cylinder pressure traces to match. Figure 5.20 and 5.21, show the empirical and simulated cylinder pressure traces for both load levels.
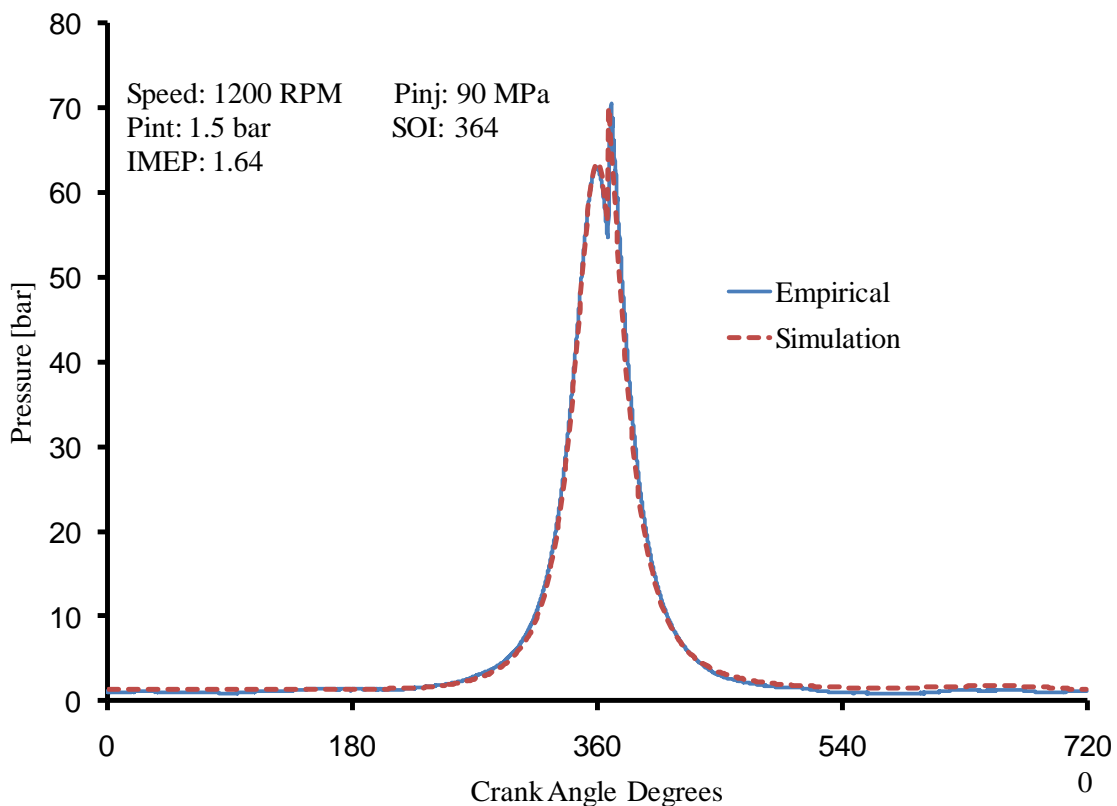


Figure 5.20: Cylinder Pressure Trace Comparison (1.64 bar IMEP)
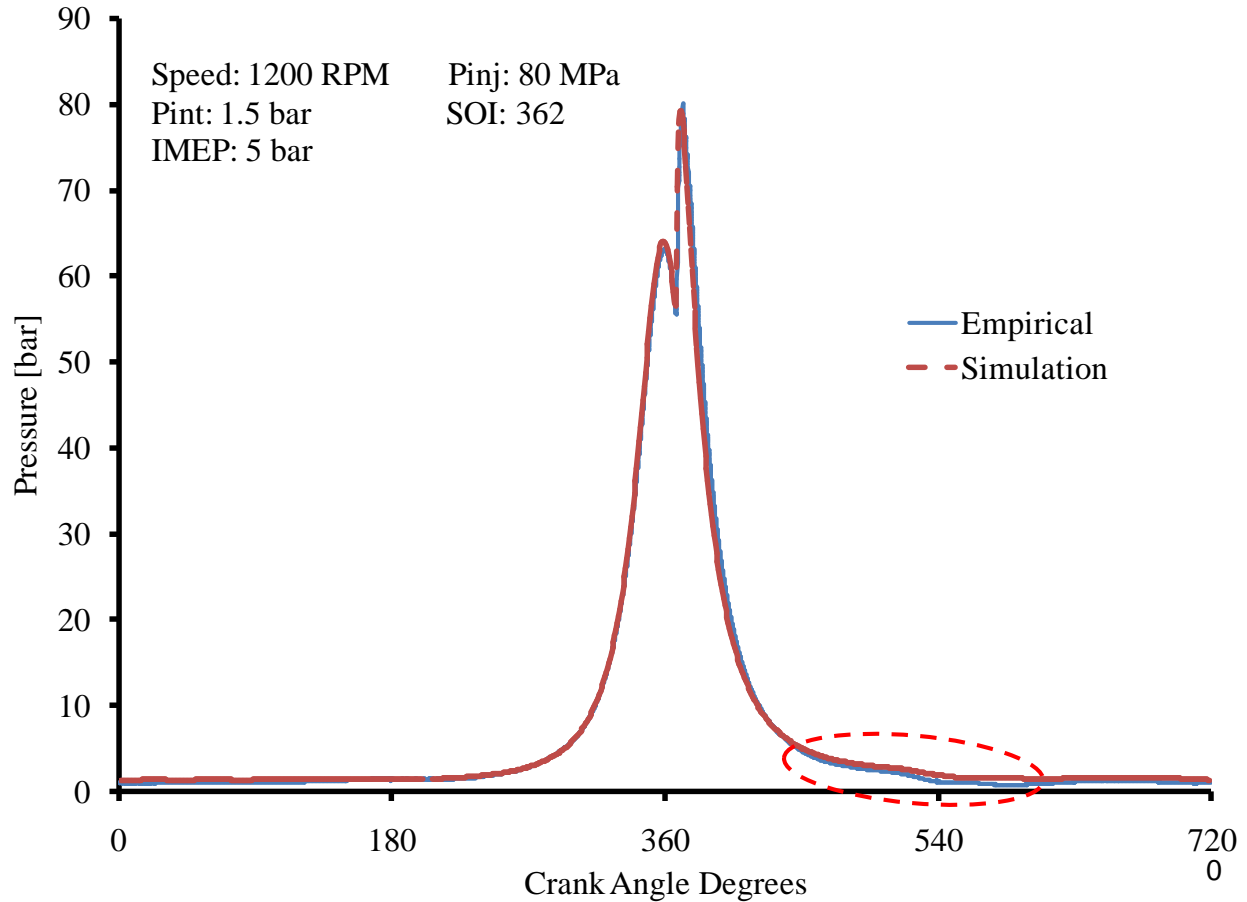
Figure 5.21: Cylinder Pressure Trace Comparison (5 bar IMEP)

Figure 5.20 shows the cylinder pressure traces for 1.64 bar IMEP. The simulation curve follows the empirical curve accurately, from compression to expansion. The combustion profile, including the start of combustion and peak cylinder pressure, matches accurately as well. During the expansion stroke, the simulation accurately follows the empirical up until the end, where there is slight variation past $540^{o}$ . In the same way, the simulated cylinder pressure curve in figure 5.21, which represents a load level of 5 bar IMEP, accurately follows the empirical cylinder pressure trace up until the expansion. The red dotted circle shows the variation between both curves. This variation exceeds the one seen in Figure 5.21. At the time of the exhaust valve opening, the simulated data has a higher pressure, therefore affecting the pressure wave

amplitude. As stated in the simulation set up, there are certain scaling parameters that can be further adjusted, to give a more accurate simulated cylinder pressure trace.

### 5.3.2 Model Validation

Figures 5.22, 5.23, 5.24, show both the empirical and simulated pressure wave traces, at different engines speeds, and a constant load level of 5 bar IMEP.
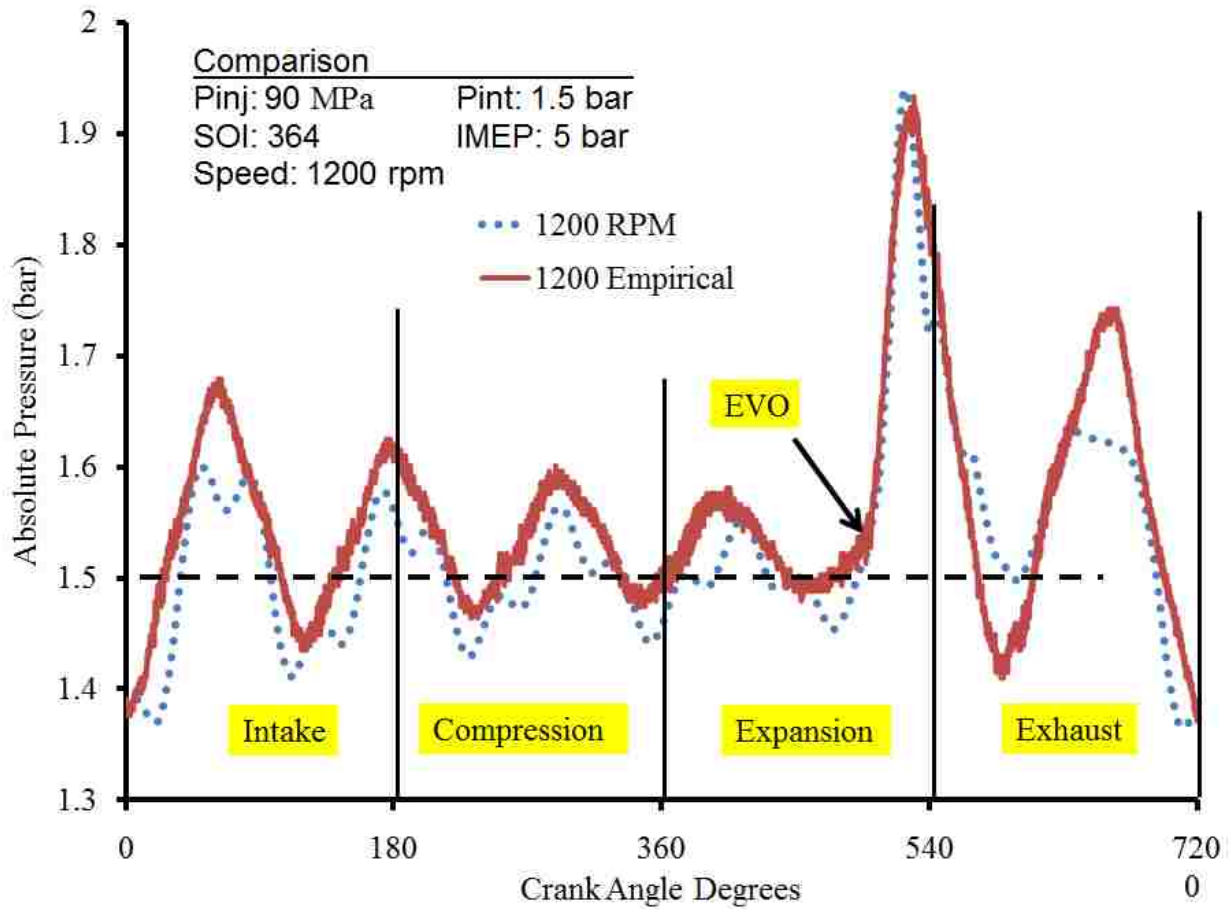
Figure 5.22: 1200 RPM Comparison
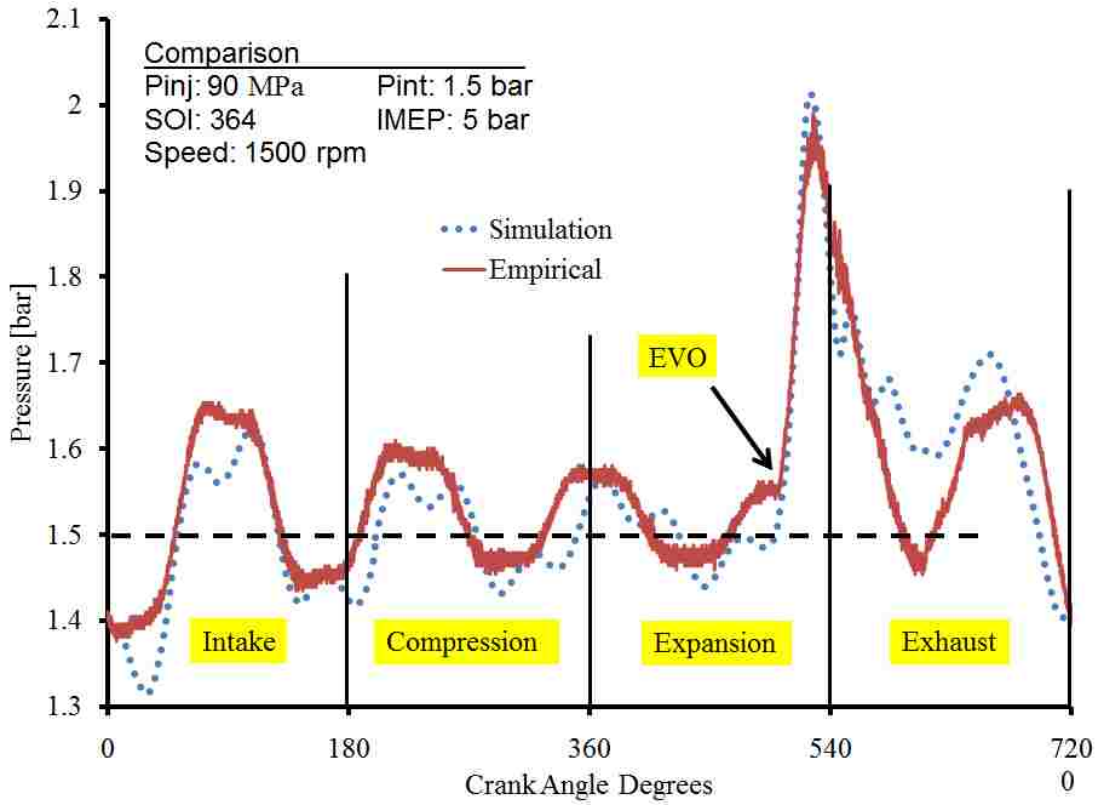
Figure 5.23: 1500 RPM Comparison
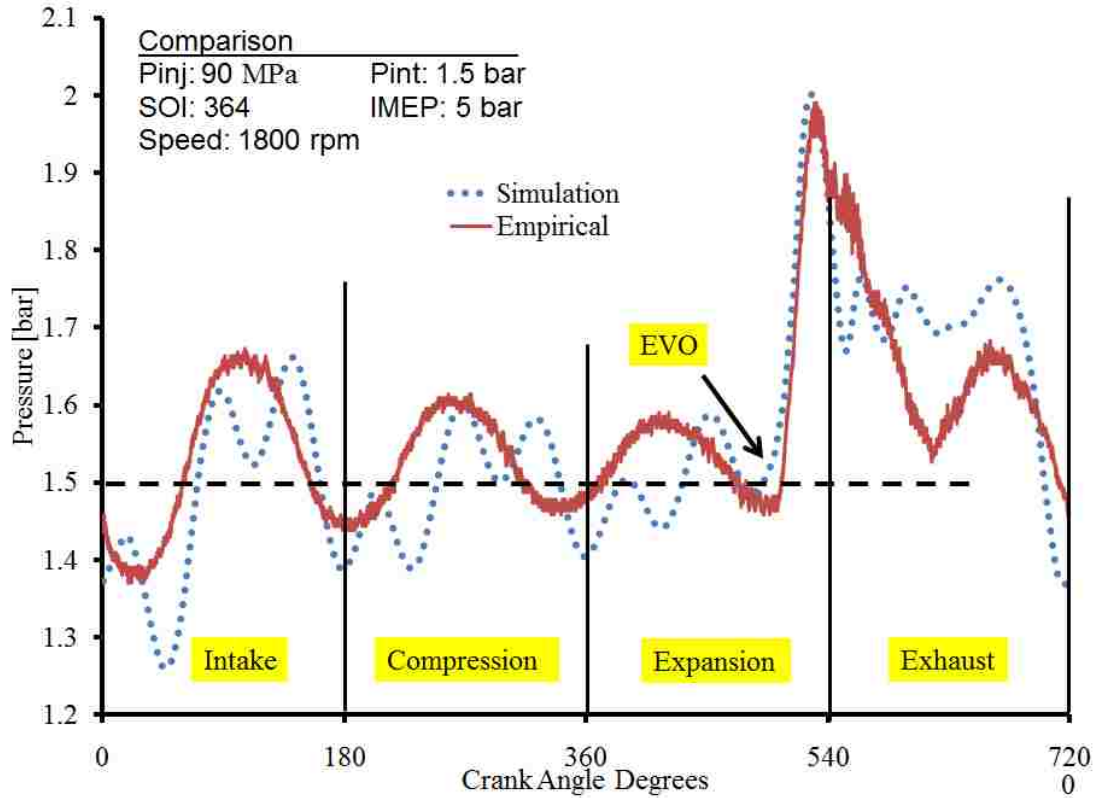


Figure 5.24: 1800 RPM Comparison

95

The simulated results for the first two comparison figures, showing 1200 rpm and 1500 rpm, have strong similarities in amplitude, phasing, and frequency. The third curve showing an engine speed of 1800 rpm, does not have the same similarity strength as the first two comparison curves. The phasing in the simulated curve for 1800 rpm differs to the empirical, except for the amplitude of the wave oscillations. The difference may lie in unknown parameters, such as heat transfer coefficients, and friction of the junctions and pipes. A better match can be attained by calibrating the model by trial and error, with different values. In all three curve comparisons, the trends are similar, and can be concluded, that the simulation model is valid. In addition, Figure 5.25 shows the comparison of the empirical to the simulated conditions at a lower load level, of 1.6 bar IMEP. The simulation curve, again follows the empirical work closely, therefore enforcing the validation of the model.
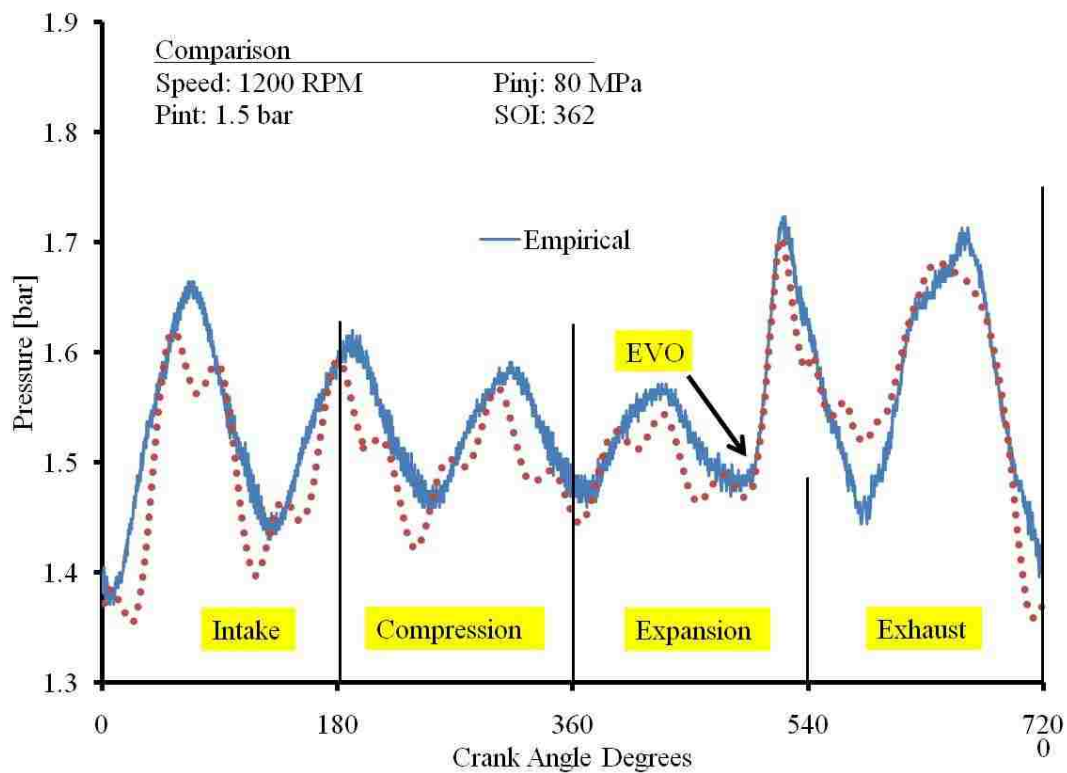


Figure 5.25: 1.6 bar IMEP Comparison

96

### 5.3.3 RPM Sweep Comparison
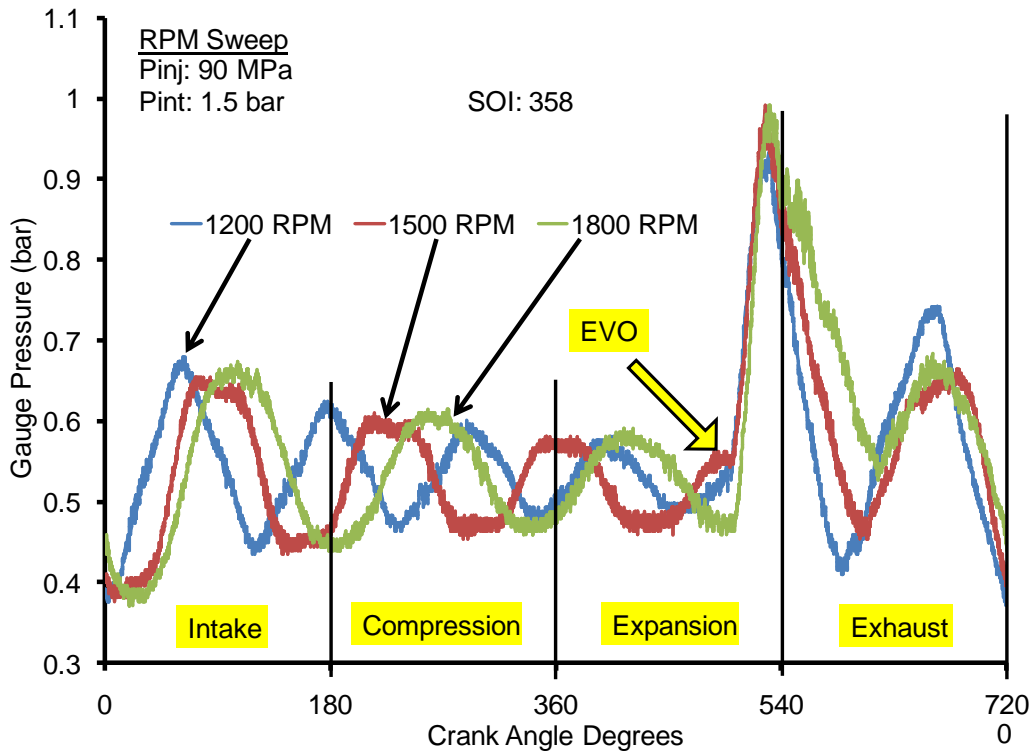


Figure 5.9: Empirical RPM Sweep
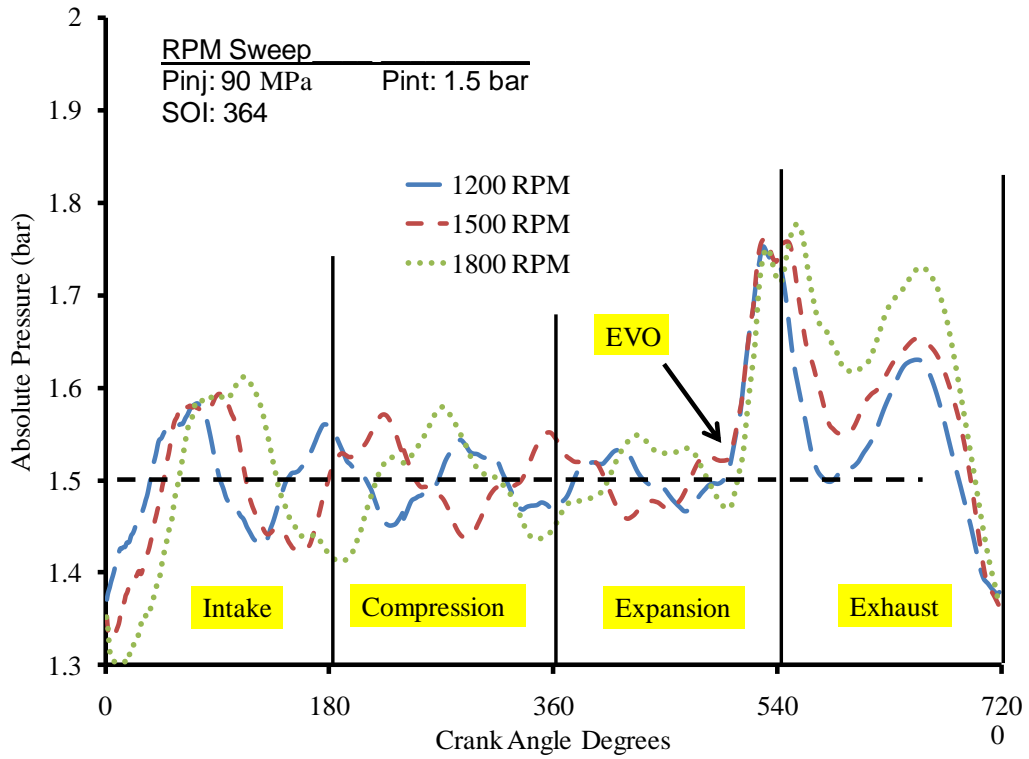


Figure 5.1: Simulated RPM Sweep

Figure 5.9 shows the empirical pressure wave action in the exhaust manifold, at different engine speeds, while figure 5.1 shows the simulated data for the same conditions. In both cases the same trends are seen. As engine speed increases, a frequency and phase shift of the pressure wave is observed. In both the simulated and empirical results, the total shift between 1200 rpm and 1800 rpm lies around $88^o$ during the compression stroke. The arrival of the pressure wave for the simulated data, at the time of the exhaust valve opening, follows the same trend as the empirical. At an engine speed of 1800 rpm, both the simulated and the empirical pressure wave results, benefit engine performance the most, since the pressure at the time of the exhaust valve opening, is a low pressure valley.

## 5.3.4 IMEP Sweep Comparison
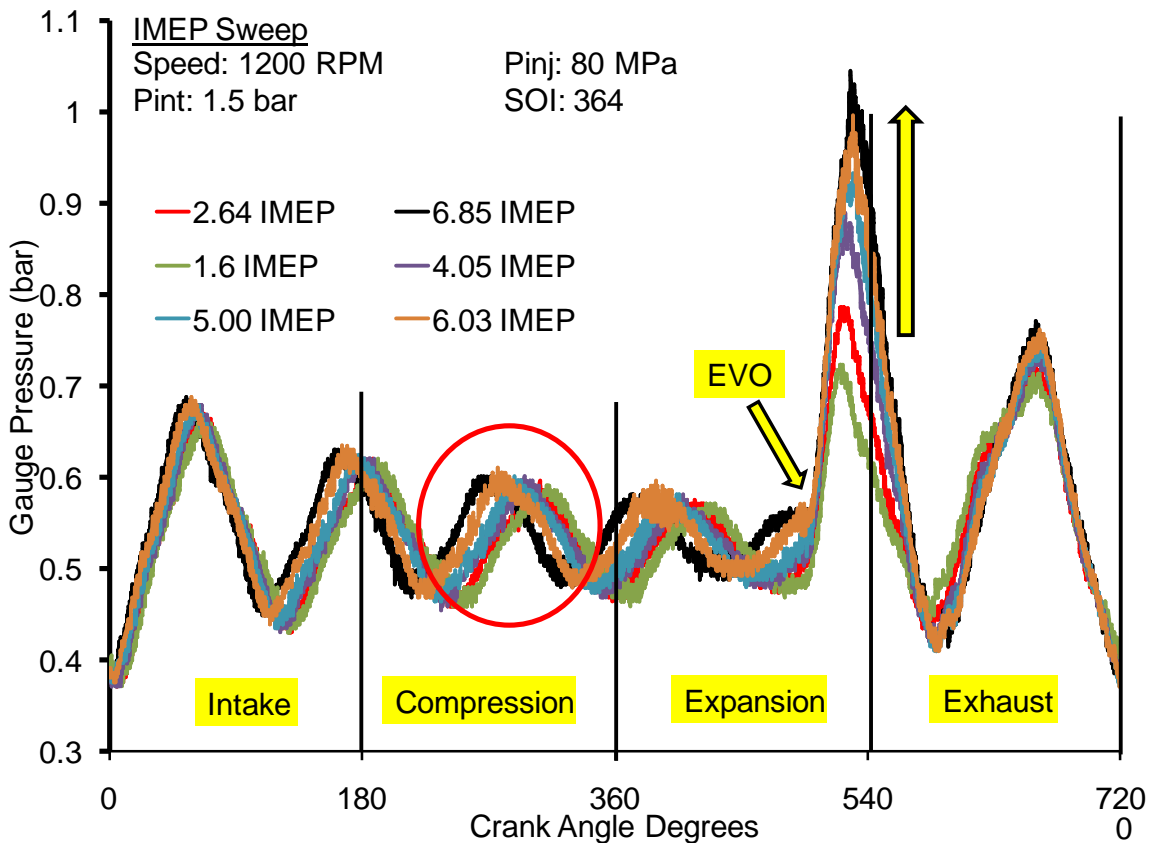


Figure 5.10: Empirical IMEP Sweep (1200 RPM)
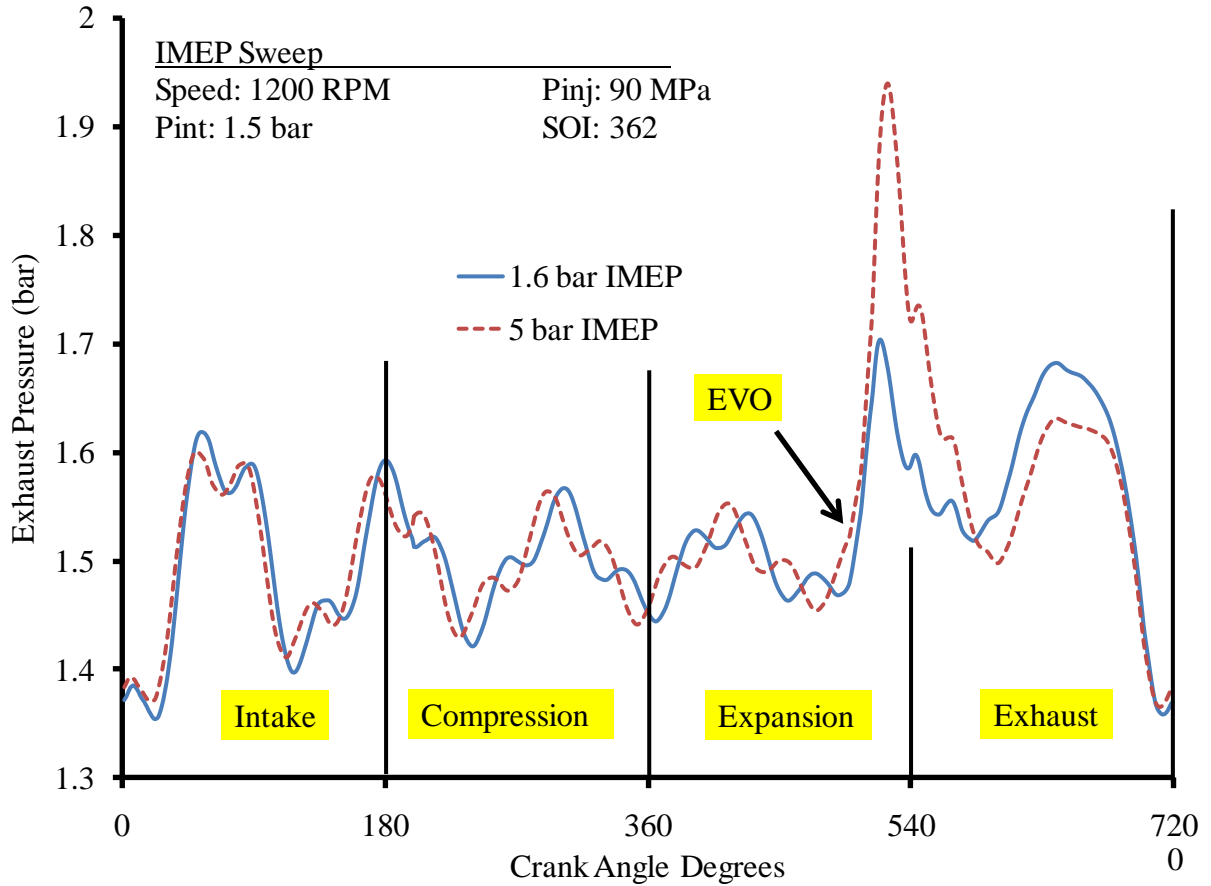
Figure 5.4: Simulated IMEP Sweep

The trends are the same for both the empirical and simulated data, as load changes at a constant engine speed. Figures 5.10 and 5.4, show the empirical and simulated data respectively. The empirical data shows more load conditions, as opposed to the two shown in the simulated. Nonetheless, the trends and characteristics for both load levels simulated are the same, as the empirical data. As load level increases, with constant engine speed, an increase in the first pressure spike, as the exhaust valve opens is observed. In both the simulated and empirical data, the frequency changes slightly during the compression and expansion strokes. The peak pressure values and curve frequency, for both load levels in the simulation, accurately match the empirical.

99

## 5.3.5 Backpressure Effect Comparison
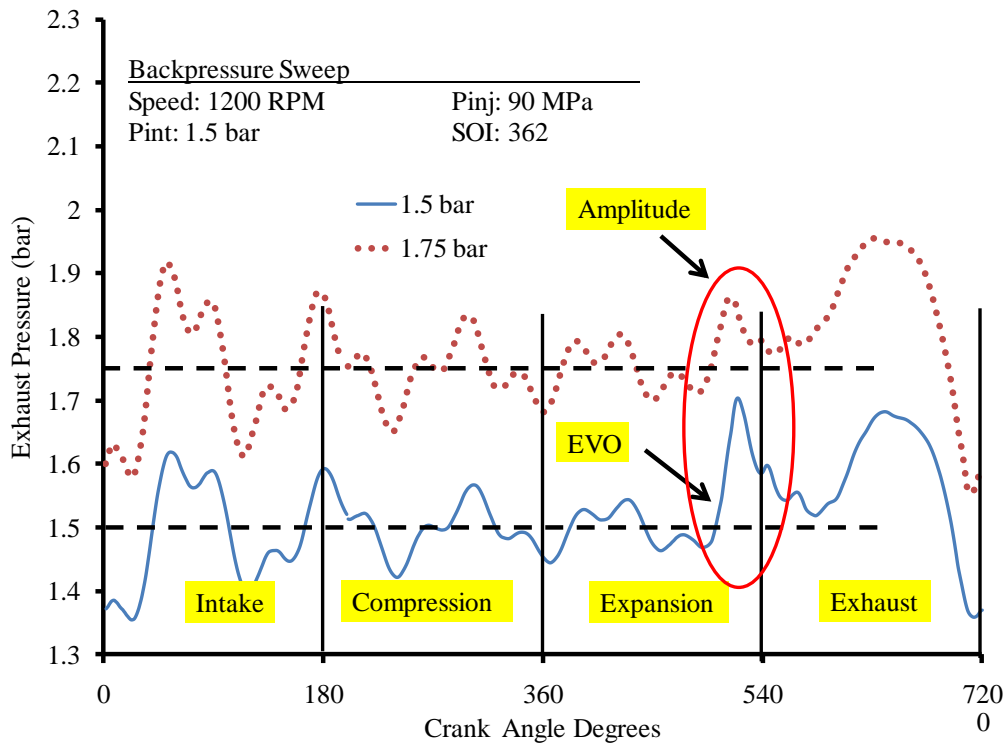


Figure 5.5: Simulated Backpressure Sweep



Figure 5.15: Empirical Backpressure Sweep

100
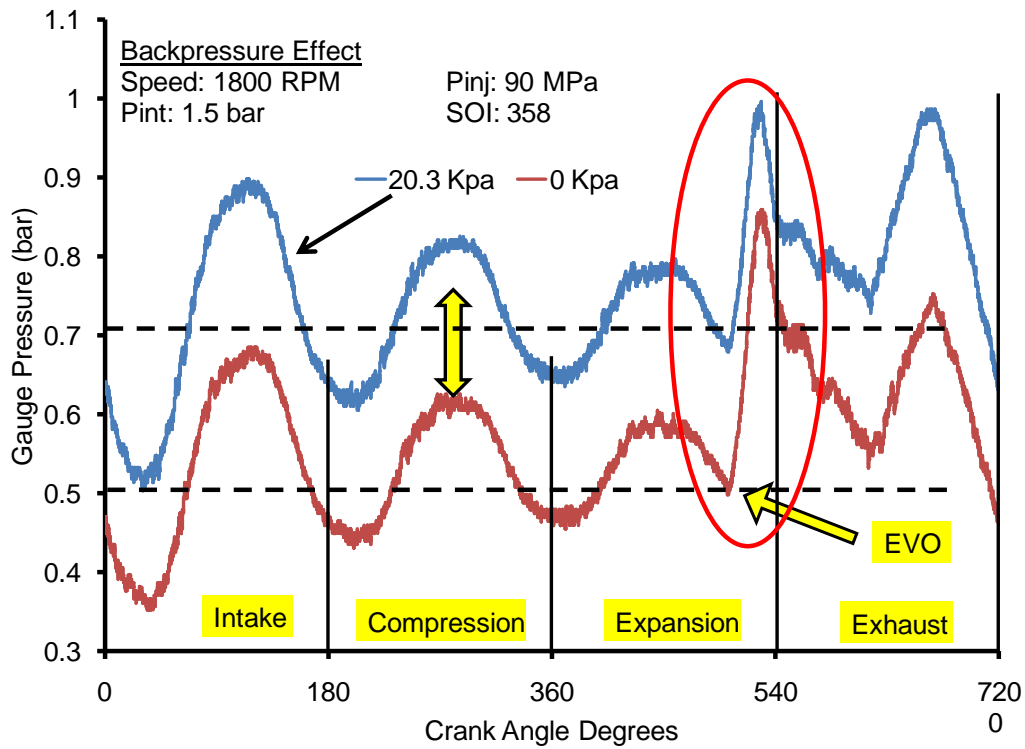
The backpressure effect for both the empirical and simulated data, are shown in Figure 5.15 and 5.5, respectively. As back pressure increases, a complete upward shift of the pressure wave curve occurs, without affecting frequency or phasing. It also reduces the initial pressure amplitude, as the exhaust valve opens. Both these trends are seen in the empirical and simulation results. The only difference is, that the simulated data was simulated at a higher engine speed than the empirical shown.

## 5.4 Orifice Flow Meter Test

The orifice meter was connected to a dry, high pressure air supply. Before reaching the upstream portion of the orifice meter, the air flowed through a pressure regulator, and finally through the flow meter for the Ford Puma research engine. The pressure regulator gave the upstream pressure reading, while the pressure drop was measured by a manometer. Four different pressure drops were tested, and their corresponding flow rates were calculated. These results are compared to the ones from the engine's flow meter, shown in figure 5.26. Both curves have the same slope and the error is less than 3%. One of the factors that may have attributed to the difference in flow rate is the upstream pressure reading from the regulator. A more precise reading needs to be acquired at the upstream side of the orifice. The engine's flow meter is a very precise reading, therefore more testing and calibration needs to be done, to ensure proper function and accuracy.
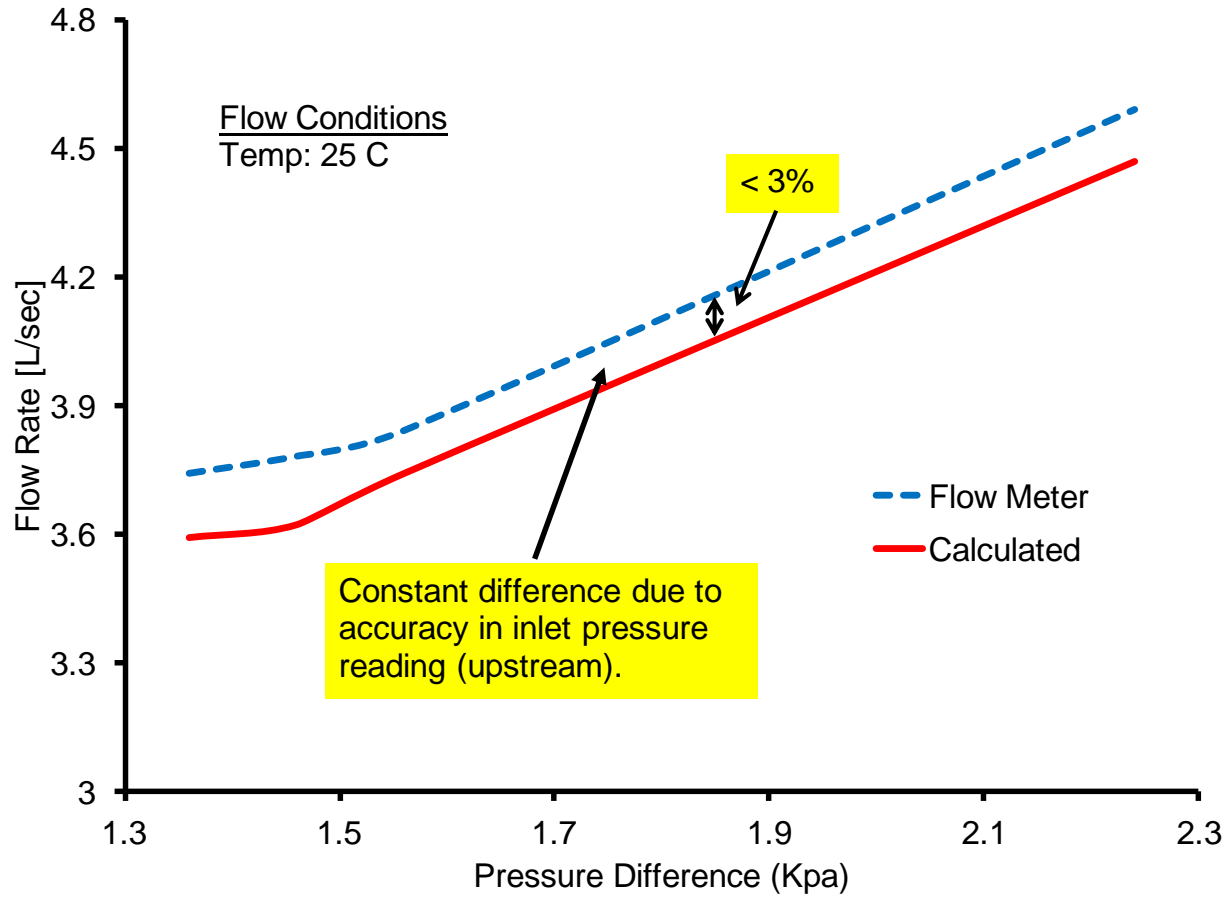
Figure 5.26: Orifice Test

# CHAPTER VI

## 6  CONCLUSION AND FUTURE WORK

The effect on pressure wave propagation, in exhaust manifolds, for various engine operating conditions, and different geometric exhaust configurations, have been demonstrated empirically, and by simulation. It is study to help understand the propagation characteristics of pressure oscillations in diesel exhaust manifolds, during different engine operating conditions. The following seven parameters and their effect on pressure wave actions have been presented in this thesis:

a) Engine Speed: Three different engine speeds, with constant intervals, at constant engine load, were conducted. As engine speed increased, the pressure wave frequency changed. As a result, the wave arrives at different pressure points, at the time of the exhaust valve opening (EVO). The shift caused by the increase of engine speed, observed in the empirical results, has the same crank angle value, as the simulation in the compression stroke. At certain engine speeds, the pressure wave arrives with either a positive or negative pressure peaks, making it ideal for either internal EGR or high exhaust flow. Also, as engine speed increases, the pressure amplitudes increase slightly, due to the increase in force exerted by the piston. In both simulation and empirical result, the same trends are observed, but the most significant trend is the frequency difference.

b) Engine Load: Various engine loads, at constant engine speeds were conducted. As higher loads are attained, cylinder pressure increases, hence, affecting peak pressure at the time of the exhaust valve opening. The amplitudes, throughout the wave's propagation, during the engine's

cycle are higher, but the most significantly affected, occurs at the EVO. The same trend is seen in both simulation and empirical results.

c) Backpressure: Two levels of backpressure at constant engine speed and load were both empirically tested and simulated. In both backpressure cases, the pressure wave remains with constant frequency and in phase, except for the upward shift, which represents the exhaust manifold pressure. In both the simulation and empirical results, the pressure peak at the time of the EVO, reduces in amplitude due to higher pressure conditions in the manifold. The rest of the amplitudes and wave characteristics seem unchanged.

d) Post-Injection: Various post-injection timings were conducted, at a constant engine speed and initial load. As different post-injection timings were employed, a rise in exhaust temperatures occurred, due to higher cylinder pressures and temperatures. The effect is similar to the load sweep results, where a higher initial peak pressure, at the time of the EVO, occurs. The rest of the wave characteristics, such as the frequency and phase, seem unchanged.

e) Runner Length: Only simulation test were conducted on the effect of runner length. In the same way as the engine speed tests, the most significant change occurs in the frequency of the curve. Therefore, arriving with different pressure values at the time of the EVO. Not only does frequency change, but different amplitudes are seen with different runner lengths.

f) Runner Diameter: Different runner diameters were simulated. In this case, as diameter changes, air flow velocity increases or decreases accordingly. This difference in air velocity causes a frequency change in the pressure wave propagation. This diameter change also affected peak pressure at the time of the EVO.

g) Position: Since SCR systems lie downstream of the exhaust system, the pressure wave effect was studied at a distant position from the exhaust valves. In this case, after-treatment devices

such as DPF's and DOC's, that dampen such waves, were not implemented into the simulation model. The pressure wave actions still occur downstream of the exhaust system, but not as pronounced. Besides the lessened pressure wave amplitudes, a lag exists due to the time required for the wave to travel the greater distance.

As a next step, in order to apply these pressure wave actions to emission control strategies such as EGR, an in depth study on intake manifolds is required. These pressure oscillations can help induce more EGR charge to any cylinder, by individually tuning each runner. Also, different injection strategies for the SCR system, using different points of the pressure wave, may help increase conversion efficiency, since it may distribute urea more efficiently. In order to continue this research, the portable dynamometer and orifice meter, are required to be completely functional. Once the research platform is established, different EGR distribution and SCR injection techniques, by applying pressure wave actions, should be studied.

# REFERENCES

1. Diesel, R. **"**Internal Combustion Engine," US Patent 0608845.

2. Majewski, W.A, Magdi Khair. **"**Diesel Emissions and Their Control," R-303, SAE International, Warrendale, 2006.

3. Zheng, Dr. Ming**. "**Fundamentals of Clean Diesel Engine Technology," Lecture Notes, University of Windsor, 2004.

4. United States Environmental Protection Agency**,** "Heavy Duty Diesel Emission Standards," http://www.epa.gov/oms/hd-hwy.htm, August. 2010.

5. Zheng, Dr. Ming, Dr. Graham T. Reader, G.J. Hawley**.** "Diesel Engine Exhaust Gas Recirculation – a Review on Advanced and Novel Concepts," *Journal of Energy Conversion and Management*, 2004, doi:10.1016/S0196-8904(03)00194-8.

6. Fable, Scott, Fanta Kamakate, Shyam Venkatesh**. "**Selective Catalytic Reduction Urea Infrastructure Study," National Renewable Energy Laboratory, Cupertino, 2002.

7. PACCAR. "Selective Catalytic Reduction - Technology for the Environment & Business," Columbus, Mississipi, 2010.

8. Heywood, John B**,** "Internal Combustion Engine Fundamentals," McGraw-Hill, Singapore, 1988.

9. Pearson, Richard, Desmond Winterbone, "Theory of Engine Manifold Design - Wave Action Methods for IC Engines," Professional Engineering Publishing Limited, St. Edmunds, 2000.

10. Rathakrishnan, Ethirajan, "Applied Gas Dynamics," John Willey and Sons, Singapore, 2010.

11. Benedict, Robert P, "Fundamentals of Gas Dynamics," John Willey and Sons Inc, Toronto, 1983.

12. Moody, Frederick J, "Introduction to Unsteady Thermofluid Mechanics," John Willey and Sons, New York, 1990.

13. C. Marquand, D. Croft, "Thermofluids - An integrated Approach to Thermodynamics and Fluid Mechanics Principles," John Willey and Sons, 1994.

14. Pefley, Richard, Ian Murray, "Thermofluid Mechanics," McGraw-Hill Book Company, San Francisco, 1966.

*15.* Sleigh, Dr. A, "Fluid Dynamics-The momentum and Bernoulli Equations," Lecture Notes, University of Leeds, 2009.

16. O'Keefe Controls, "Choked Flow of Gasses," http://www.okcc.com/PDF/Choked%20Flow%20of%20Gases%20pg.48.pdf, August. 2000.

17. Benson, Rowland S, "The Thermodynamics and Gas Dynamics of Internal Comsbustion Engines," Vol I, Oxford University Press, New York, 1982.

18. Kistler, "4075A10 Pressure Transducer," http://www.kistler.com/CH_en-ch/13_Productfinder/App.4075A10/Piezoresistive-absolute-pressure-sensors-10-bar.html, August. 2011.

19. Kistler, " 7075 Water Cooled Adapter," http://www.kistler.com/PH_en-sg/13_Produc tfinder/App.7505/Cooling-adapter-M18x1-5-M12x1-wrench-size-SW21.html, August. 2011.

20. Ricardo Inc, Ricardo Wave (Version 8.0), Computer Software, 2010

21. Dassault Systemes, CATIA (V5R20), Computer Software, 2010

22. Honeywell, "Sensing and Control Honeywell 1104," https://measurementsensors .honeywell.com/Pages/Product.aspx?category=PRODUCTTYPES-TORQUE-SlipRing-Shaft&cat=Honeywell&pid=1100&SortBy=&Asc=&rank=2, August. 2011.

23. Daytronic, "Signaling and Conditioning Products," http://www.daytronic.com/products /5M%20 series/5M%20series.htm, August. 2011.

24. International Organization for Standardization, "Measurement of Fluid Flow by Mean of Pressure Differential Devices inserted in Circular-Cross Section conduits Running Full," ISO 5167-2:2003 (E), 2003.

25. Dichtomatik. "O-Ring Gland Design Guidelines", USA.

## A.1 Portable Dynamometer Kart Design

The kart shown in Figure A.1, was donated by Ford Motor Company, and the system needed to be built on top of this kart. The kart is a stand used to transport engines within Ford's manufacturing plant. It is made up of rectangular steel beams, and a plastic oil spill pan in case certain engine fluids were to leak.



Figure A.1: Kart

## A.1.1 Supports

In order to build a flat steel plate on top of the kart, supports had to be made. These rail supports, are designed to slide along the rails that the kart already has in place. They are bolted down by means of T-blocks, as such in dynamometer bed platforms. In order to be able to tighten the bolts down to the kart, the ends of the rail supports had to be cut on an angle, as shown in Figure A.3. To ensure the rail supports remained within the rails, steel blocks were welded on the mating surface, as shown in Figure A.2. Across the rail supports, two additional perpendicular and rectangular supports were designed, for the flat bed to sit on. These rectangular supports, shown in Figure A.4, are bolted down to the rail supports.

| Figure A.2: Rail Support | Figure A.3: Top View of Rail Supports |

### A.1.2 Bed Plate

The bed plate is made up of two one inch thick steel plates, one section being shorter than the other, due to material availability. The shorter section bolts the AC motor, while the longer section bolts the rest of the components. The plate sits on top of both rectangular supports shown in Figure A.4.
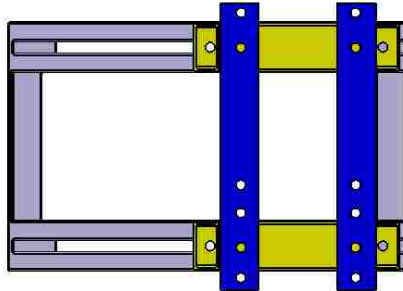


Figure A.4: CAD Bed Plate Supports [21]

A total of eight bolts are used to clamp down both bed plates onto the supports. The drilling of the holes was conducted on a Bridgeport. First, the holes were drilled onto the plates in precise locations. Once the drilling on the plates was completed, a punch tool was made to fit the right inner diameter of the holes, in order to locate the position on the support beams. In order to ensure the right positioning of the bed plates, if it were needed to be disassembled, ½ x 1 in dowel pins were used. A total of four pins were used to locate the plates onto the support beams.

The drilling and reaming of the dowel holes were done using a magnetic drill press. Figure A.5 shows the bed plates assembled to the supports.



Figure A.5: Blancher Grinder

Finally, straight edges and a flat surface needed to be machined. In this regard, a company by the name "Anchor Lamina", helped in machining straight edges and a flat surface. The straight edges along the plate serve as alignment tools. Figure A.5 shows the first trial in machining a flat surface, using a process called, "Blancher Grinding". The results were not suitable, therefore the plate was sent back to use a different process called, "Surface Grinding". The results are a glass mirror surface, with a .7 micron finish, seen in Figure A.6.



Figure A.6: Surface Grinder

Anti rust Oil is used and applied to bed plate surface to prevent rust. Depending on the ambient conditions, the oil should be applied every four to six months in low humidity environments and one to two months for humid conditions.

### A.1.3 Torque Sensor Support

A support block was required for the torque sensor which, would have the correct exact height, and also be simple enough to disassemble. The support block consists of two blocks, the first one bolting onto the bed plate shown by Figure A.8, and the second, bolting onto the torque sensor shown by Figure A.7.
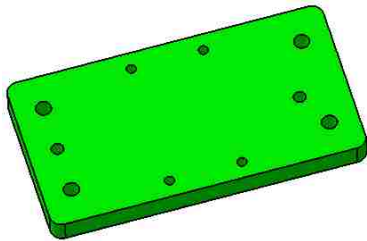


Figure A.7: CAD Sensor Top Plate [21]          Figure A.8: CAD Sensor Bottom Block [21]
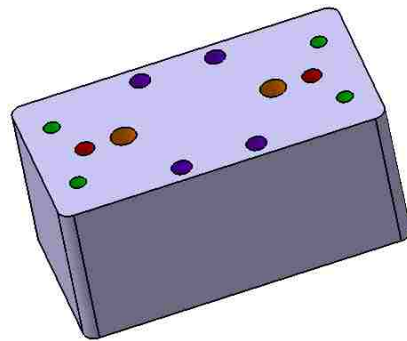
Two M8 shoulder bolts are used to clamp the block onto the bed plate. The shoulder bolts ensure proper location, while fastening the component down. The red holes shown in Figure A.8 represent the ¼ in dowel pins, used to locate the top block with the torque sensor to the bottom block, with M8 allen bolts. The purple holes are just recessions in the block, to accommodate the bolt heads used to fasten the torque sensor to the top plate.  Figure A.9 shows the complete assembly.
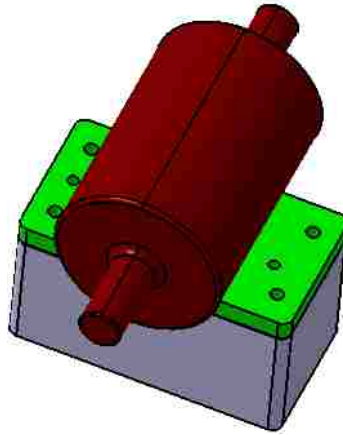
Figure A.9: CAD Torque Sensor Mounting Assembly [21]

**A.1.4 Pillow Block Bearings and Support**

Bearing selection is critical, and many efforts went into selecting the correct ones for the application. Different types of bearings and housings exist. Initially, premade pillow block bearings were the choice, but the degree of misalignment tolerance was too much. The tolerance needed to be less than one degree in every direction. Due to lack of selection, for the given price range, a custom pillow block was designed, which accommodated the bearings selected. The bearings used are single roller bearings, with a dynamic and static load capacity of 29.5 kN and 39.5 kN respectively, which corresponds to a safety factor of eight times. The bearings are rated at a maximum speed of 4800 rpm, well over motor's speed limitation. The pillow block designed, shown in figure A.10, uses two M12 bolts, and two ¼ in dowel pins. The construction consists of aluminum 6061, and has a 0.002 in interference with the bearings, for a secure press fit.
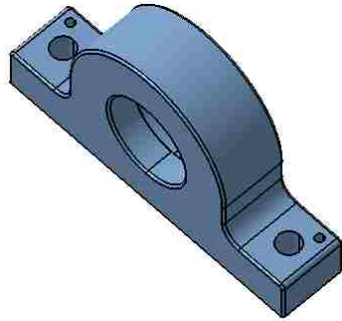
Figure A.10: CAD Pillow Block [21]          Figure A.11: CAD Bearing [21]

In the same way as the torque sensor, a mounting block had to be created, on which both custom pillow block bearings, could be mounted with the precise height. In designing the block, shown in Figure A.12, the pulley had to be taken into consideration due to its size, as well as being able to fit tools to tighten the pulley onto the shaft. The construction consists of M1 aluminum, machined manually on a Bridgeport.
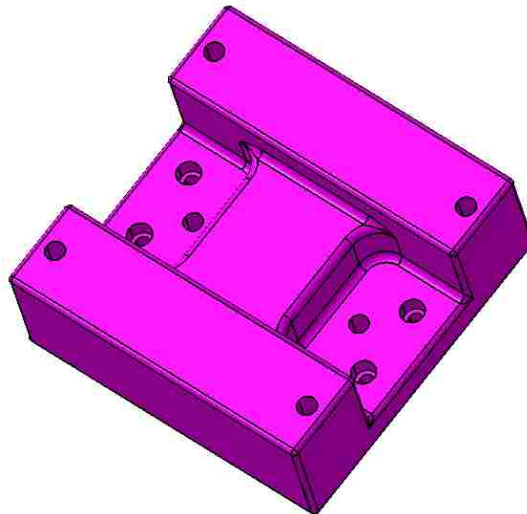


Figure A.12: CAD Pillow Bearing Block [21]

A total of eight bolts are used to tighten the block to the bed plate, along with two ½ in dowel pins for positioning. Four M10 allen bolts are used on the inner portion of the block, and four M6 allen bolts on the four recessed corners, to prevent the block from flexing during operating

114

conditions. The two ½ in dowel pins are located on the inner portion of the block, between the two M10 bolts. The pillow block bearings assembly is shown in Figure A.13.



Figure A.13: Pillow Block Bearing Assembly

**A.1.5 Shaft**

The shaft construction consists of 4041 hardened steel. The shaft consists of a solid design since the loads are relatively small. Mating lips are made for the pillow block bearings and pulley to rest on. The bearings can only be pressed onto the shaft one way, so once the whole system is assembled, no shaft play is present. Figure A.14 shows the shaft design along with the bearings and pulley.
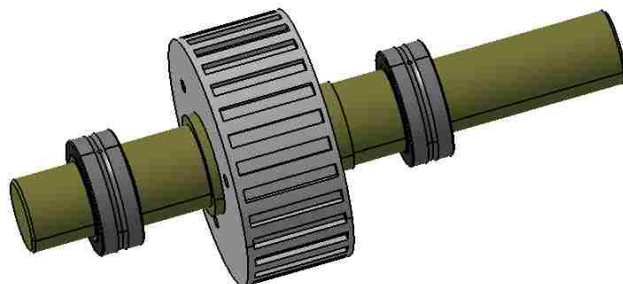


Figure A.14: CAD Shaft Assembly [21]

### A.1.6 Disk Couplers

The coupling system consists of circular flanges, coupled together by compressed thin disks, shown in Figure A.15. The circular flanges attached to the components, connect to the thin disk, so no direct contact between the flanges exists. The disks are stainless steel and flexible, to allow misalignment. Depending on the load requirement, different disk configurations, with different amount of thin disks put together, are needed. In this case, the disks used to couple the system together, consist of a total of six thin disks sandwiched together for every coupler. A total of two sets of couplers, are needed for both the motor to the torque sensor, and the torque sensor to the pillow block bearing assembly.



Figure A.15: Disk Coupler

### A.1.7 Safety Guard

Safety is always a priority, and in order to prevent dangerous situations, a steel guard was designed to cover the rotating components, except for the pulley. The major concerns are the couplers, as the disks might fail prematurely. The guard consists of rolled ¼ in steel, equipped with a one piece hinge. Also, the guard door contains a flange, where it can be securely fastened

by a nut, to the welded M8 bolt on the base flange. The top of the safety guard contains hole used for the torque transducer signal cable as shown in Figure A.16.



Figure A.16: Safety Guard

## A.1.8 Alignment

Alignment is always critical on fast rotating components, as vibrations can cause excess wear and be prone to premature failure. The alignment was conducted by setting a long flat steel rail, parallel to the length and perpendicular to the width of the bed plate. The rail served as a guiding tool, to slide a dial gauge across the length of the bed plate, measuring and aligning every component from its shaft. The final product is shown in Figure A.17.
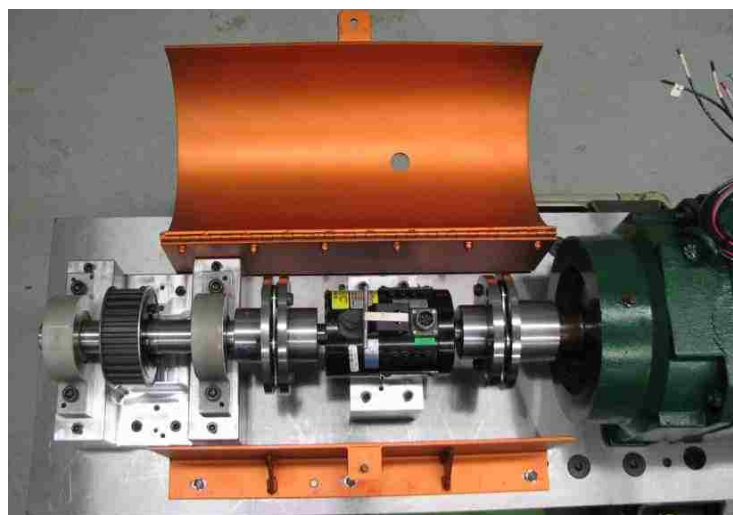


Figure A.17: Dynamometer Assembly

117

## APPENDIX B

**B.1 Orifice Meter Design**

As stated previously, the design chosen involves the location of the pressure tapings being a multiple of the main diameter of the pipe. The pipe diameter was chosen to be 55.8 mm. There are four major parts that make up the orifice meter, as shown in Table B.1, while the layout can be seen in Figure B.1.

| ORIFICE COMPONENTS | |
|---|---|
| 1 | Upstream |
| 2 | Downstream |
| 3 | Orifice Plate |
| 4 | Outside Cones |

Table B.1: Orifice Components
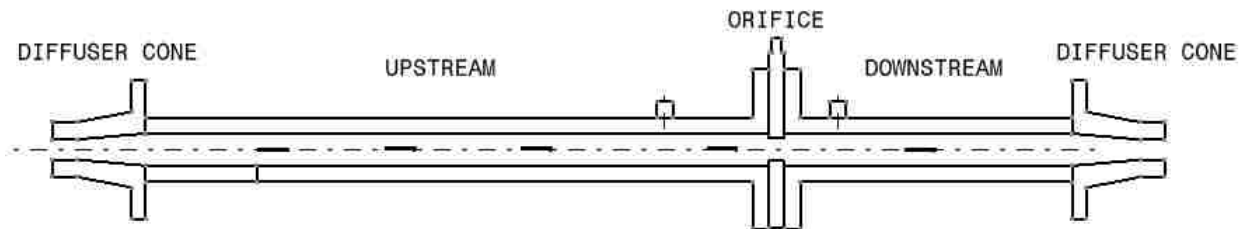


Figure B.1: Orifice Schematic

**B.1.1 Upstream**

The upstream or inlet pipe initially carries the working fluid, directing it to the orifice plate. A specified length, inner surface finish, and pressure taping location, is necessary to ensure accuracy.

### B.1.1.1 Upstream Length

The minimum length for the upstream pipe is specified by the guidelines ISO 5167-2:2003(E) [24]. The upstream lengths are given in multiples of inner diameter of the pipe. It is further broken down into categories depending on the configuration of the upstream pipe. Our design configuration lies under the full bore ball valve or gate fully open. A maximum diameter ratio as stated above previously is 0.75. The chosen maximum diameter ratio is 0.60, which yields an upstream length of 14 times the inner diameter of the pipe. Adjacent to that value, is a different lower multiple, which corresponds to an upstream length, if a flow conditioner were to be used. Since it was chosen not to use a flow conditioner, this topic will not be covered [24].

### B.1.1.2 Material and Production

The upstream pipe as well as the downstream pipe is made out of aluminum 6061. Aluminum is chosen in order to reduce weight and decrease machining difficulty. In order to avoid welding flanges which distort the material and increases alignment difficulty the upstream is made out of one solid piece of aluminum. Extensive amount of machining was necessary in producing this piece as well as others, which can be seen below. Figure B.2 and B.3 show the completed upstream pipe.



Figure B.2: Upstream Front View

Figure B.3: Upstream Side View

### B.1.1.3 Pressure taping

The location of the pressure taping $l_1$ on the upstream pipe is equal to the inner diameter of the pipe as shown in figure B.4 [24]. The correct measurement is taken from the upstream flange surface to the pressure taping axis. The pressure taping was drilled at $90^o \pm 3^o$ with respect to the main diameter axis and its diameter is no bigger than the 13 mm or 0.13D as stated in the guidelines ISO 5167-2:2003(E) [24]. The minimum taping depth required corresponds to 2.5 times the taping diameter. Table B.2 shows the detailed taping specifications used.
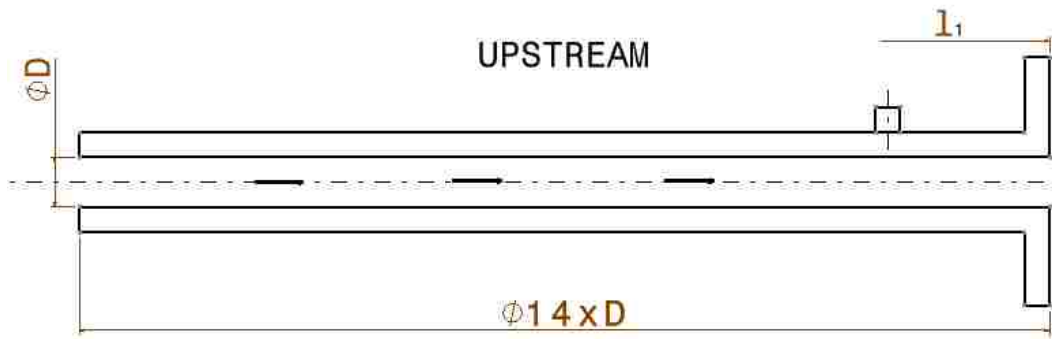


Figure B.4: Upstream Main Dimensions
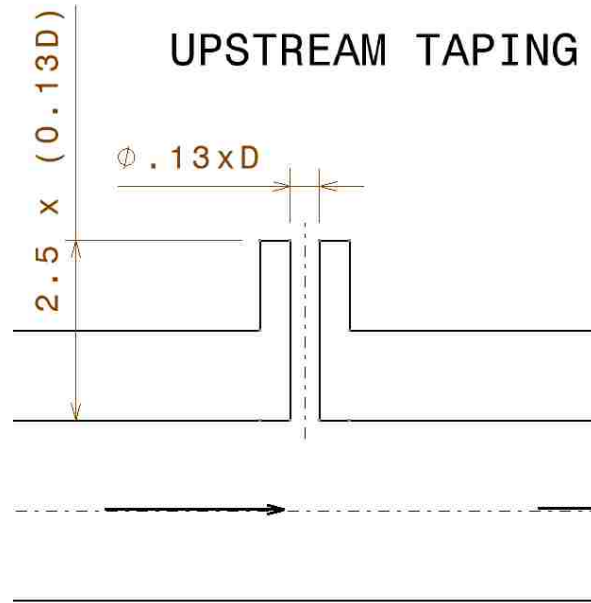
Figure B.5: Upstream Tapping Dimensions

| UPSTREAM PRESSURE TAPING SPECIFICATIONS | |
| --- | --- |
| Diameter | 3.2 mm |
| $l_1 = D$ | 55.8 mm |
| Taping depth (minimum) | 8 mm |
| Upper Tolerance ($l_1$) | 61.38 mm |
| Lower Tolerance ($l_1$) | 50.22 mm |

Table B.2: Upstream Tapping Specifications

In the upstream pipe design, a ring of material is created in order place the pressure taps as seen in figure B.6. This enables to use more than one pressure sensor in various locations around the pipe. The ring is separate from the flange and has a certain thickness.
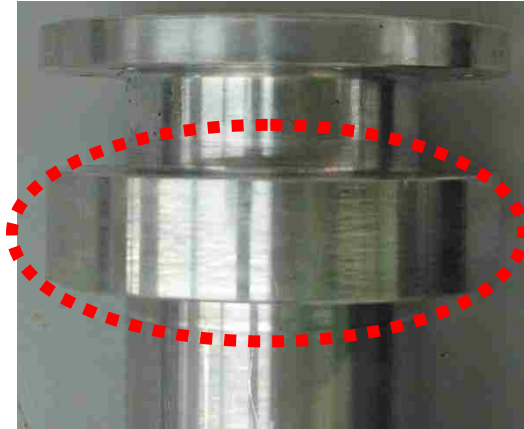
Figure B.6: Upstream Pressure Tap Ring

## B.1.2 Downstream

The downstream pipe, guides the fluid flow after it passes through the orifice, and into the ambient. In a sense it acts as the exhaust pipe of the orifice meter. It is also important to maintain guideline specifications, to ensure proper function and accuracy [24].

## B.1.2.1 Downstream Length

The downstream length is not as critical as the upstream but still requires a certain length to ensure proper reading of the pressure drop across the orifice plate. The required length also depends on the maximum diameter ratio chosen and can be found in the same way as the upstream length in the design guidelines ISO 5167-2:2003(E) [24]. In this case, based on a diameter ratio of 0.6 chosen, the minimum length required, is 7 times the main pipe diameter of 55.8 mm. Again, the proper measurement is taken from the flange flat surface to the end of the downstream pipe as shown in Figure B.7.
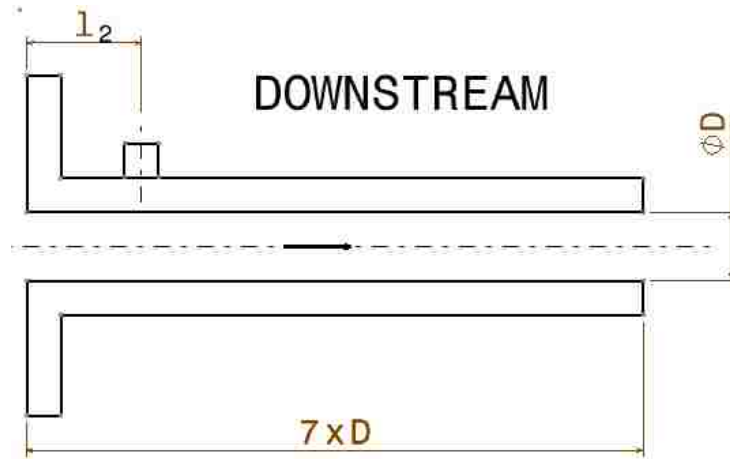
Figure B.7: Downstream Main Dimensions

## B.1.2.2 Material and Production

The downstream pipe as stated above is made out of aluminum 6061. Again, aluminum is chosen in order to reduce weight and decrease machining difficulty. In order to avoid welding flanges which distort the material and increases alignment difficulty, the downstream is made out of one solid piece of aluminum. Extensive amount of machining was necessary in producing this piece. Figure B.8 and B.9 show the completed downstream pipe.



Figure B.8: Downstream Front View

Figure B.9: Downstream Side View

## B.1.2.3 Pressure Tapping

The location of the pressure taping on the downstream pipe defined as $l_2$ is equal to nominally half the value of the main inner diameter of 'D' as specified in the guidelines: ISO 5167-2:2003(E) [24]. The proper location is measured from the main flange of the downstream pipe as shown in figure B.7. The location tolerance depends on the diameter ratio, as shown in Table B.3.

| DOWNSTREAM TAPING DISTANCE TOLERANCE | | |
|---|---|---|
| Diameter Ratio ($\beta$) | Tolerance | |
| | + | - |
| $\beta \leq 0.6$ | 0.52 x D | 0.48 x D |
| $\beta > 0.6$ | 0.51 x D | 0.49 x D |

Table B.3: Downstream Tapping Tolerance

The pressure taping was drilled at $90^o \pm 3^o$ with respect to the main diameter axis and its diameter is no bigger than the 13 mm or .13D stated in the guidelines. The minimum taping depth required corresponds to 2.5 times the taping diameter. Table B.4 shows the detailed taping specifications used.

| DOWNSTREAM PRESSURE TAPING SPECIFICATIONS | |
|---|---|
| Diameter | 3.2 mm |
| $l_2 = 0.5D$ | 27.9 mm |
| Taping depth (minimum) | 8 mm |
| Upper Tolerance ($l_1$) | 29.01 mm |
| Lower Tolerance ($l_1$) | 26.784 mm |

Table B.4: Downstream Tapping Specifications

In the same way as the upstream, a ring is created in order to adapt it with the pressure taps. In this case the ring is part of the flange as well since the location of the tap is closer to the flange. Figure B.10 shows the downstream pressure tap ring.
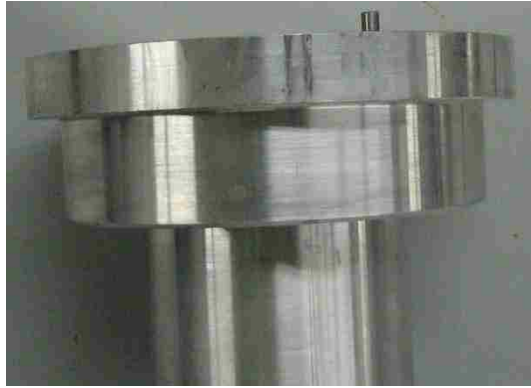


Figure B.10: Downstream Pressure Tap Ring

**B.1.3 Orifice Plate**

The orifice plate separates the upstream from the downstream by means of a small orifice diameter than compared to the main diameter of the pipe. This orifice causes a static pressure drop between the upstream and downstream due to a smaller diameter the flow has to pass through. The design guidelines of the orifice plate are critical and must be precise to ensure proper function and accuracy [24].

**B.1.3.1 Shape**

The orifice plate was chosen to be circular and concentric with the pipe's axis, and both the upstream and downstream faces, are parallel with one another, and flat as stated in the guidelines [24]. The shape of a standard orifice plate is shown in Figure B.11.
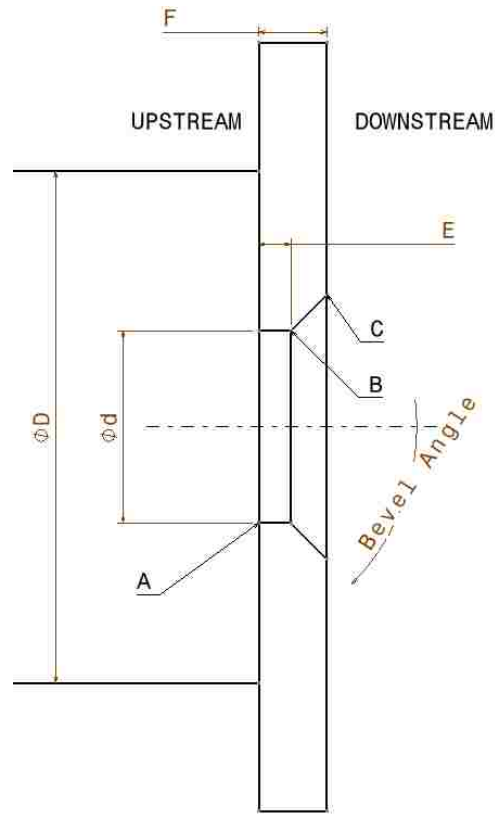
Figure B.11: Orifice Plate Schematic (Adapted from [24])

## B.1.3.2 Surface Quality

The surface quality is more critical on the upstream face as compared to the downstream face, but nonetheless both should be emphasized. A surface requirement stated by the guidelines of $Ra < 10^{-4} d$ was implemented on both the upstream and downstream faces [24].

## B.1.3.3 Thickness

The orifice plate as explained in the guidelines should have a thickness of $E \leq F \leq 0.05D$ [24]. When the main diameter is 50 mm and 64 mm the thickness F is permissible up to 3.2 mm. A thickness of 3.2 mm was chosen for the orifice plate. Thickness E as explained in the guidelines should be $0.005D \leq E \leq 0.02D$ and was chosen to be 0.8mm [24].

**B.1.3.4 Edges**

Edges A, B, and C as stated in the guidelines were machined to ensure sharp and no wire-edges or burrs [24]. A maximum radius of 0.05mm for the edges was chosen to ensure sharp edges which follow the guidelines [24].

**B.1.3.5 Material and Production**

Stainless steel is the material choice for the orifice plate due to possibility of rust which in turn will affect the correct function and precision of the instrument. Figure B.12 and B.13 show one of the orifice plates with a diameter d of 12.5 mm.



Figure B.12: Orifice Plate Side View          Figure B.13: Orifice Plate Front View

The orifice plates are designed with handles to ease assembly and present any damage to both the surfaces. The handle also has a 15 mm hole used for storage, so the plates can be hanged and not be lying on any faces to again prevent damage and contamination.

### B.1.3.6 Diffuser Cones

The diffuser cones are located at both ends of the orifice meter. The function is to smoothly guide the fluids into and out of the orifice meter. Also, the cones were designed with plate adapters to use different type and size nozzles that connect to both the fluid source and exhaust as seen in Figure B.14. Figure B.15 shows the actual finished parts.
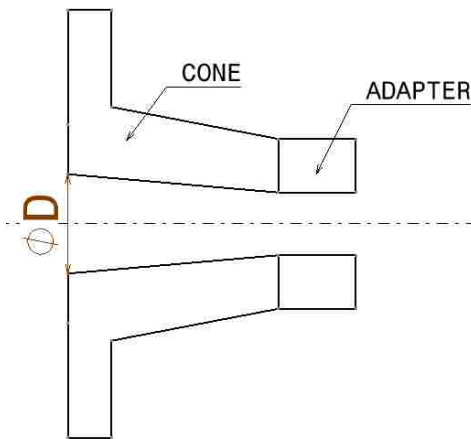


Figure B.14: Orifice Schematic        Figure B.15: Diffuser Cone

Both the adapter and cone are joined together by means of six M6 bolts and in order to insure sealing, a high temperature exhaust gasket was used, as seen in figure B.15. The surface finish used on the inside of the cone is the same as the one used for both the upstream and downstream. The adapter has a half inch brass NPT barbed fitting. New adapters can be made to use different type and size fittings.

Figure B.16: M6 Flange Bolts                    Figure B.17: Cone Assembly

These cones are attached to both ends of the orifice meter by means of a flange shown in figures B.18 and B.19. The flange is designed to thread onto the upstream and downstream ends. For this, male threads had to be cut on a lathe for both the upstream and downstream pipe. The flanges consist of a six bolt design and use six M8 bolts with washers and nylon locking nuts.





Figure B.18: Outside Flange Front View          Figure B.19: Outside Flange Side View

Figure B.20: Female Thread                    Figure B.21: Outside Flange Assembly



Figure B.22: M8 Outside Flange Bolts

To insure sealing between the cone and the threaded flange the same high temperature exhaust gasket is used, between the threaded flange and the face of both the upstream and downstream ends. A Viton o-ring is used and the gland dimensions on the threaded flanges follow the "Dichtomatik" o-ring guidelines for the correct o-ring compression and gland fill [25].

### B.1.3.7 Main Flanges

The main flange is designed such that there is only one possible assembly configuration. This prevents from setting up the orifice plate facing the wrong direction. It is done by two ¼ in dowel pins located on the downstream side at a certain radius and angle between them as seen in Figure B.23.



Figure B.23: Dowell Pins on Main Flange

The main flange also consists of a six bolt designed which uses M8 hex bolts with three washers, one being a spring washer.



Figure B.24: M8 Main Flange Bolts

To ensure alignment upon assembly, the downstream flange has an incision in which the orifice plate fits into, but it is thicker than the plate in order for the upstream flange to slide into as well. The upstream flange diameter is oversized by 0.002 in as compared to the diameter of the incision on the downstream, to ensure alignment.

O-rings are used for sealing and both compression and gland specifications are followed by the "Dichtomatik" design guidelines [25]. Both the upstream and downstream flanges use the same Viton o-ring shown in Figure B.25. A 75% gland fill, at a 25% o-ring compression is used.



Figure B.25: Main Flange O-rings

### B.1.3.8 Mounting

A stand was designed to mount the orifice in order to use and work on. It consists of a rectangular bean with two square legs. On the main rectangular beam C-clamps are bolted down to the beam by four M6 bolts with nylon locking nuts to hold the orifice as shown in figure B.26. The clamps are two piece parts that come together by two M6 allen bolts. The stand is made out of steel, and was chosen due to cost, while the c-clamps shown in Figures B.27 and B.28, are made out of aluminum 6061, in order to avoid external damage on the orifice meter.



Figure B.26: Orifice Stand



Figure B.27: C-Bracket Front View

Figure B.28: C-Bracket Top View

**VITA AUCTORIS**

NAME:                    Arturo Mendoza-Pinon

PLACE OF BIRTH:          Chihuahua, Mexico

YEAR OF BIRTH:           1987

EDUCATION:               Academy St. Cecile International School, Windsor

                         2001-2005

                         University of Michigan-Dearborn, Michigan

                         2005-2009 BASc.

                         University of Windsor, Windsor, Ontario

                         2010-2011 MASc.

## LIST OF PUBLICATIONS

1. Usman Asad, **Arturo Mendoza-Pinon**, Kelvin Xie, Marko Jeftic, Meiping Wang, Ming Zheng.; "Speciation Analysis of Light Hydrocarbons and Hydrogen Production During Diesel Low Temperature Combustion", Proceedings of the Internal Combustion Engine Division, ASME International, 2011 Fall Technical Conference, October 2-5, 2007, Morgantown, West Virginia, USA, Paper # ICEF2011-60130

## Posters:

2. M. Jeftic, T. Gao, Y. Shui, U. Asad, X. Han, K. Xie, X. Zhang, **A. Mendoza-Pinon**, M. Wang, M. Zheng, X. Chen, G.T. Reader. (2010). Green Auto Power Train Annual General Meeting. Theme 2: Diesel and Diesel Electric Power Train. Waterloo, Ontario.

3. P Divekar, F Lin, T Gao, Q Han, X Han, M Jeftic**, A Mendoza-Pinon**, K Xie, X Zhang, U Asad, R Kumar, C Mulenga, M Wang, S Yu; "Clean Diesel Engine Technologies: Past, Present, Future and Beyond", 10th Year Canada Research Chairs - thinking ahead for a strong future conference series; Ontario region: Nov. 24-25, 2010; Toronto.